A DISSERTATION IN THE LATE UNIVERSE, RECOMBINATION, AND THE SWAMPLAND CONJECTURES

by

Rance Matthew Solomon

October 4, 2022

A dissertation submitted to the
Faculty of the Graduate School of
the University at Buffalo, The State University of New York
in partial fulfilment of the requirements for the
degree of

Doctor of Philosophy

Department of Physics

The thesis of Rance Matthew Solomon was reviewed by the following:

Dejan Stojkovic
Professor of Physics
Thesis Advisor, Chair of Committee

William Kinney
Professor of Physics
Committee Member

Salvatore Rappoccio
Professor of Physics
Committee Member

Dedication

Let this work be an unsolicited but heartfelt marker to the patience that has been unduly paid to me by so many.
To my parents, Judy and Scott Solomon, you let me make all the right mistakes.
To my wife, Garvita Agarwal, your laugh is what I do it all for.

Acknowledgments

I must thank my oldest friends, Strawberry and Gimli. Their friendship kept the redundancies of school from squashing my interests in education. Thanks to my close friends Cooper, Herlan, and Stringer for providing a standard to work towards. Thanks to Erenso and Montemayor for making me into an adequate researcher and educator. Thanks to my graduate school comrades: Ben, Courtney, Jiawei, Jiayang, John, Kevin, Luke, Michael, Nathaniel, Omar, and Sushruth. We do not choose our friends in war but they are appreciated all the same.

A special thanks is owed to Stojkovic for trusting me even though I gave him no reason to. Today, the mountains are again mountains but unfortunately some of the waters are still not waters.

And finally, thank you to my family: Garvita, Mom, Dad, Amanda, Shali, Tim, and Roger-Trenton. I am a formed by them as much as a drop is formed from a crack in a water vase. Let my work serve as a partial reflection of their effect on my life.

Abstract

Modern cosmological models such as ΛCDM and single-field inflation have shown remarkable agreement with nearly all current observations. They have lent understanding to the accelerated expansion of the Universe observed with type Ia supernovae, match nearly perfectly to the abundance of light elements, have accurately predicted the size of the baryon acoustic oscillations seeded from the initial density perturbations, and have explained away the flatness, horizon, and monopole relic problems. Yet, the challenges that remain have grown worse with the increased accuracy of observations hinting that they will not likely go away. What is needed now are novel cosmological probes and new solutions to test these challenges. In this dissertation I discuss just that: my work in advancing the use of quasars as a novel standardizable candle and my work in modifying the period of recombination with an electron-symmetron coupling in order to solve the Hubble tension. I also discuss my work in testing the Weak Gravity and de Sitter Swampland Conjectures.

The dissertation is structured as follows. Part I provides a broad review of the background knowledge that the later chapters assume where as Part II, containing chapters 2 to 4, discusses the selected work and publications I have

contributed to during my Ph.D. candidacy. Chapter 2 focuses on my use of quasars as standardizable candles originally published in [1] along with a brief discussion on ΛCDM biases towards high z probes published in [2, 3]. Following my work in [4], chapter 3 lays down the arguments for a modified electron mass at recombination in order to relieve the Hubble tension. As a mechanism to drive the change in mass I propose a Yukawa coupling between the electron and symmetron field and discuss the likely observables. And Chapter 4 discusses my contributions towards studies in both a generalization of the Weak Gravity Conjecture and a study in how the de Sitter Swampland Conjecture can be applied to $P(X, \varphi)$ inflationary theories.

Table of Contents

List of Tables

List of Figures

Part I

Review

Chapter 1

The Good, the Bad, and ΛCDM

The field of cosmology has come a long way since the first cave person gazed into the Sun. Modern advances in telescopes, interferometers, and computing now allow us to gaze into billions of stars, stellar explosions, accreting black holes, the first formation of nuclear hydrogen, and may be soon the gravitational ripples created from the earliest moments after the big bang. As the technology evolved so did our description of the Universe. Some good ideas were proposed, some bad ideas too, and now we have a working model, ΛCDM.

In the remaining chapters of part I I will describe in sufficient capacity the current status of topics relevant to my work. These topics include: general relativity and the FLRW Universe, the ΛCDM model, the expanding universe at low redshifts, and inflation. A reader well learned in cosmology and astrophysics may skip to II where I discuss the work I have done during my Ph.D. candidacy.

1.1 General Relativity

The history of General Relativity (GR) is likely one of great intrigue with Albert Einstein's seminal work in 1905 on Special Relativity eventually leading to a very fertile year of publications in 1915 which outlined the details of GR. The theory can be summed up very nicely with Einstein's field equations

$$R_{\mu\nu} - \frac{1}{2}Rg_{\mu\nu} + \Lambda g_{\mu\nu} = \frac{8\pi G}{c^4}T_{\mu\nu}. \tag{1.1}$$

The left hand side of the equation describes the geometry of a curved manifold while the right hand side accounts for the matter[1] content in a system. Together we get the take-away idea of GR: matter causes curvature and curvature moves matter. A full description of GR is of course beyond the scope of this thesis but I point the interested reader to the densely written "General Relativity" by Wald [5], the very useful "Problem Book in Relativity and Gravitation" by Lightman, Press, Price and Teukolsky [6], or the coffee table book "Gravitation" by Misner, Thorne, and Wheeler [7]. For the purposes here, a brief overview of (1.1) and some of its consequences should suffice.

Content warning, throughout this text, unless otherwise stated, I will be assuming $G = c = 1$ and the metric signature of choice will be (-,+,+,+).

I begin again with the left hand side of (1.1). The $R_{\mu\nu}$ term in addition to its scalar counterpart, $R = R^{\alpha}{}_{\alpha}$, denotes the Ricci curvature tensor and the Ricci scalar, respectively. The tensor can be expressed as a collection of partial derivatives of the metric, $g_{\mu\nu}$,

$$R_{\mu\nu} = \Gamma^{\alpha}{}_{\mu\nu,\alpha} - \Gamma^{\alpha}{}_{\alpha\nu,\mu} + (\Gamma^{\alpha}{}_{\alpha\beta}\Gamma^{\beta}{}_{\mu\nu} - \Gamma^{\alpha}{}_{\mu\beta}\Gamma^{\beta}{}_{\alpha\nu}) \tag{1.2}$$

[1] Matter is used in a loose sense here. All forms of energy content is included.

where $\Gamma^{\sigma}{}_{\mu\nu}$ is the Christoffel symbol which GR assumes as the affine connection given by

$$\Gamma^{\sigma}{}_{\mu\nu} = \frac{1}{2}(g_{\nu\alpha,\mu} + g_{\mu\alpha,\nu} - g_{\mu\nu,\alpha})g^{\sigma\alpha}. \tag{1.3}$$

An very prominent prediction of GR can already be seen, but perhaps it is made clearer if I momentarily consider $\Lambda = 0$ and rewrite left hand side of (1.1) with the Einstein tensor, $G_{\mu\nu} \equiv R_{\mu\nu} - \frac{1}{2}Rg_{\mu\nu}$, so that

$$G_{\mu\nu} = \frac{8\pi G}{c^4}T_{\mu\nu}. \tag{1.4}$$

Since $G_{\mu\nu}$ is up to second order in partial derivatives of the metric with respect to the spacetime coordinates then what we have is a wave equation sourced by the stress energy tensor. So quite readily one could expect the existence of gravitational waves, but since the coefficient $8\pi G c^{-4}$ is quite small ($\sim 10^{-43}\mathrm{N}^{-1}$) the source would have to be immense if we have hopes of detecting the waves; hence why LIGO, VIRGO, and eventually LISA are looking at merging binary neutron stars and black holes.

I want to make an important aside on the Λ term or the cosmological constant. It is currently not clear whether this term should be taken into account in the field equations. Most often we consider the cosmological constant to be the observed dark energy (thus the name ΛCDM) because it would provide an accelerated expansion with an effective fluid equation of state (EoS) of $w = -1$ as is observed in low redshift observations. However, it could be that the dark energy's EoS evolves with redshift in such a way that it looks like a constant in our current epoch in which case dark energy and Λ would not necessarily be identical. The possible difference between Λ and dark energy is corroborated

by the fact that if the cosmological constant is sourced by vacuum fluctuations then the predicted Λ value from electroweak calculations alone differs from the cosmologically measured value by 55 orders of magnitude [8]. But now that this caveat has been addressed, I will take the approach that many in the field take which is to treat the cosmological constant and dark energy as the same thing until something better comes along with convincing evidence.

1.1.1 General Relativity on Large Scales

We can make the ansatz that our Universe at the largest scales (at least above that which galaxy clusters form, $\gtrsim$ 100Mpc) is uniform and isotropic. This idea carries over from Copernicus' work on the decentralization of the Earth in celestial mechanics and is suitingly referred to as the Copernican principle. Under the Copernican principle we can argue that the most general metric is the Friedman-Lemaître-Robertson-Walker (FLRW) metric:

$$\mathrm{d}s^2 = -\,\mathrm{d}t^2 + a^2(t)\Big(\,\mathrm{d}r^2 + S_k(r)^2\,\mathrm{d}\Omega^2\Big) \tag{1.5}$$

where a is the scale factor and k is a constant which parameterizes the intrinsic curvature of space-time[2]. The function $S_k(r)$ takes the form

$$S_k(r) = r\,\mathrm{sinc}(r\sqrt{k}) = \begin{cases} \sqrt{k}^{-1}\sin(\sqrt{k}r) & k > 0 \\ r & k = 0 \\ \sqrt{k}^{-1}\sinh(\sqrt{k}r) & k < 0 \end{cases} \tag{1.6}$$

[2]The term $\mathrm{d}\Omega^2 \equiv \sin^2(\phi)\,\mathrm{d}\theta^2 + \mathrm{d}\phi^2$ which only shows up here should not be confused with the fractional energy density Ω to be introduced below.

and is dependent on if the Universe is open ($k > 0$), flat ($k = 0$), or closed ($k < 0$)[3]. Both a and k can be talked about in two ways: (i) a is dimensionless so that k has units of [LENGTH]$^{-2}$ or (ii) a has units of [LENGTH] while both k and r are dimensionless. The difference between the two is only a matter of convenience, and for convenience I will be using the former choice so that I can define the scale factor today as unity giving the simple conversion between scale factor and redshift $a = (1 + z)^{-1}$.

The stress-energy tensor, or energy-momentum tensor, $T_{\mu\nu}$, can generally be written as

$$T_{\mu\nu} = -2\frac{\partial \mathcal{L}_M}{\partial g^{\mu\nu}} + g_{\mu\nu}\mathcal{L}_M \tag{1.7}$$

where $\mathcal{L}_M$ is the Lagrangian density for the matter fields which must satisfy the continuity equation, $T^{\alpha}{}_{\mu;\alpha} = 0$. The definition of $\mathcal{L}_M$ will vary depending on the system of interest. For example, the Schwarzschild black hole is a vacuum solution with a $\mathcal{L}_M$ such that $T_{\mu\nu} = 0$ everywhere except at the singularity at which point it is undefined. Often for cosmological purposes we consider perfect fluid systems which on large scales works very well. In the perfect fluid case we can write the stress-energy tensor as

$$T_{\mu\nu} = (p + \rho)U_\mu U_\nu + p g_{\mu\nu}. \tag{1.8}$$

The fluid's pressure, p, and density, ρ, can always be related by $p = w\rho$ where w is the EoS mentioned earlier. In the rest frame of the fluid (i.e. when $U^\mu U_\nu = 1$ which will be the frame we assume from now on) the stress-energy tensor takes

[3]Current observations put k very near to zero [9].

the form

$$T^{\mu}{}_{\nu} = \begin{bmatrix} -\rho & 0 & 0 & 0 \\ 0 & p & 0 & 0 \\ 0 & 0 & p & 0 \\ 0 & 0 & 0 & p \end{bmatrix} \tag{1.9}$$

with a trace

$$T \equiv T^{\mu}{}_{\mu} = -\rho + 3p. \tag{1.10}$$

The trace is not important here but it will briefly return later in chapter 3 when I argue for a coupling of the matter fields to the trace of the stress-energy tensor.

Now that we have chosen a metric and a stress-energy tensor we can reduce the Einstein field equations (1.1). The 00-component we would find gives the first Friedmann equation

$$H^2 \equiv \frac{\dot{a}^2}{a^2} = H_0^2(\Omega + \Omega_k a^{-2}) \tag{1.11}$$

where H and H_0 are the Hubble parameter and the Hubble constant, respectively, used as a measure of the expansion rate of the universe. I have also defined the fractional energy density of the fluid, $\Omega \equiv \frac{\rho}{\rho_c}$ (where $\rho_c \equiv \frac{3H_0^2}{8\pi G}$ is the critical density at which the universe would be exactly flat), and that of the curvature, $\Omega_k \equiv \frac{k}{H_0^2}$. In general, Ω is a function of the scale factor such that at $a = 1$ we expect $(\Omega + \Omega_k) = 1$. For a composite system of n perfect fluids with constant EoS we can express Ω as

$$\Omega = \sum_i^n \Omega_{i_0} a^{-3(1+w_i)}. \tag{1.12}$$

	w_i	Ω_i	Ω_{i_0}
radiation ..	$1/3$	$\Omega_{r_0} a^{-4}$	$\Omega_{r_0} \approx 9 \times 10^{-5}$
matter	0	$\Omega_{m_0} a^{-3}$	$\Omega_{m_0} \approx 0.3$
dark energy	-1	Ω_Λ	$\Omega_\Lambda \approx 0.7$

Table 1.1: The three commonly used perfect fluid contributions to the energy content in the Universe. The columns in order are the fluids' EoS, scaling relations, and approximate estimates of their current densities from observations.

A non-constant EoS is not much more difficult to solve for and can be written as

$$\Omega = \sum_i^n \Omega_{i_0} \exp\Big[-3\int (1+w) a^{-1}\, \mathrm{d}a\Big]. \tag{1.13}$$

In most of the fluids we are interested in, a constant EoS is a sufficient assumption and as such we will continue to assume the form (1.12), but many alternative models of dark energy suppose an evolving EoS so (1.13) remains relevant in the literature. The coefficients in the series satisfy $\sum_i^n \Omega_{i_0} = 1 - \Omega_k$ and represent the current densities of the fluids today. The standard cosmological model, which will be discussed later, has three fluid components which I have listed in table 1.1. Their scaling relations are quite easy to argue for based on first principles and are sketched in figure 1.1. The matter density scales with the volume inverse (a^{-3}) as is usually the case for pressureless dust system. Likewise, radiation scales with the volume inverse but with an additional factor due to the radiation's wavelength stretching with the scale factor. Dark energy's scaling relation is a bit of an anomaly but it can be physically argued for by considering a scalar field with a potential energy term dominating its kinetic energy term. I will discuss this type of fluid in more detail in section 1.4, but for now it should suffice to say that the scaling relation of dark energy is the simplest working relation we have to match with observation.

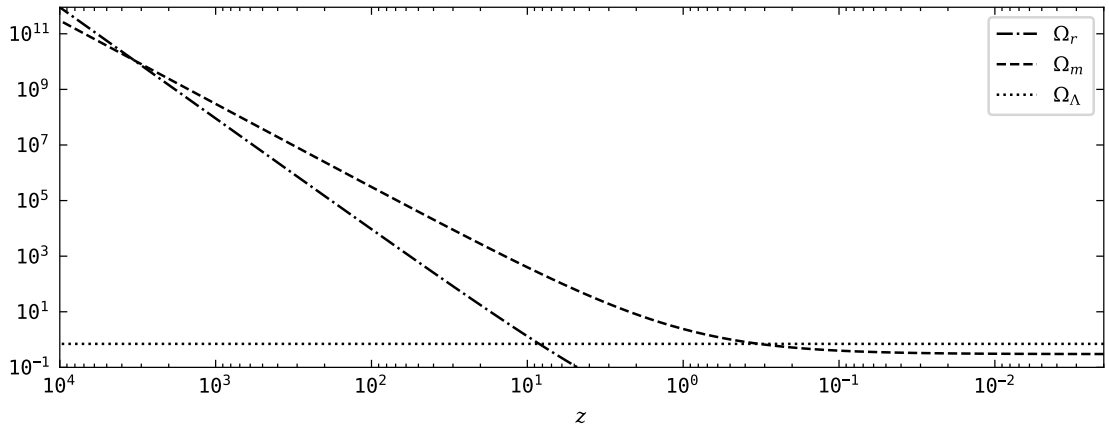

Figure 1.1: The three perfect fluids making up the energy content of the Universe as a function of redshift. Based on current observations, in the present (rightmost, $z \lesssim 0.3$) the Universe is dark energy dominated while in the distant past (leftmost, $z \gtrsim 3000$) the Universe was radiation dominated and in between we had a phase of matter domination.

In addition to (1.11), the ii-component of (1.1) in combination with the 0-component of the continuity equation, $T^{0\alpha}{}_{;\alpha} = 0$, can be used to determine the second Friedmann equation, a linearly independent relation dictating the behavior of the Hubble parameter,

$$\dot{H} + H^2 = \frac{\ddot{a}}{a} = -\frac{1}{2}H_0^2 \sum_i^n (1 + 3w_i)\Omega_i. \tag{1.14}$$

We can now see that in general the Universe will undergo some accelerated expansion, either positive or negative, and a constant expansion rate would require a fine tuning between the separate fluids. Furthermore, if for simplicity we consider an effectively single fluid state with $w < -1/3$ then the Universe will undergo an accelerated expansion. Thus, throughout the matter and radiation dominated epochs the expansion rate was slowing until the fairly recently onset of dark energy domination causing the expansion rate to quicken. If dark energy proves to have a constant EoS $w = -1$ as it seems to have from current

observations then our Universe will eventually evolve towards a de Sitter universe (i.e. one with only a $w = -1$ fluid or cosmological constant) marked by an exponential growth in the scale factor, $a \propto \exp[2H^2 t]$, similar to the inflationary epoch of the very early Universe.

1.1.2 General Relativity at Small Scales

By small scale I of course mean in the ball park of astrophysical objects, primarily stellar sized black holes (BHs) – a sufficient discovery of a quantum theory of gravity still remains to be made[4]. BHs were predicted very early on after the construction of GR and have been inferred in observations of stars orbiting massive unseen counterparts. In recent years the gravitational wave observations from LIGO/VIRGO and the BH image from EHT have all but solidified the existence of BHs in nature. The typical story of BH formation is that a massive star ($> 3M_\odot$) will eventually collapse into a white-dwarf star, which might eventually collapse into a neutron star, which might eventually collapse into a BH. But since BHs are sourced by extreme densities then we can also expect them to be produced around the initial density perturbations in the early Universe. These latter BHs are referred to as primordial black holes (PBHs) and have been proposed as a candidate for the missing matter in the Universe (i.e. dark matter). PBHs are no longer in strong favor for explaining the missing matter due to the combined constraints from transient microlensing searches such as EROS and MACHO and those from wide binary perturbations [10].

The transition from an initial state, whether a neutron star or an over dense region in the early universe, to a BH can be a very complicated process where

[4] A discovery for which the discoverer will no doubtedly win a great number of many noble awards and grants along with the highly sought after and miserable life of a celebrity.

inflowing gas and plasma can cause large deviations from spherical symmetry. But the final stable state of the BH we know very well since only three quantities are needed to define it: mass (M), angular momentum (J), and charge (Q). The charge does not have to be the $U(1)$ charge of electromagnetism but for convenience I will speak of it as such. The most general BH solution is given by the Kerr-Newman metric but it is much too long of a solution to put here so for brevity I will only discuss its horizon radii:

$$R_{\pm} = M \pm \sqrt{M^2 - a^2 - Q^2} \tag{1.15}$$

written in units where $4\pi\epsilon_0 = 1$ and with the angular momentum parameter $a \equiv J/M$ not to be confused with the scale factor[5]. There are three relevant limiting cases:

Schwarzschild ($Q = a = 0$) The Schwarzschild solution is the most general spherically symmetric vacuum solution of (1.1). It has a single radius of $R = 2M$ and it is expected that evaporative processes will drive all BHs towards the Schwarzschild state.

Reissner-Nordström ($a = 0$) The Reissner-Nordström BH has two radii, $R_{\pm} = M \pm \sqrt{M^2 - Q^2}$. The outer horizon, R_+, is the true event horizon while the R_- is only a Cauchy horizon with the space inbetween allowing for trapped space-like geodesics. We can imagine through some mechanism that $Q^2 \to M^2$ which would cause the two horizons to become degenerate and form what is called an extremal BH. Extremal BHs are very interesting

[5]The angular momentum parameter, a, will only be used in this section. Elsewhere in the text a can be safely assumed as the scale factor.

in that the Hawking evaporation for a Reissner-Nordström BH goes as

$$T = \frac{1}{2\pi}\frac{\sqrt{1-Z^2}}{1+\sqrt{1-Z^2}} \tag{1.16}$$

which clearly goes to zero when $Z \equiv Q/M \to 1$. Thus, if the thermodynamic analogy persists then extremal BHs would be an example of an absolute zero temperature system. If the state $Q > M$ can be reached then the geometry of the space no longer has an event horizon and a naked singularity is left behind. The extremal bound is discussed in greater detail in chapter 4.2.1 where a few of these comments will be repeated for continuity purposes. In practice astrophysical charged BHs are highly unlikely due to the net neutrality of matter but it remains a theoretically rich course of study especially when one considers the evaporation of small BHs near the Planck mass.

Kerr ($Q = 0$) The Kerr solution is the most astrophysically relevant BH and our first one with axial symmetry. Similar to the Reissner-Nordström BH it has two radii, $R_\pm = M \pm \sqrt{M^2 - a^2}$ and likewise it too has an extremal case at $a^2 = M^2$ with a similar behavior for the Hawking temperature. And even though Hawking evaporation can more readily evaporate away angular momentum than charge it is also much easier to construct a way to spin up a BH towards the extremal bound by accreting matter or by collapsing a high-spin neutron star.

While other BH solutions exist (e.g. Gauss-Bonnet, dilatonic, etc.) I will leave these for the interested reader.

Parameters	Best Fit	Definition
ω_b	0.02242±0.00014	..... $\Omega_b h^2$, baryon density today
ω_c	0.11933±0.00091	.....$\Omega_c h^2$, cold dark matter density today
$100\theta_{MC}$ ...	1.04101±0.00029	100× Monte Carlo approximation to r_*/D_A
τ	0.0561±0.0071	..... Optical depth at reionization
n_s	0.9665±0.0038	.....Scalar spectrum power law index
$\ln(10^{10}A_s)$	3.047±0.014	..... Primordial curvature perturbations

Table 1.2: The six free parameters used in the base ΛCDM model and their best fit values determined by *Planck* 2018 TT,TE,EE+lowE+lensing+BAO [11].

1.2 ΛCDM

In the remainder of the text I will be assuming the standard ΛCDM model unless otherwise stated. ΛCDM is today considered the standard model of cosmology. It has been a very successful model with a notably small number of free parameters (see table 1.2). There are however a number of assumptions under its hood which I will take a moment to discuss along with some increasingly relevant difficulties ΛCDM is having with observations.

1.2.1 ΛCDM Assumptions

1.2.1.1 The Copernican Principle Holds

Recall that the Copernican Principle postulates that the Universe is homogeneous and isotropic at the largest scales and results in our use of the FLRW metric. The Universe of course does not satisfy the Copernican Principle at all scales (e.g. the Milky Way galaxy has a definite preferred direction to it) nor does there exist a first principle reason for it to, but at least at scales much larger than ∼100Mpc it seems a reasonable assumption based on observation. However, there are some current considerations that put the isotropic assumption under scrutiny. Particularly, a strong dipole anisotropy is expected in the cos-

mic microwave background (CMB) due to the Sun's peculiar motion relative to the CMB and has been measured by the *Planck* team. They have inferred the Sun's peculiar velocity to be (369.82 ± 0.11)km s^{-1} with respect to the CMB in the direction of the constellation Leo [9]. However, bulk flow estimates have determined a peculiar velocity in a direction in agreement with the CMB dipole but with more than twice the amplitude [12, 13]. A number of additional anomalies have also been observed along the direction of the dipole [14], bringing into question whether the CMB dipole is fully explained by peculiar motion or if something beyond standard cosmology is required. I will however continue to assume the validity of the Copernican Principle and the FLRW metric.

1.2.1.2 General Relativity is Sufficient

Our next assumption is that GR is an accurate description of gravity. The unsuspecting reader may find this statement exceptionally trivial due to GR's repeated success in both high accuracy direct measurements and observed predictions such as gravitational lensing, black holes, and gravitational waves, but the gravitational effect of both dark matter and dark energy without a detectable counterpart has brought some reasonable scrutiny to the theory, giving way to other modified gravity models such as MoND, $f(R)$ gravity, entropic gravity, etc. (see [15] for an extensive review of modified gravity theories). The complexity of modification can vary from simple modifications of GR ($f(R)$, Einstein-Cartan theory,...) or even more drastic overhauls. For example, MoND (Modified Newtonian Dynamics) is a more drastic deviation from GR. It is a dark matter free theory whose original aim was to explain the flattened rotation curves

in galaxies and the baryonic Tully-Fisher relation (BTFR)[6] MoND does this by using Milgrom's relation [16] to modify Newtonian gravity so that

$$|\mathbf{F}_g| = G\frac{mM}{r^2} f(\tfrac{a}{a_0}) \tag{1.17}$$

where $f(\frac{a}{a_0})$ is an empirically determined interpolating function which at sufficiently large accelerations ($a \gg a_0$) approaches unity in order to retain Newtonian gravity, but at sufficiently low accelerations $f(a \ll a_0) \to {}^{a}/_{a_0}$ and

$$|\mathbf{F}_g| \to G\frac{a_0}{a}\frac{mM}{r^2}. \tag{1.18}$$

The transition acceleration is found to be $a_0 \sim 10^{-10}\text{m s}^{-2}$ which due to its numerical proximity to $cH_0 \approx 6 \times 10^{-10}\text{m s}^{-2}$ has been the cause of additional speculation. MoND has been wildly successful in reproducing both the galactic rotation curves and the BTFR up to the scale of galactic super clusters [17], but it still needs improvements before it can match CMB, large scale structure (LSS) formation, and lensing events like the bullet cluster.

Einsten-Cartan (EC) gravity on the other hand is a very minor generalization of classic GR and is in most cases observationally indistinguishable. The key difference in EC gravity is that the affine connection is not assumed to be symmetric or torsion-free resulting in a more general connection than that given by the Christoffel symbols. The allowance of torsion in the manifold contributes and additional torsion tensor, $\mathcal{T}_{\mu\nu}{}^{\rho}$, with an analogous role that the metric has

[6] The BTFR is an empirical relation between a galaxy's asymptotic rotational velocity and the galaxy's luminous mass which goes as $M \propto V^{\alpha}$ where $\alpha \sim 4$. Based on first principles the asymptotic rotational velocity should be dependent on both the dark matter and luminous mass. Baryonic feedback effects are still expected to bring ΛCDM into agreement with the BTFR though.

for curvature. The field equations, obtained by varying the action with respect to the metric and now also the torsion tensor, give both (1.1) as before and

$$\mathcal{T}_{\mu\nu}{}^{\rho} + g_{\mu}{}^{\rho}\mathcal{T}_{\nu\alpha}{}^{\alpha} - g_{\nu}{}^{\rho}\mathcal{T}_{\mu\alpha}{}^{\alpha} = \frac{8\pi G}{c^4}\sigma_{\mu\nu}{}^{\rho} \tag{1.19}$$

where $\sigma_{\mu\nu}{}^{\rho}$ is the spin tensor which serves the same purpose as the stress-energy tensor does for curvature. The importance I want to note here is that the torsion equation, (1.19), is an algebraic combination of the torsion tensor unlike the partial differential equations of (1.1). This means that, although curvature is able to propagate through free space via gravitational waves, torsion has no wave counterpart and would leave no signal in gravitational wave detectors. Furthermore, mass is known to be the source of curvature but it is not clear what the source of torsion is (i.e. what determines $\sigma_{\mu\nu}{}^{\rho}$). A common speculation is that the intrinsic spin of fundamental particles may act as a source, and if this is the case then we are unlikely to observe any torsion signatures outside of a dense, highly correlated spin system. Thus, any deviations in EC gravity from classic GR is safely outside the reach of current observational cosmology. Interestingly though, EC gravity naturally introduces a mechanism to avoid the formation of singularities which is of great cosmological interest since it can avoid the formation of BH singularities and provide a natural mechanism for a "big bounce" cosmology instead of the big bang one. But since it is not relevant to the interests of this text I leave it for the interested reader.

In total, alternatives to GR have not been ruled out and may likely be a better description of gravity. But due to the success of GR, the alternatives must be very close to the form of GR in all relevant cases making it safe to assume that GR is sufficient.

1.2.1.3 The Universe is Evolving from a Hot Dense State

This assumption can be solidly based on two observations: the Universe is expanding and the CMB. If the Universe has been expanding monotonically for a very long time then it is only natural to consider that the Universe was much more dense and hot in earlier times. Today we observe the CMB which is a 2.7K photon bath. At earlier times the photon bath was more condensed and therefore much hotter and if we take it far enough back we could have the photon bath reach any temperature we can imagine up to the Planck temperature where quantum gravity is expected to kick in or at roughly a third of the Planck temperature due to the formation of BHs [18]. Considering hydrogen to be the most abundant element in the present Universe, at some point in the past the temperature would have reached the ionization temperature of hydrogen. Before this temperature (earlier Universe) the Universe must have been opaque due to the abundant compton scattering off of free electrons and hydrogen nuclei while after the temperature (later Universe) the Universe should be transparent allowing the photons to free stream. This is our current understanding of the CMB. The CMB photons were the last photons scattered before hydrogen nuclei could capture the electrons hence the name: surface of last scattering. The transition period is ironically called recombination and sits at a redshift around $z \approx 1100$.

1.2.1.4 There are Five Components to the Energy Content

The base ΛCDM model considers five basic constituents to the energy content of the Universe:

i Ω_Λ, dark energy which behaves like the energy density of the vacuum,

ii Ω_c, cold dark matter which is stable enough for structure formation,

iii Ω_b, baryonic matter which behaves as predicted by the standard model of particle physics plus gravity,

iv Ω_γ, CMB photons (astrophysical photons are less abundant by a factor of 200 [19]),

v Ω_ν, neutrinos with at least one massive flavor.

As a result the Hubble parameter (1.11) can be written as

$$H^2(z) = H_0^2\left[\Omega_{r_0}a^{-4} + \Omega_{m_0}a^{-3} + \Omega_\Lambda + \Omega_k a^{-2}\right] \tag{1.20}$$

where the 0-subscript denotes the value in the present epoch, $\Omega_{r_0} \equiv (\Omega_{\gamma_0} + \Omega_{\nu_0})$ is the radiation component today, and $\Omega_{m_0} \equiv (\Omega_{b_0} + \Omega_{c_0})$ is the matter component today. The presence of dark energy is required due to the accelerated expansion measured in low redshift observations. Dark matter not only explains the missing matter in galaxy rotation curves and lensing observations but also determines the higher ℓ odd peaks in the CMB power spectrum. The requirement for cold dark matter allows for sufficient structure formation since if the dark matter were too hot (i.e. too light) then large scale structures would be more washed out than observed. The need for baryonic matter, CMB photons and neutrinos is self explanatory.

1.2.1.5 The Universe is Spatially Flat

The base ΛCDM model also assumes that the Universe is exactly flat, $\Omega_k = 0$. This is a pretty safe assumption for two reasons: *Planck* measures a spatially flat Universe, $\Omega_k = 0.0007 \pm 0.0019$ (*Planck*+lensing+BAO [11]) and standard inflationary models generally drive the Universe exponentially towards flatness.

1.2.1.6 The Initial Fluctuations are Random

And finally, the last assumption I will mention is that the initial density fluctuations in the early universe were Gaussian, adiabatic, and nearly scale-invariant. This assumption is primarily one of ease as there are no physical processes requiring them except for standard inflation models which drive the Universe towards such a configuration.

1.2.2 The Many Successes and Failures of ΛCDM

ΛCDM has been successful on many fronts. It predicted the right size of the baryon acoustic oscillations (BAO) which were first observed by the Sloan Digitial Sky Survey (SDSS) [20] and predicted the CMB polarization anisotropy detected by DASI [21]. ΛCDM can also explain the accelerating expansion [22], the spectrum of large scale structure [23], the abundance of light elements [24], and the power spectrum of the CMB anisotropies [11]. But dissonance remains in the field due to a few resilient tensions with observation.

The most striking issue is of course the cosmological constant problem marked by the fact that the theoretically expected value for Λ from electroweak contributions to the vacuum energy is 55 orders of magnitude larger than the observed value [8]. Since we do not have a firm grasp on dark energy the issue may be there or it may be that somewhere in more extensive QFT calculations a large cancellation may occur (which would then cause a fine-tuning problem). For the time being we have posted this problem on the cosmological refrigerator and promised to get around to it someday after we have a better grasp on dark energy and dark matter.

Still other tensions persist. For brevity I mention only a few of the more sig-

nificant tension ($\geq 2\sigma$, which can often be viewed as significant in cosmology), but I refer the reader to [25–27] for extensive reviews of further tensions and anomalies.

Hubble Tension [$> 4\sigma$] The *Planck* 2018 [11] CMB observations have constrained the spread in H_0 values to a very narrow window of $H_0 = (67.4 \pm 0.5)$km s^{-1}Mpc^{-1} while the cosmic distance ladder measurements from the SH0ES team [28] has obtained a wider but significantly different window of $H_0 = (73.04 \pm 1.04)$km s^{-1}Mpc^{-1}. An up-to-date collection of H_0 estimates from multiple observations is shown in figure 1.2. The top section of the plot lists the high z constraints on H_0 from CMB and BBN (Big Bang Nucleosynthesis) observations while the remainder lists the low z observations. Systematic errors may of course inflate the tension, but none have yet been found that would cause a discrepancy to this degree (see [29] for a nice discussion on both low and high z systematics).

S_8 **Tension** [$2 - 3\sigma$] The strength in matter clustering can be parameterized by the $S_8 \equiv \sigma_8\sqrt{\Omega_m/0.3}$ parameter where σ_8 is the amplitude of mass fluctuations on a fiducial scale of $8h^{-1}$Mpc. If one has a good level of confidence in Ω_m then the tension can also be referred to as a σ_8 tension. The *Planck* TT,TE,EE+lowE+lensing constraints place $S_8 = (0.832 \pm 0.013)$ while weak lensing, globular clusters, galaxy cluster abundances, and redshift space distortions all prefer a lower value with weak lensing alone around $S_8 = (0.735 \pm 0.044)$. Physically it seems that the CMB observations are predicting more clustering than is observed.

Cosmic Dipole [$2 - 5\sigma$] The tension in the cosmic dipole has already been mentioned in the previous section but for completeness I will briefly reiterate

it here. A dipole anisotropy in the CMB has been measured by both the WMAP and *Planck* teams in agreement with the direction of the Sun's peculiar velocity with respect to the CMB rest frame. However, bulk flow measurements show that the dipole amplitude should be more than twice the value measured on the CMB (i.e. we seem to be going faster than what the dipole shows).

Cosmic Birefringence [2.4σ] Recently a non-zero birefringence has been observed in the *Planck* 2018 CMB polarization anisotropies at the 2.4σ level. A cosmic birefringence, if confirmed, would hint at parity violation in the early Universe which standard ΛCDM is not yet able to explain.

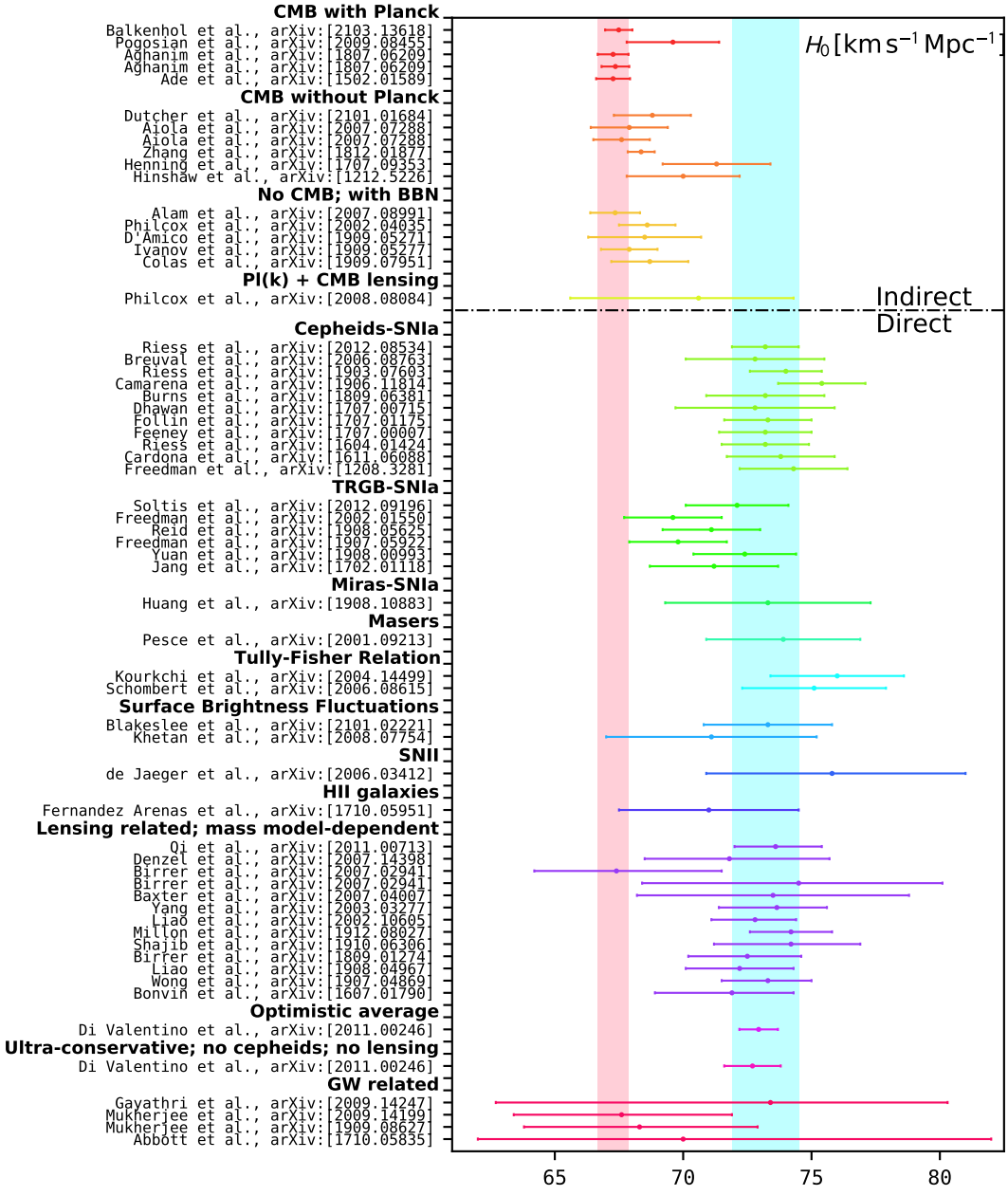

Figure 1.2: A non-exhaustive list of H_0 measurements. The pink and blue bands correspond to the H_0 values from *Planck* 2018 [11] and the SH0ES team [28], respectively. Referenced papers are listed on the side with their arχiv identifier and correspond to [11, 30–85]. Code for the repoduction of similar plots has been made available at `http://github.com/lucavisinelli/H0TensionRealm` by the authors of [29].

1.2.3 Alternatives to ΛCDM

The above tensions have put more interest into modified ΛCDM models. There is a continuous flux of alternative models going in and out of favor as our cosmological constraints improve in accuracy and robustness. Below I describe a few commonly discussed models including two models which took the silver (early dark energy) and gold ($m_e\Omega_k\Lambda$CDM) in the H_0 Olympics [86].

$\Omega_k\Lambda$CDM This is the minimal extension to ΛCDM taken when one drops the assumption that $\Omega_k = 0$. The *Planck* team has shown that in $\Omega_k\Lambda$CDM a small but finite $\Omega_k = -0.044^{+0.018}_{-0.015}$ is preferred by the TT,TE,EE+lowE data set and $\Omega_k = 0.0007 \pm 0.0019$ is preferred by +lensing+BAO data set [11]. By itself the model does not reduce any of the tensions significantly.

w_aCDM Standard ΛCDM treats dark energy as a cosmological constant corresponding to a constant EoS $w = -1$. w_aCDM instead considers

$$w = w_0 + (1 - a)w_a \tag{1.21}$$

thus giving dark energy a phenomenologically dynamical behavior. Using CMB, BAO, and type Ia supernovae combined, *Planck* 2018 finds preferred values of $w_0 = -0.957 \pm 0.080$ and $w_a = -0.29^{+0.32}_{-0.26}$ with minor reduction in the S_8 and H_0 tensions [11].

Early Dark Energy (EDE) A run of the mill EDE model is usually one with a frozen-in scalar field (i.e. $w \approx -1$) sitting high enough on its potential that it is able to momentarily provide a significant fraction ($\sim 10\%$) of the total energy density prior to recombination. At this point the field unfreezes and transitions through the potential such that $w \geq 1/3$ which allows its

energy density to decay away rapidly. A common example in the literature uses the potential

$$V(\Theta) = m^2 f^2 \left[1 - \cos(\Theta)\right]^n \tag{1.22}$$

where $\Theta \equiv \phi/f$ is a re-normalized field variable ranging from $-\pi \leq \Theta \leq \pi$. The freeze-in mechanism, provided by the high Hubble friction at early times, finishes when $H < m$ at which point the field behaves like a fluid with EoS $w = (n-1)/(n+1)$. This choice of EDE does not replace the cosmological constant however.

$m_e\Omega_k\Lambda$CDM This model is similar to the $\Omega_k\Lambda$CDM model discussed previously, however a time-dependent electron mass is added in order to modify recombination as well. The $m_e\Omega_k\Lambda$CDM model has been shown to reduce the Hubble tension to below 2σ with the combined TT,TE,EE+lowE+BAO and Pantheon supernovae data set [87]. This is discussed in greater detail in chapter 3.

For a more exhaustive and modern list of alternative models along with their present standing with observations see [29, 86].

1.3 Low z Cosmology

The low redshift Universe provides a unique model independent window into constraining cosmology. This is through the application of Hubble's law, $v = Hd_L$, with the luminosity distance given by $d_L \equiv \sqrt{4\pi/L}$. It is a bit more useful however to expand the relation as a power series in redshift:

$$H_0 d_L = z + \frac{1}{2}(1 - q_0)z^2 - \frac{1}{6}(1 - q_0 - 3q_0^2 + j_0)z^3 + \mathcal{O}(z^4) \tag{1.23}$$

where q_0 and j_0 are the current (i.e. $z = 0$) values of the deceleration and jerk parameters given by

$$q \equiv -\frac{\ddot{a}a}{\dot{a}^2} = \frac{(1+z)}{H}\frac{\mathrm{d}H}{\mathrm{d}z} - 1 \tag{1.24}$$

$$j \equiv \frac{\dddot{a}}{aH^3} = \frac{1}{(1+z)}\Big(-(1+z)\frac{\mathrm{d}q}{\mathrm{d}z} - q + 2q^2\Big). \tag{1.25}$$

When assuming a particular cosmological model such as ΛCDM it will be much more convenient to use the general relation

$$d_L = (1+z)\int_0^z \frac{cdz}{H(z)}, \tag{1.26}$$

since it can be easily extended to much higher redshifts, but for now I will continue to consider (1.23). For agnostic concreteness I will take the central value for today's rate of expansion, $H_0 \approx 70\mathrm{km\ s^{-1}Mpc^{-1}}$, unless stated otherwise. A general expression for j_0 is a bit complicated but it is easy to see from (1.14) that assuming a spatially flat cosmology (i.e. $\sum_i^n \Omega_{0_i} = 1$) then today's value of the deceleration parameter has a simple analytic expression:

$$q_0 = \frac{1}{2}\sum_i^n \Omega_{0_i}(1+3w_i). \tag{1.27}$$

As an exercise, if I consider a radiation dominated Universe ($w = 1/3$) then $\{q_0, j_0\} = \{1, 1\}$. And if I consider a matter dominated Universe ($w = 0$) then $\{q_0, j_0\} = \{1/2, 0\}$. So if we have a mixed Universe of radiation and matter[7] then $q_0 \in [1/2, 1]$ and $j_0 \in [0, 1]$.

In order to test what kind of Universe we are in we just need to measure the luminosity distance and redshift of very distant objects. In principle the deter-

[7] As any sane person would prior to the 1990's.

mination of redshift is straight forward. If we have enough telescope time we can do a spectrographic analysis where we sample the whole spectrum of the object and measure how far shifted it is. Spectrographic redshifts are very accurate but cannot always be done due to time constraints. Photometric redshifts, on the other hand, can be done much faster as they are determined by comparing the brightness of an object through several wide bandpass filters, and as a result they are usually less accurate. But, due to advancements in large field surveys such as the Sloan Digital Sky Survey (SDSS) and the Legacy Survey of Space and Time (LSST) (soon to come online), photometric redshifts are now quite reliable. It is however much more difficult to determine the luminosity distance to an object. In the following sections I will discuss in detail how d_L can be measured but for the immediate discussion it should suffice for now to say that we can determine both redshifts and luminosity distances to type Ia supernovae pretty accurately. Using supernovae data from the Pantheon survey [88] reaching up to $z = 2.26$, we can see that $q_0 \in [1/2, 1]$ is strongly disfavored (see figure 1.3). The supernovae instead prefer a $q_0 < 0$ which can be explained by a Universe dominated by a fluid with $w < -1/3$. This was first observed by the High-Z Supernova Search Team [22] with supernovae only extending up to $z = 0.62$.

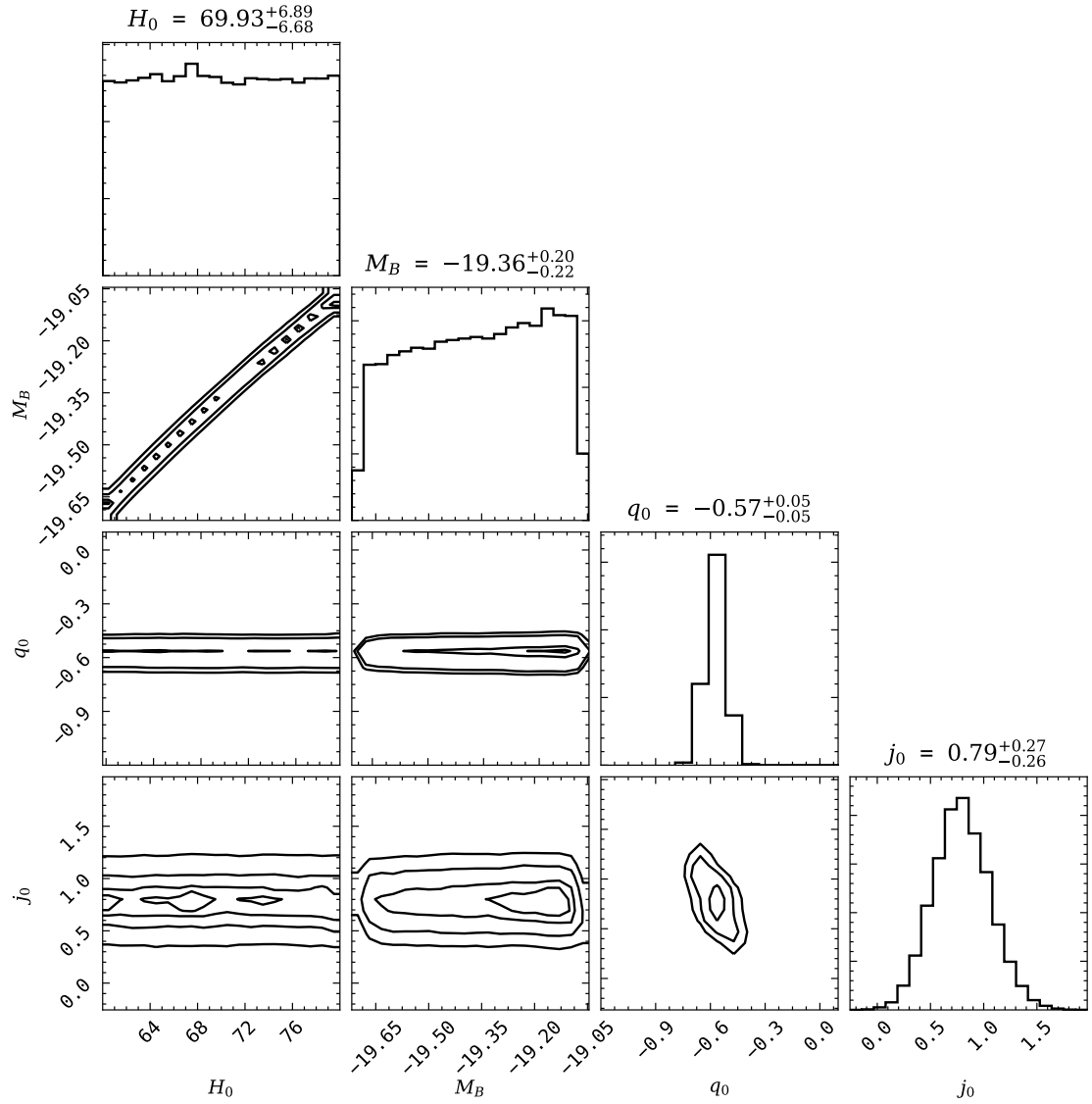

Figure 1.3: MCMC fits of the Pantheon [88] supernovae data to (1.23). An accelerated expansion ($q_0 < 0$) is favored by over 11σ while a mixture of radiation-matter domination is disfavored by over 21σ. M_B is the absolute magnitude at peak brightness of the type Ia supernovae in the B-band which we see is degenerate with H_0. The degeneracy can be broken by anchoring the supernovae with Cepheid variables or stars in the tip of the red giant branch and will be discussed later.

The next relevant question is: how do we reliably measure d_L without assuming a cosmological model for $H(z)$? The most basic approach is the one em-

ployed by Edwin Hubble in his work on the expanding Universe [89]. Today we can consider this an early example of the current cosmic distance ladder. Hubble had used geometric distances to calibrate the luminosity of Cepheid variables from which he was able to determine d_L for more distant Cepheid variables. The details of these measurements I will go into shortly. The typical cosmic distance ladder today does something similar but then uses the Cepheid variables to calibrate type Ia supernovae (SNIa) which are then used to measure d_L. In total this forms a three rung distance ladder. The purpose of calibrating SNIa to Cepheid variables which are in turn calibrated with geometric distances is important in order to reduce the degeneracy between the brightness of the object and H_0. This degeneracy can clearly be seen in the uncalibrated SNIa of figure 1.3. The simplicity of the cosmic distance ladder has made it a key tool in measuring the expansion of the Universe, but as is clear for anyone who has climbed a ladder, any small wiggle at the base of the ladder can cause great concern at the top. That is to say, any small error in the geometric-Cepheid calibration could cause significant systematic error in the high redshift SNIa. However, alternative ladders have been constructed using the tip of the red giant branch (TRGB) in place of Cepheid variables providing an independent calibration for the type Ia supernovae. Since both ladders are in agreement (see figure 1.2) it is less likely that systematic errors in either Cepheids or TRGB calibrations are playing a significant role.

The Hubble diagram is another tool for measuring the expansion rate. It is almost identical to the cosmic distance ladder except that it does not require the anchoring to lower redshift objects. In general Hubble diagrams can be applied to a wider class of objects since there is no prerequisite for using classes of objects with coincident positions like in the calibration of SNIa with Cepheids.

Without the anchoring to lower redshift objects, a Hubble diagram is insensitive to H_0, but can still be useful in probing the evolution of the expansion rate.

In the next few sections I will break the distance ladder into two parts: geometric distances and standard candles. The latter part will cover the physics of Cepheid variables, TRGBs, and SNIa

1.3.1 Geometric distances

The most natural method for measuring distances is through parallax which which measures the difference between images of a single object taken at two different viewing angles. For instance, the binocular vision found in many predatory animals provides an ability to gauge the distance to an object. This is due to the coordination of the two spatially separated eyes focusing on the same point in space and providing two different viewing angles. The average separation between a human's eyes for example can provide an accurate distance gauge up to a few hundred meters. The relation between the object's distance, d, and the viewing angle, θ, when the object is much further than the separation of detectors, R, (e.g. when an object is much farther than the separation of a human's eyes) goes as

$$d = \frac{R}{\theta}. \tag{1.28}$$

Thus, measuring greater distances can be done by increasing the separation distance or by decreasing the viewing angle (i.e. increasing the telescope resolution). As long as the angular position of the object we want to look at does not change significantly within one Earth year then the maximum we can increase R within reason is up to the orbital radius of Earth around the Sun. This is illustrated in figure 1.4) where an image of the object is taken at least twice per year

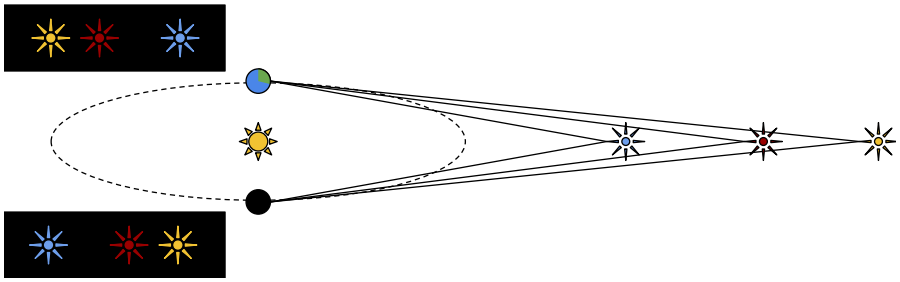

Figure 1.4: Parallax measurements to gauge the distance to astronomical objects. Over a six month interval of the Earth's orbit around the Sun the viewing angle is maximized giving the best measure of parallax. But still, as we can see by comparing the apparent differences in position between the yellow and red stars to that of the blue star, eventually the parallax effect will be below the resolution of our telescopes.

when the object-Earth-Sun system forms a right triangle. The Gaia satellite, our most accurate parallax survey to date, was designed to take an average of 14 images of each observed object per year. At this point, getting more distant parallax measurements is just a game of minimizing θ. For Gaia DR2 [90] the angular resolution for parallax measurements was near the 0.1 milli-arcseconds which corresponds to a maximum measured distance on the order a few kilo-parsecs. The Gaia DR3 release has fractionally better resolution. Much farther geometric distances can be made in specialized cases such as the precise distance to NGC 4258 using water masers. But since the majority of geometric distances are done through parallax measurements I will not spend time discussing these other cases.

If we take $H_0 \approx 2.3 \times 10^{-7} kpc^{-1}$ ($c \equiv 1$) and q_0 to be of order unity then to get q_0 to within 10% accuracy we would need an angular resolution of about 10 nano-arcseconds. Since Gaia DR2 can only measure parallax to within 0.1 milli-arcseconds q_0 is still out of range for parallax measurements and will be for quite some time. Furthermore, at a few kilo-parsecs two issues arise for

determining q_0:

- peculiar redshift dominates so the measured z would not correspond to what we assume in (1.23),
- any objects within a few kilo-parsecs would be gravitationally bound to the Milky Way galaxy making them insensitive to the expansion rate.

For these reasons we require a higher redshift probe in order to test cosmology.

1.3.2 Standard Candles

Historically, standard candles were exactly that: a candle made of a particular wax and wick that could produce a standard brightness to compare other candles to – similar in principle to the standard meter and kilogram. A more modern example would be a 60W light bulb attached to a 12V battery since the luminosity of all such systems would be identical to within manufacturing errors. The importance of standard candles in distance measurements is that, due to the radiation flux dropping off as r^{-2}, by comparing the dimness of a remote standard candle to how bright it should be you would be able to determine its distance. And like the geometric distance determinations, standard candle distances can be made independent of a cosmological model.

As a short aside I must first introduce the magnitude scale that is flagrantly used in astronomy and here. The magnitude scale is a logarithmic parametrization of flux. For historical reasons the scale is defined as

$$m - M \equiv -2.5 \log F/F_0 = 5\big(\log(d_L) - 1\big) \tag{1.29}$$

where m is the apparent magnitude (i.e. observed brightness), M is the abso-

lute magnitude (i.e. how bright the object would be if measured at a fiducial distance of 10pc), F is the observed flux, and F_0 is likewise the flux that would be measured at a distance of 10pc from the object. In this form it is assumed that d_L is measured in parsecs. As we can see from (1.29), brighter objects have more negative magnitudes. For example, the Sun has an apparent magnitude in the optical band of -26.74 when viewed from Earth's orbit, but has an absolute magnitude of +4.83 at 10pc [8]. We can compare this to the optical band apparent and absolute magnitudes of Betelgeuse determined to be +0.5 [91] and -5.85 [92], respectively. So Betelgeuse is much brighter than the Sun but due to our proximity to the Sun we observe the Sun to be much brighter. One additional notation we wish to make is the distance modulus, $\mu \equiv m - M$, which is not a particularly enlightening notation but it is commonly used in the literature that I will be referring to.

However, there are very few classes of astronomical objects so consistent in form that they could be considered a standard candle (with the possible exception of TRGBs). Instead standard*izable* candles are commonly used. These are types of objects which may not be consistent in brightness but has been shown to have a reliably predictable brightness based on the measurement of another physical parameter. Currently we have three main standard/standardizable candles: Cepheid variables, TRGBs, SNIa.

1.3.2.1 Cepheid Variables

Our working model for Cepheid variables is that they are very regular, non-variable, yellow giants with an outer layer of singly ionized helium, He^+. Radiation pressure from the star pushes the He^+ layer outwards while simulta-

[8] https://nssdc.gsfc.nasa.gov/planetary/factsheet/sunfact.html

neously ionizing it into He^{++}. Since He^{+} is more opague than He^{++}, the ionization effectively reduces the radiation pressure allowing helium to both fall back towards the star and to cool back down below the ionization temperature to reform He^{+}. The process forms a closed loop and is able to repeat itself many times. Meanwhile, a distant observer sees a yellow giant star with a periodic brightening (He^{++} phase) and dimming (He^{+} phase). Figure 1.5 shows the *i*-band light curve of a Cepheid variable located in the Milky Way. Since the radiation pressure is the driving force in this process, the period of oscillations can be directly tied to the brightness of the star; thus, measuring a Cepheid variable's period one can directly determine its brightness. The authors of [94] used parallax measurements to calibrate the period-magnitude relation in the V-band and obtained

$$\langle M_V \rangle = -2.81 \log(P) - 1.43. \tag{1.30}$$

For example, if we ignore the difference in bands, the Cepheid in figure 1.5 has a period of roughly $P \approx 8.75$days with a mean magnitude of 13.9 which would give an absolute magnitude of $\langle M_V \rangle \approx -4$. Using (1.29), luminosity distance to the Cepheid is then $d_L \approx 39$kpc, within the Milky Way disk as expected. Additional color corrections can make for a more accurate distance but for a back-of-the-envelope calculation this is not bad.

The most distant Cepheid variable detected so far is in the M100 galaxy at a distance of $d_L \approx 16.8$Mpc, but even at this distance, q_0 is still below our sensitivity.

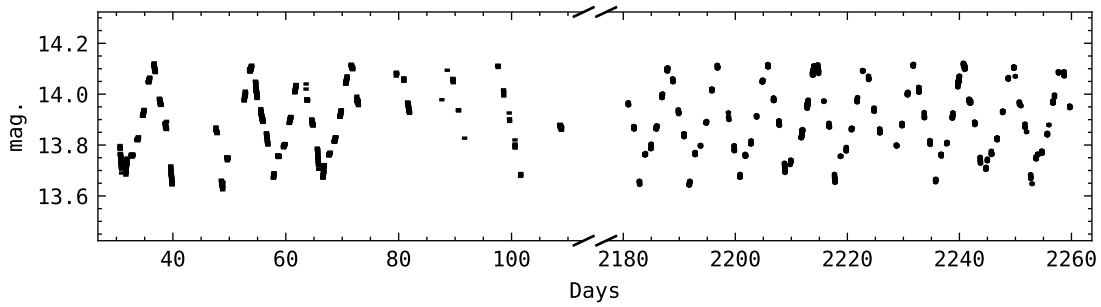

Figure 1.5: The *i*-band light curve (with errorbars) of a Cepheid variable located in the Milky Way disk (taken from the OGLE III survey [93]). The periodicity of the magnitude is quite apparent.

1.3.2.2 Tip of the Red Giant Branch

TRGBs were first proposed for distance measurements in 1983 [95] and can be considered a true standard candle. The TRGB is formed by the transition of red giant stars from the red giant branch into the horizontal branch of the Hertzsprung-Russell (HR) diagram. The evolution starts with an old red giant which has converted most of its core's hydrogen into helium. Not yet having the necessary temperature to ignite helium fusion the star compresses and begins fusing hydrogen layers surrounding the inert helium core causing the star to brighten and climb the red giant branch. If the star is $\lesssim 2M_{\odot}$ the helium core will first reach the electron degeneracy pressure and then continue heating up to the temperature necessary to fuse helium into carbon – growing more luminous along the way. In this case, the entire degenerate helium core will almost simultaneously undergo helium fusion causing a bright so-called *helium-flash* before quickly descending into the dimmer horizontal branch[9]. What this means observationally is that if we were to make an HR diagram of the stellar population

[9] In more massive red giants ($\gtrsim 2M_{\odot}$) the helium fusion temperature will be reached before electron degeneracy pressure causing the star to gradually transition over to the horizontal branch.

in a galaxy and focus on the red giant branch then we would see a large population of red giant stars climbing the red giant branch up to a hard cutoff in luminosity before descending into the horizontal branch – the hard cutoff being those stars just before their helium-flash. As was discussed in [95] and later works, this luminosity peak in the HR diagram forms well defined standard candle. Figures 8 and 11 of [96] provide very nice examples of this section of the HR diagram for both the large and small Magellanic clouds, respectively.

Furthermore, the TRGB luminosity reaches an I-band magnitude of approximately -4 putting its use as a distance indicator in the same redshift range as Cepheid variables.

1.3.2.3 Type Ia Supernovae

SNIa are formed by inordinately bright stellar explosions which quickly climb up to a peak brightness of $M_B \approx -19$ and decays away over the following couple of months. They are bright enough to outshine their host galaxy and common enough that we would expect on average one to occur in the Milky Way alone every 50 years[10]. The true nature of the mechanism behind SNIa is a bit of a mystery except that we are pretty certain a compact object is at the core [97]. As such I will discuss the most likely scenario considered by the supernova community.

The progenitor of a SNIa is expected to be a binary system containing either two carbon-oxygen white dwarfs (WDs) or a single WD with a main sequence companion star. In either case, the primary WD will accrete matter from its companion. The accretion process increases the primary WD's mass towards

[10]The last SNIa observed in the Milky Way was SN1604 in the year 1604. The Milky Way is long over due for a SNIa explosion and many a astronomy students have prolonged their Ph.D. thesis in hopes that one will go off in time.

the Chandrasekhar limit of $1.4M_{\odot}$ after which the outward electron degeneracy pressure is not enough and gravitational collapse will drive the WD to form a neutron star. But at a mass of approximately $1.37M_{\odot}$ carbon burning is ignited and a deflagration front pushes its way through the outer layers (not necessarily in a spherically symmetric manner). Meanwhile, the core continues to heat but, since the WD does not have the ability to regulate heat, a runaway thermonuclear reaction occurs causing a release of $\sim 10^{51} ergs$ or $1 foe$[11]. Surprisingly, it is not the explosion itself that forms the prototypical light curve of a SNIa but instead the radioactive decay of elements produced in the explosion (mostly those in the Fe-group [98]).

The consistency in the amount of nuclear energy produced in the explosion causes the brightness of the decay to be nearly uniform enough to consider SNIa as standard candles but variations occur requiring some phenomenological corrections. The most significant correction was noted by Mark Phillips [99] and relates the peak brightness of the light curve, M_B, to the decrease in magnitude over the following 15 days, Δm_{15} (see figure 1.6). Both the choice in using the B-band and 15 days were due to these providing the lowest dispersion. Today the dispersion in the relation is found to be $\sim$ 0.1dex [100].

Due to their brightness, SNIa can be observed at great distances. The Pantheon survey [88] uses SNIa up to $z = 2.26$ which is more than enough to start probing q_0. Already at $z \approx 0.4$ the Supernova Search Team [22] was able to detect the accelerated expansion with $q_0 < 0$.

At present the population of SNIa with science worthy light curves is not expected to reach far past $z = 2$. There is no reason not to expect SNIa at much larger distances, even up to $z \approx 12$ when the first stars began forming, but

[11] A common notation in supernova literature. Fifty One Ergs (foe).

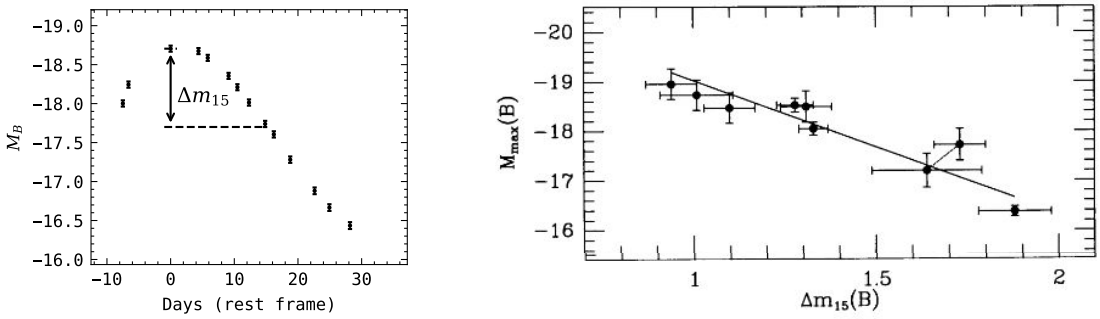

Figure 1.6: *Left*: The light curve of SN2021pit from the SWIFT survey showing how Δm_{15} is defined. We can estimate a $\Delta m_{15} \approx 1$ and $M_B \approx -18.75$. *Right*: Modified plot from Philips' original paper [99] showing the tight relation between peak brightness and Δm_{15}. SN2021pit falls very close to the best fit line given our rough estimates.

observationally they will not provide a statistically relevant source above $z = 2$ for a long time. As a result, cosmology beyond this would require a much brighter class of objects.

1.4 An Introduction in Inflation

The ΛCDM model has tested successful against data all the way back to the synthesis of light elements during the BBN when the Universe was only 10^{-2}s old. The model can also give convincing description to the very early Universe back when the Universe was only $10^{-34}s$ old. There are however some problems ΛCDM cannot address. For example, the entire CMB, including sections that hold polar opposite positions in the sky, is a nearly perfect thermalized system to 1 part in 10^5. This is made even more impressive by the fact that the particle horizon at recombination makes up $\sim 1\,\text{deg}$ on the CMB map. No causal process (like Compton or Thompson scattering) could have brought all of these remote regions of space into thermal equilibrium. The inflationary model how-

ever provides a simple physical mechanism for which thermal equilibrium is a natural byproduct. Inflation is expected to describe the very early phase of the Universe, $t < 10^{-34}$s, and requires a vacuum energy dominated phase in the form of a scalar field called the inflaton field. The Lagrangian of the inflaton must be chosen such that its EoS is $w < -1/3$ to drive an accelerated expansion phase, but usually the simple picture is discussed in terms of the field having $w = -1$ so that Ω_{inf} is constant and (1.14) reduces to an exponential growth in the scale factor, $a \propto \exp[2H^2 t]$. Meanwhile, the horizon size, $\propto H^{-1}$, remains constant. Thus, much of the Universe could have been causally connected and in thermal equilibrium before inflation then inflation kicks in and everything is expanded out beyond the horizon which breaks their causal connection. With the same mechanism inflation can also explain the flatness and monopole relic problems but I leave this for the interested reader (see [101] for a nice discussion on these problems).

The trick is then to construct an inflaton field such that the necessary expansion can occur but also naturally drops off to give way to ΛCDM. I will describe two well known inflationary models that can do just this: standard inflation and k-inflation.

1.4.1 Standard Inflation

Consider the universe to be dominated by a spatially uniform scalar field, ϕ, in a potential, $V(\phi)$, giving

$$\mathcal{L} = \frac{1}{2}\dot{\phi}^2 - V(\phi). \tag{1.31}$$

For reasons that will be described in a moment, our choice of potential is one that has a nearly flat plateau which then quickly drops into a potential well.

The placement of the well determines the energy we want inflation to stop so since ΛCDM works up to 10^{-34}s, corresponding to an energy scale of 10^{14}GeV, I can center the potential well at $\phi \approx 10^{14}$GeV (see figure 1.7 for a schematic of the potential). To leading order, as long as the slow-roll conditions (to be discussed) are met then the inflationary mechanism is insensitive to finer details in the potential. The equation of motion (EoM) for the field can be obtained by varying the action with respect to ϕ:

$$\ddot{\phi} + 3H\dot{\phi} + V'(\phi) = 0, \tag{1.32}$$

with the prime notation noting derivatives with respect to ϕ. This just describes a damped driven oscillator with the Hubble parameter serving as the damping coefficient (*Hubble friction*) and the field gradient as the driving force. An additional damping term, $\Gamma\dot{\phi}$, can also be put in by hand in order to account for the condensation of ϕ-particles that can then decay into other fields coupled to ϕ thereby reducing the energy stored in the vacuum. This will lead to the necessary reheating process that will give us back a hot early universe after the super cooling from the exponential expansion. Its neglect however will not change the following discussion so we drop the term for simplicity.

The energy-momentum tensor for a simple scalar field is just

$$T^{\mu\nu} = \partial^{\mu}\phi\partial^{\nu}\phi - \mathcal{L}g^{\mu\nu}, \tag{1.33}$$

which when compared to (1.8) readily gives the EoS for the field

$$w \equiv \frac{p}{\rho} = \frac{\frac{1}{2}\dot{\phi}^2 - V(\phi)}{\frac{1}{2}\dot{\phi}^2 + V(\phi)}. \tag{1.34}$$

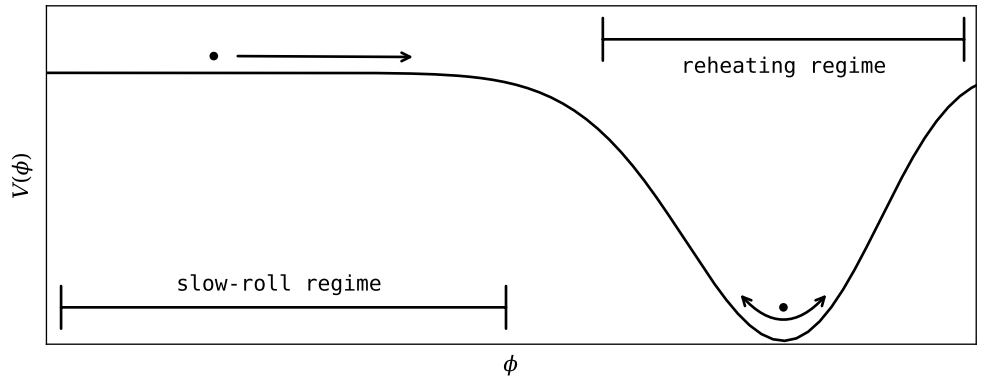

Figure 1.7: A schematic of a common inflationary potential. The plateau to the left helps to ensure a slow-roll regime and an accelerated expansion. Then a quick drop into a potential well, resulting in oscillations about the minimum, leads to the necessary reheating process.

Given that H is very large in the early Universe the Hubble friction slows the motion of the field so that $\dot{\phi} \approx 0$ and $w \approx -1$ providing an exponential-like growth in the scale factor. It is useful at this point to introduce the first slow-roll parameter

$$\epsilon \equiv -\frac{\dot{H}}{H^2} < 1 \tag{1.35}$$

which corresponds to a $w < -1/3$ in (1.14); thus, the first slow roll condition ensures an accelerated expansion. We can also pose the first slow roll condition in terms of the logarithmic gradient of the potential:

$$\epsilon_V = \frac{M_{Pl}^2}{2}\frac{V_{,\phi}^2}{V^2}. \tag{1.36}$$

In the single field inflationary model we have $\epsilon = \epsilon_V$, but this is not a general equivalence and the two definitions can differ based on our choice of model.

The next thing to ensure is that the slow-roll regime lasts long enough. We can do this by requiring $\ddot{\phi} \ll H\dot{\phi}$ which is equivalent to the Hubble friction dominating the motion of the scalar field. This introduces our second slow roll

parameter:

$$\eta \equiv \frac{\dot{\epsilon}}{H\epsilon} \tag{1.37}$$

with the constraint $|\eta| \ll 1$. This can also be viewed as requiring the growth in ϵ during a Hubble time to be small. In the case $\epsilon \ll 1$ we can reduce η to

$$\eta = \frac{\ddot{\phi}}{H\dot{\phi}} \tag{1.38}$$

showing that if we are slowly rolling then an $\eta \ll 1$ will ensure that we remain that way for many Hubble times. A host of additional parameters are used in the inflation literature. Some differ by mere convention while others involve more subtle arguments. For now, my choice of definitions for ϵ, ϵ_V, and η will suffice.

I have so far been careless with my use of time. After all, everything so far in this section must have occurred within a time span of $\sim 10^{-34}$s. That's about 100million times faster than it takes light to cross the length scale of a quark. So, in usual inflationary style, we instead use the number of e-folds, N, to measure how long the slow-roll process has occurred. We define the number of e-folds as

$$N \equiv \ln\left(\frac{a}{a_i}\right) \tag{1.39}$$

where a_i is the scale factor at the beginning of inflation. To estimate the number of e-folds necessary we can consider the largest perturbation modes re-entering our horizon today, $k_0 \approx a_0 H_0$. Inflation must have lasted long enough to push these modes out of the horizon, and, since the horizon has been expanding since the end of inflation, the extent to which these modes were pushed out can be determined by how much the horizon had to expand to get them back in. That is

to say, the number of e-folds should be approximately given by how much our horizon has expanded since inflation. For a quick back of the envelope calculation we can take the ratio of the temperature at reheating, $T_{RH} \approx 10^{10}$GeV, to that of the 2.7K CMB temperature today ($T_0 \approx 10^{-13}$GeV):

$$N \approx \ln\left(\frac{T_{RH}}{T_0}\right) \approx 52. \tag{1.40}$$

The generally quoted number is nearer to 60 with a rough range of $N \in [50, 70]$.

1.4.2 k-inflation

An alternative to the standard inflationary model was proposed in [102] where both the slow roll and accelerated expansion conditions sought after by standard inflation could still be met in the absence of a potential energy term if one considers non-standard kinetic terms. To see this we consider the Lagrangian density

$$\mathcal{L} = P(X, \varphi) \tag{1.41}$$

where $X \equiv -(\partial\varphi)^2/2$ is the canonical kinetic term. For concreteness, perhaps $P(X, \varphi)$ admits the expansion

$$P(X, \varphi) = \frac{1}{2}C_1(\varphi)X + \frac{1}{4}C_2(\varphi)X^2 \tag{1.42}$$

where it is assumed that $C_2(\varphi) > 0 \forall \varphi$ in order to ensure a positive energy density while $C_1(\varphi)$ is free to vary between positive and negative values. The important note here is that there is no potential term in the Lagrangian. In the same manner as was done for the standard inflationary model, the EoS for the

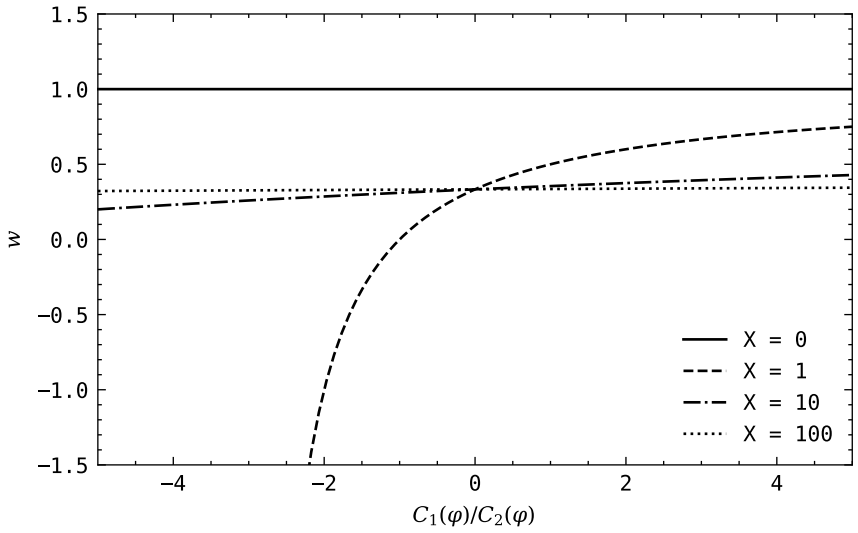

Figure 1.8: Equation of state parameter for a $P(X, \varphi)$ theory with respect to the ratio of the expansion coefficients. In the limit $X \to 0$ the field behaves like a free scalar field and as $X \to \infty$ the field behaves like radiation ($w \to 1/3$). But for intermediate X the EoS can be sufficiently negative to drive accelerated expansion.

field can then be written as

$$w = \frac{P}{\rho} = \frac{C_1(\varphi)X + C_2(\varphi)X^2}{C_1(\varphi)X + 3C_2(\varphi)X^2} = \frac{C_1(\varphi)/C_2 + X}{C_1(\varphi)/C_2 + 3X} \tag{1.43}$$

which can take on sufficiently negative values for $C_1(\varphi) < 0$, providing an accelerated expansion without a potential energy term. Figure 1.8 shows the EoS where it is clear that for reasonable values of X a $w < -1/3$ can be reached.

The Friedmann equations for the general $P(X, \varphi)$ theory can be written as

$$H^2 = \frac{1}{3M_{Pl}^2}(2XP_X - P), \tag{1.44}$$

$$\frac{\ddot{a}}{a} = -\frac{1}{3M_{Pl}^2}(XP_X + P). \tag{1.45}$$

For brevety we have dropped the comma notation for derivatives so that $P_X \equiv$

$\partial P/\partial X$, $P_{XX} \equiv \partial^2 P/\partial X^2$, and so on. The EoM for the field is then

$$\ddot{\varphi} + 3H\dot{\varphi} + \dot{\varphi}\frac{\dot{P}_X}{P_X} - \frac{P_\varphi}{P_X} = 0 \tag{1.46}$$

in which we have gained an additional friction term driven by the time variations in our $C_{1,2}(\varphi)$ coefficients. Likewise, the first slow roll parameter is found to be

$$\epsilon = \frac{3}{2}\Big(1 + \frac{P}{2XP_X - P}\Big), \tag{1.47}$$

which, if the slow-roll condition is applied, $\epsilon < 1$, corresponds to

$$P < -XP_X. \tag{1.48}$$

The second slow roll parameter, η, is defined as before, but it is useful at this point to also introduce the parameter

$$\tilde{\kappa} \equiv \frac{\dot{P}_X}{HP_X} \tag{1.49}$$

which quantifies the deviation from the canonical kinetic term. For instance, if $\tilde{\kappa}$ is small then the deviation from $P(X, \phi) = X$ would have to be a slowly varying function of time and can be ignored. I can then rewrite the EoM in terms of the slow roll parameters

$$\ddot{\varphi} = \frac{1}{2}(\eta - 2\epsilon - \tilde{\kappa})H\dot{\varphi}. \tag{1.50}$$

Part II

Publications

Chapter 2

Quasar Standard Candles

In this chapter I discuss my work in using quasars as distance indicators [1] and collaborative work done on apparent biases in the ΛCDM model for high redshift probes [2, 3].

2.0.1 Quasar Introduction

Quasars (QSOs) are known for two basic characteristics: they are highly variable in luminosity (see figure 2.1) and their spectrums are highly redshifted compared to how bright they are observed. When QSOs were first observed it was expected that their redshifts were either gravitational or due to peculiar motion because if the redshift were due to cosmological expansion then QSOs would have to be exceedingly bright for us to see them at the observed magnitudes (their absolute magnitudes would be in the range of -23 to -30 compared to the integrated magnitude of galaxy M87 which is only -22). In the case of gravitational redshift the emitting source is located in a deep gravitational well with the amount of redshift depending on how far into the well the source is. But with gravitational redshift we expect the emission lines to be broadened since

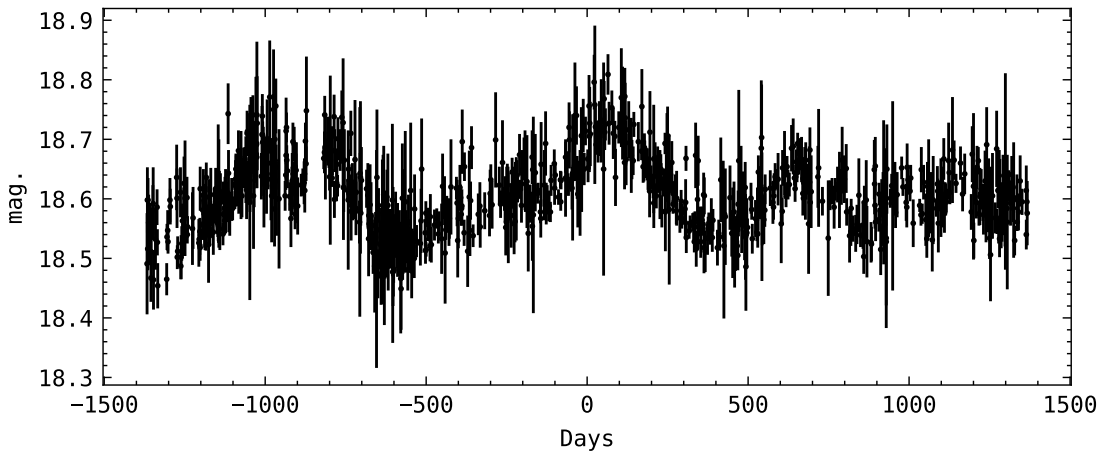

Figure 2.1: The light curve of QSO 9.5484.258 measured by the MACHO project. Due to the expansion of the universe relativistic time dilation occurs causing the observed variations to be longer by a factor of $(1+z)^{-1}$. For this QSO, $z = 2.32$ making the actual variation timescales more than three times shorter than is shown.

not all emitting regions will be at the same gravitational potential therefore giving slightly different redshifts. Broad emission lines can be observed in some QSO emissions but they do not comprise the bulk of the observed redshift so gravitational redshift cannot be the explanation. For peculiar redshift the prevailing idea was that QSOs may be a normal astronomical object such as a star that has been ejected at high velocity from a host galaxy. In this way the object can be close (i.e. lower luminosity) but with a highly shifted spectrum due to its motion. But the continued absence of any highly blueshifted QSOs rules out peculiar redshift based on the Copernican Principle. It was eventually shown in [103] that some QSOs were gravitationaly bound in galaxy clusters of equal redshifts; thus, if the redshifts of the galaxies were cosmological in origin then so too must the redshifts of QSOs.

The variability of QSOs however is something we still know very little about. In fact, many features of QSOs are poorly understood. So like the discussion on

SNIa, I will proceed with out best working model.

As we understand it today, QSOs are a subclass of active galactic nuclei (AGN). AGNs are thought to be galaxies still in the youth of their formation where the central super massive black hole (SMBH, thought to be at the center of nearly all galaxies) is still accreting large volumes of matter via an accretion disk. We believe our own Milky Way galaxy is even expected to have had an AGN phase a long time ago before our SMBH, Sgr A*, used up most of its accreting material and went dormant.

The AGN classification covers a wide and complicated array of astronomical objects from Seyfert galaxies to blazars (see figure 2.2). When a very energetic AGN is viewed at an angle not dominated by the jet a QSO is observed. The radiation from a QSO comes primarily from the super-heating of the accretion disk which emits mostly in the X-ray and UV spectrum. For non-rotating SMBHs the matter-to-radiation conversion in the super-heating of the accretion disk is about eight times more efficient than the *p*-*p* nuclear fusion process found in the Sun, while rapidly rotating SMBHs can reach up to about 45 times more efficient [104] which has earned QSOs the title for the most efficient engine in the known Universe. The aging process of QSOs is still poorly understood so it is unclear how long the birth or death of a QSO takes or what a dimming QSO looks like. This could potentially be an issue when trying to use QSOs as standard candles unlike SNIa. Since SNIa are short lived we are in principle able to observe their full lifetime. QSOs on the other hand have extremely long lifetimes (orders of magnitude longer than the lifetime of any research grant) so it is at the moment not possible to tell where a QSO is in its lifetime. This ambiguity could cause some selection bias since, if we consider all QSOs to have formed around the same time, QSOs at higher redshift will be younger while

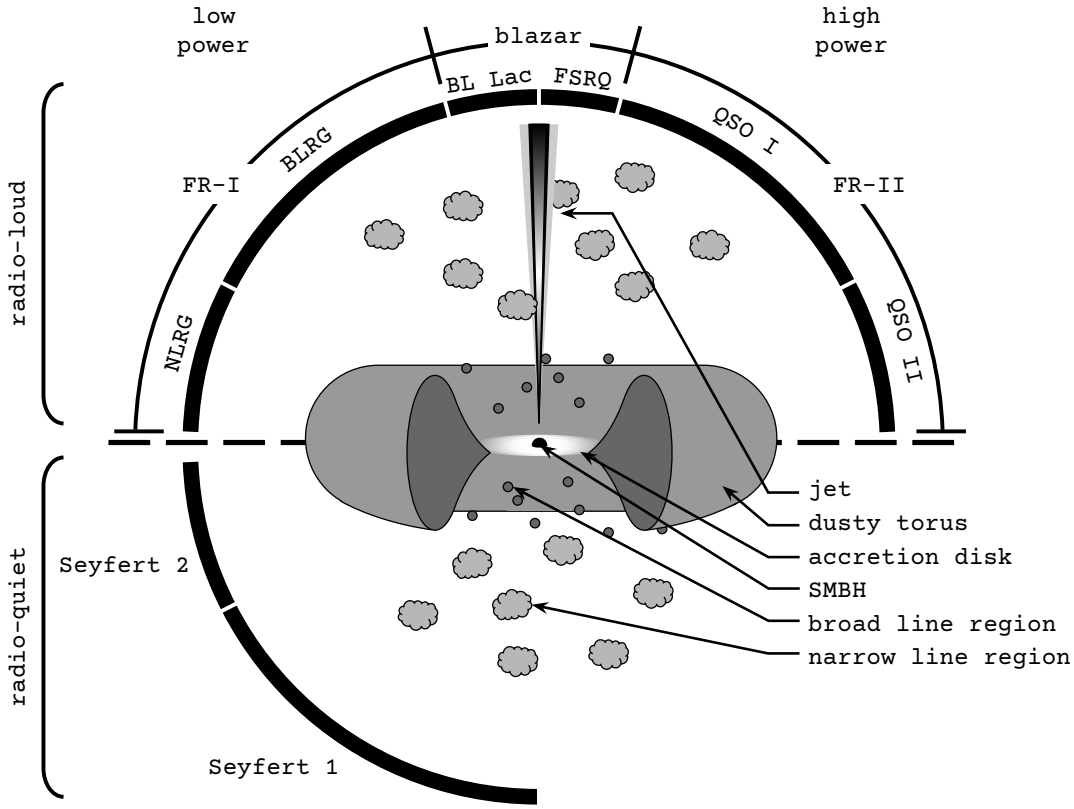

Figure 2.2: A cartoon of the unified picture of AGNs. In reality the division lines are not so clean cut. Previously thought to be distinct, all of these objects listed around the circumference are now understood to be different sublclasses of AGNs. Apparent dividing lines seem to follow energetics, presence of a jet, and viewing angle. Normally the jets are produced in an antipodal set but, for the representation of radio-quiet AGNs which have not been observed with jets, the lower jet has been left off.

lower redshift QSOs will be older and they do not necessarily have to behave the same.

Regardless of how little we understand about QSOs, they would make very useful distance indicators. They have been observed at redshifts ranging from $z \approx 0.04$ (Mrk 231) up to $z \approx 7.6$ (J0313-1806) with a population density peaking around $z \approx 2$ [105]. Their long lifetimes make repeated observations possible and they make up close to a tenth of the galaxies observed by the Sload Digital

Sky Survey (SDSS). For these reasons there have been many attempts at using QSOs as distance indicators through reverberation mapping [106, 107], a nonlinear relation between L_X and L_{UV} [108–112], the virial luminosity from emission line widths [113], metallicity [114], and X-ray variance variability [115]. The method I discuss is one that I discovered in [1] which uses a phenomenological relation between the rate of short timescale variations (i.e. the slope of fluctuations) in QSO light curves and their luminosities. Since the origin of QSO variability remains poorly understood the physical nature of the relation is a mystery; although, a simple motivation may be made by analogy. In general, thermal fluctuations grow with temperature so one would expect the variance in a QSO light curve to have some correlation with its luminosity as observed by [115], but the variance is dominated by the randomness of the fluctuations. But how quickly the accreting fluid can increase and decrease in temperature is only dependent on the characteristics of the fluid and the heat source. Assuming the makeup of the accretion disk is pretty uniform across QSOs then it is reasonable to consider that the slopes of short timescale variations is tied to the luminosity.

2.0.2 Quasar Sample

The analysis outlined later in section 2.0.3 requires high cadence light curves. That is to say, photometric measurements of the QSO must have been made more than once per month in order to optimize our analysis. This requirement constrains our use of available data sets since most prior QSO studies sample much less regularly. However, the high cadence light curves from microlensing projects (MACHO, OGLE, etc.) and strong lensing time delay projects (COSMOGRAIL) can in principle be repurposed for our analysis.

Thanks to the efforts of Geha et. al. in [116] 59 quasars from the MACHO project have been confirmed and made available for public use.[1] Assuming the microlensing events are infrequent enough then one can easily avoid them or subtract them out of the light curves. None of the 59 light curves show obvious signs of microlensing events, but quasar 42.860.123 has a significantly low sampling and will be neglected in this work. The OGLE project on the other hand has observed over 700 quasars (see [117]) – the light curves of which are expected to be in the coming OGLE IV release but are not yet available at the writing of this article.

The multiply lensed quasars from the COSMOGRAIL collaboration have the potential to be highly beneficial to our analysis since their time delays effectively extend a quasar's observation time which gives better statistics to our analysis. Also, the overlapping regions between two matched light curves could reduce the uncertainty in the quasar's intrinsic variations. Having said that, the purposes of the time delay measurements are concerned only with matching the light curves from one quasar at a time and do not require a universal calibration among different quasars. The calibrations are instead done with respect to stable stars within a small viewing angle of each strongly lensed quasar thereby making their apparent magnitudes shifted by some undetermined value unique to each quasar. One could in principle recalibrate these light curves using the calibrations given by the COSMOGRAIL team; however, the additional effect of the lens is not very well understood and can cause an uncertain amount of brightening in the individual images. These effects would require further study before the light curves can be significantly considered towards our purposes.

Focusing now on the 58 remaining quasars from the MACHO project, the

[1] http://www.astro.yale.edu/mgeha/MACHO/

apparent magnitudes are supplied in both the v- and r-bands. We make the usual conversion to absolute magnitudes,

$$M = m - 5(\log d_L - 1) - K(z) \tag{2.1}$$

which is similar to equation 1.29 with the addition of the K-correction, $K(z)$. The K-correction is an approximate correction for the apparent shift of the spectral energy distribution across the narrow band filters used in observations. For example, if the quasar's flux varies over its spectrum as $f \sim \nu^{\delta}$ then two identical quasars at different redshifts (but measured with the same filter) would display different absolute magnitudes. In magnitude form the K-correction goes as

$$K(z) = -2.5(1+\delta)\log(1+z) \tag{2.2}$$

with the canonical spectral index $\delta = -0.5$ being taken (see [118]). For proof of concept d_L has been calculated from the redshift of each quasar using a standard cosmology with $\Omega_m = 0.3$, $\Omega_\Lambda = 0.7$, and $h = 0.7$. This makes our present work model dependent, but using a larger collection of quasars at small redshift or ones with relative distances determined through cross-calibrations with SNIa would allow us to avoid this model dependence in future work.

On average the MACHO quasars are sampled with more regularity in the v-band. We therefore commit our analysis only to the well sampled v-band, but in principle the finding method is independent of wavelength and may very well show less dispersion in another well sampled band. It should also be noted that the MACHO quasars were selected based off of their variability so the below arguments may hold only for highly variable quasars. Quasars from other

surveys may clarify this.

2.0.3 Finding Method & Analysis

Our intention is to simply measure the average absolute slope of the increases and decreases in flux making up the QSO variability. The previous work of [119] had hand selected approximately linear segments spanning ∼90 days in the QSOs' rest frames and made linear fits to each. While this was sufficient for their purposes we require a less subjective analysis and one that can be extended to large data sets. A popular idea would be to train a supervised neural network to select the linear behaviors from noisy signals, but since we are constrained on data we are not yet able to obtain a large enough training set. I have instead constructed a more elementary approach.

Searching for linear trends in noisy and intrinsically variable data is a tricky task. It is likely that two individuals would agree on the general location of a linear segment in a varying data set but not so much on the beginning and end-points of the linear segment. Take figure 2.3 for instance where we represent a light curve segment with a simple sine wave shown in black dots[2]. We want to measure the slope of the rising segment which we have highlighted with a box in the leftmost plot. To measure the slope of this segment one would naturally truncate the beginning and end of the curve until a roughly linear segment is obtained and then fit to a straight line (i.e. look at only a small window around the center of the interested region). If the truncation is not enough, resulting in contributions from data near the turning points of the curve, then the slope is

[2]Keep in mind as we go through these arguments that the actual data will have noise and a less defined pattern such that some very obvious and simple alternative solutions can become quite complicated.

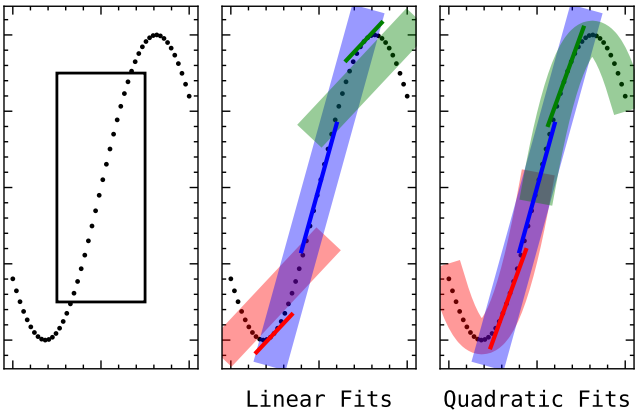

Figure 2.3: Illustration of the finding method using linear (center) and quadratic (right) fits. The intended slope is boxed in the leftmost figure. The thick bands in the right two figures represent fits to subsections of the curve while the lines of the same color are the slopes that are being taken from the fits. The blue line best approximates the intended slope.

skewed off of the expected value (in this case to lower values). See footnote 2 for issues with truncating too much. In order to side step these issues we have segmented the data into subsections. The right two plots of figure 2.3 shows segments spanning half the length of the total curve: the faint red bands encompass the first half of the curve, the faint green bands encompass the last half of the curve, and the faint blue bands cover the middle half of the curve, partially overlapping the previous two halves. Further segmentation of the curve is done with five segments each spanning a third of the curve's full length and again with seven segments each spanning a fourth of the full length and so on until we reach a minimum window length which we set by hand. Figure 2.3 only shows the first iteration of segmentations for clarity.

In the linear fits plot of figure 2.3 the three faint bands are the linear best fits for their corresponding segments while the darker lines of the same color are the slopes of the corresponding fit at the middle point of the segment. For the linear fit method, these two are degenerate in slope values. The blue segment does

pretty good at approximating the slope value we had intended, although it is a little underestimated due to the points at its extremes. The χ^2/DoF of the blue fit would therefore be close to unity. The red and green segments on the other hand significantly underestimate the intended slope but likewise have a poor χ^2/DoF. By taking the most common slope from the weighted population of fits (including fits from smaller segments), with weights determined by the χ^2/DoF values, we are able to obtain a reasonable estimate for the intended slope. Due to the simplicity of our example all slopes will be an underestimated, but the presence of noise in actual light curves allows for overestimations as well.

The quadratic fits plot of figure 2.3 uses quadratic functions to fit the segments of the curve instead of linear functions as one can see from the faint bands. The blue band is identical in both plots as expected but the red and green bands clearly fit their curve segments much better than the linear fits had. If we evaluate the slope of the quadratic fits at the middle point of the individual segments then we will obtain the same result as what the linear fitting method gave but with worse discrimination due to better overall χ^2/DoF values for each fit. So instead we evaluate the slope of the quadratic fit at a point midway between the minimum of the fit and the maximum of the fit, hence the shifts of the red and green lines. This gives an overall better estimate of the slope in the rising (or falling) sections of the curves as we can see from the near alignments of the red, blue, and green lines along the rising section in the curve.

While the use of linear fits has a wide spread of slope values it also has good discriminatory power through its weighting with the goodness-of-fit values. Using quadratic fits can get a narrower spread around the intended slope but is not able to weight the slopes as well due to the overall better goodness-of-fit values of the quadratic function. Both methods are sufficient for the analysis

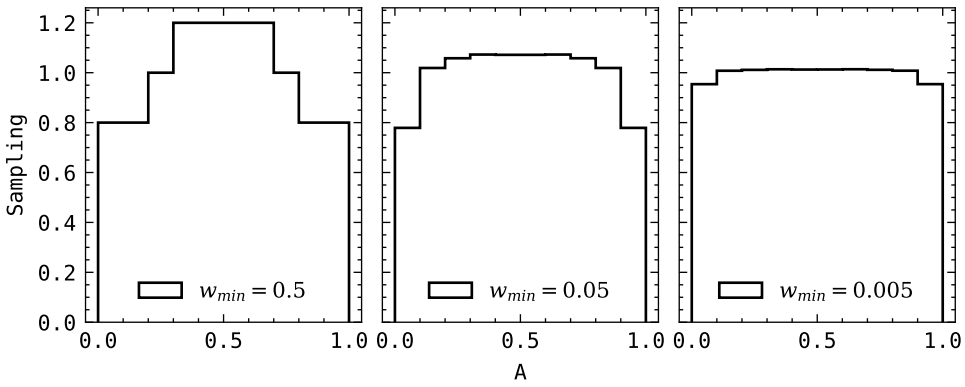

Figure 2.4: We consider an example data set, A, stretching uniformly over the range [0,1]. If we consider a minimum window size of $w_{min} = 0.5$ (left most) then features in the middle of the data set will be given more significance as highlighted by the central peak. But decreasing the w_{min} (middle and right most) spreads the weighting more evenly across the data set.

but in practice the quadratic fitting method performs marginally better. Therefore, in the remaining sections we will assume the use of the quadratic method.

One may note that this method samples the slopes of the inner regions of the curve more than the outer regions (i.e. the blue regions in figure 2.3 overlaps with the inner halves of the red and green regions, effectively weighting them twice as much as the outer regions). This persists as the segmentation goes to smaller window sizes but, as shown in figure 2.4, as long as the length of the curve is much larger than the minimum window size then the effect is negligible.

We define the variational rate, s_F, as the most common slope returned by the above method where the subscript denotes whether the curve is from an absolute light curve, s_F, or an apparent light curve, s_f. The method allows for an almost completely objective determination of s_F with dependence on only two subjective parameters. The first of these parameters is the choice of the minimum window size, w_{min}, the segmentation process will go down to. Tak-

ing w_{min} too large makes us insensitive to short timescale variations in addition to the unequal sampling shown in figure 2.4. In an ideal case, the smaller the w_{min} value the better since all timescales would be sampled evenly. However, the smallest timescales will be dominated by noise which will skew our results, usually towards higher slope values. In order to curb this issue we have made visual inspections of the multiply lensed quasars from the COSMOGRAIL collaboration. The overlapping regions of their matched light curves show that variations occurring at timescales greater than about 40 days are nearly identical in both images. Since the images have a time-delay between them, the matched variations correspond to observations taken at two different times. Therefore, the variations at timescales greater than 40 days are unlikely to be due to local noise. With this we take $w_{min} = 40$days in the quasar's rest frame. This argument does not necessarily rule out local noise from the $>$40 day long variations in the MACHO light curves used here nor does it rule out non-noise dominated variations at shorter time scales – it just gives a standard to improve from. The second parameter we must set by hand is the lower cutoff for the sampling frequency (i.e. the lowest average density of data points we are willing to consider in a light curve segment). For accurate fits at all timescales we require the sampling frequency to be at least greater than $2/w_{min}$. Little dependence is seen in varying this value within reason though, but applying this cutoff avoids large unsampled gaps (usually between observing seasons) from skewing s_F towards lower values.

Figure 2.5 shows the light curve of quasar 9.5484.258 with the finding method applied to it. The slopes from the quadratic fits method are superimposed over the light curve showing a dense network of lines which map out the general behavior of the light curve. Figure 2.6 shows the corresponding weighted pop-

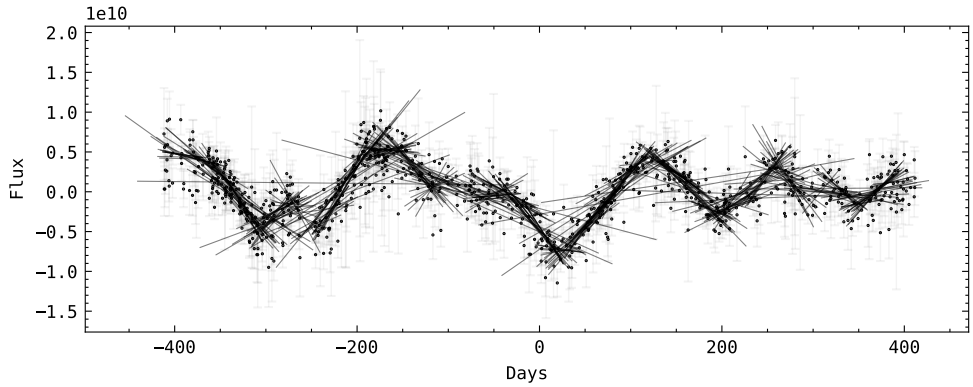

Figure 2.5: The fitted light curve of quasar 9.5484.258 from the MACHO project (centered at the origin). The slopes (measured using the quadratic fits method) are shown overlaying the sections of the light curve they correspond to. The fits range from half of the observation period down to ≈ 40 days. The error bars on the data is suppressed for clarity.

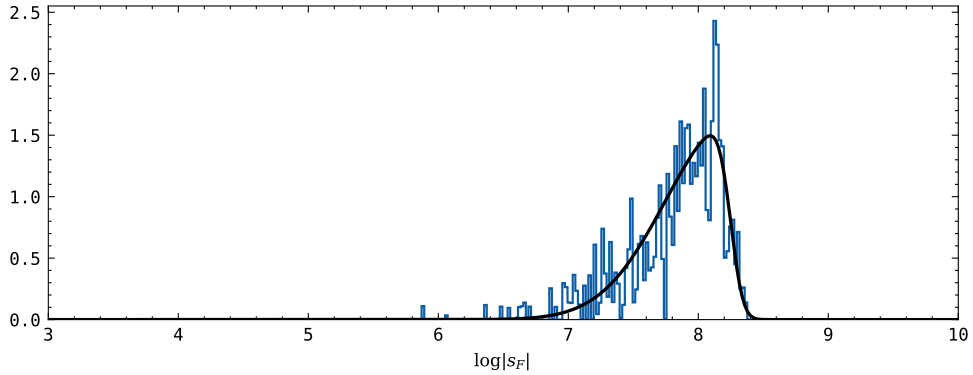

Figure 2.6: The population of $\log|s_F|$ for quasar 9.5484.258 weighted by the χ^2/DoF of the corresponding fits. For this particular quasar, the expected variational rate would be $\log|s_F| = 8.10$.

ulation of measured slopes which for 9.5484.258 has $\log|s_F| = 8.10$ or $|s_F| = 1.26 \times 10^8$ units/day as determined by the mode of a skewed normal fit to the histogram (figure 2.7 shows the weighted population of 16 other randomly selected quasars for reference).

Applying this analysis to each of the quasars individually we have found (see figure 2.8) that the variational rate has a nonlinear relation with the mean

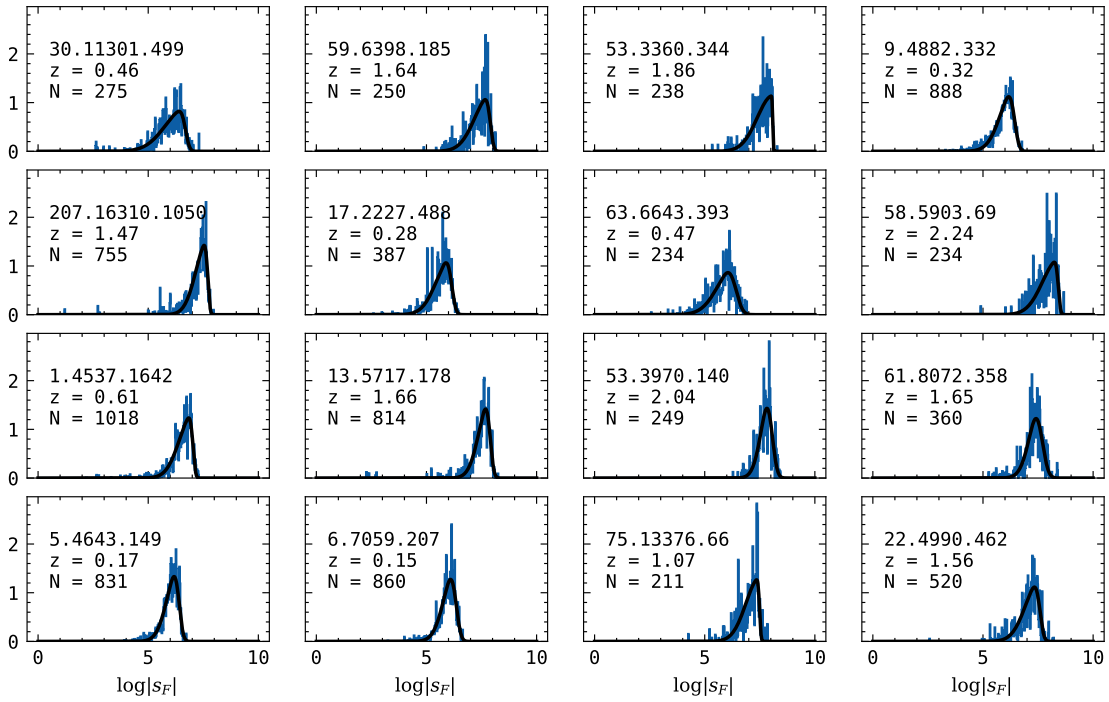

Figure 2.7: A larger display of the weighted s_F populations in the MACHO data set. The MACHO ID, redshift, and number of observations are given for each quasar.

absolute magnitude,

$$\log|s_F| - \log(1+z) = \alpha\langle M\rangle + \beta \tag{2.3}$$

where the $\log(1+z)$ term is introduced to cancel out the z dependence of the time derivatives in

$$s_F = \frac{dF}{dt_{qso}} = (1+z)\frac{dF}{dt_{obs}}.$$

Using a least squared fit gives $\alpha = -0.2920 \pm 0.0101$ and $\beta = -0.36 \pm 0.25$. With no selection criteria made except for the two parameters already discussed we obtain a dispersion of 0.16dex without any significant dependence on z as can be seen in figure 2.9. If we make a very rough cut by considering only those

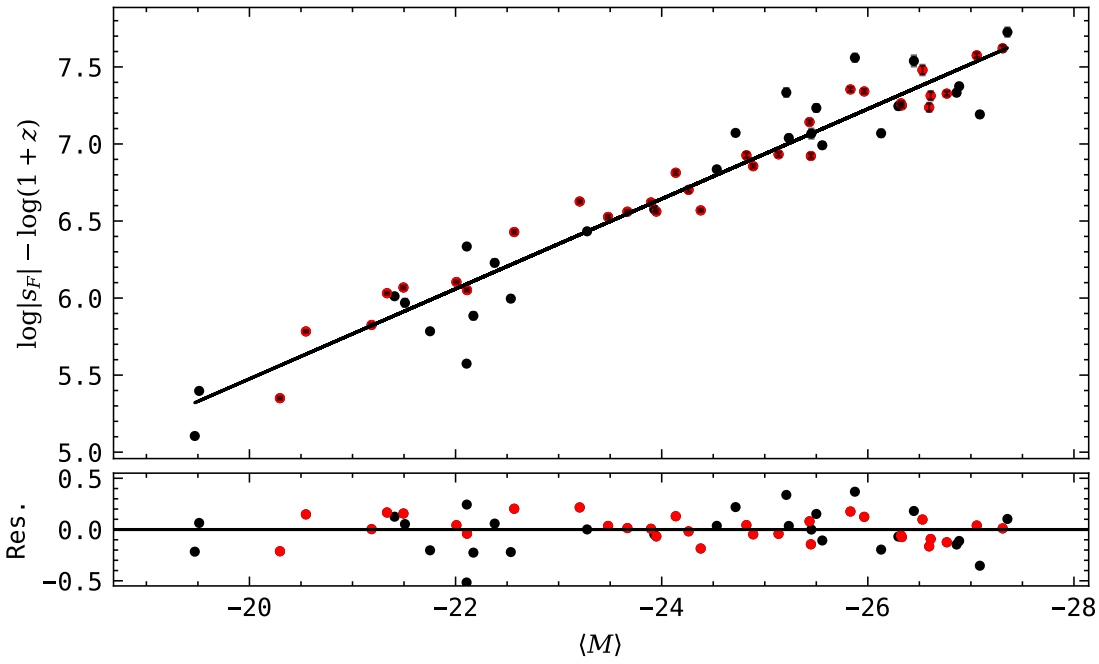

Figure 2.8: The v-band variational rate against the mean absolute magnitude in the quasars' rest frames shows a strong correlation with 0.16dex dispersion. Red points correspond to quasars with high sampling (N≥500). Error bars are barely visible and are determined by the uncertainty in the peak position of the quasar's fitted histogram.

light curves with ≥500 observations over the ∼3000 day observational period then we can reduce our dispersion down to 0.11dex though we also reduce the number of light curves to 31. Those 31 quasars are highlighted in red in relevant figures. We note however the bruteness of this cut since it does not take into account the uniformity of the ≥500 observations. Furthermore, the model assumption used to calculate the MACHO quasars' d_L values may contribute towards a higher dispersion. It is possible that relieving the model dependence could reduce the dispersion.

For clarity, the dispersion estimates discussed here have been calculated us-

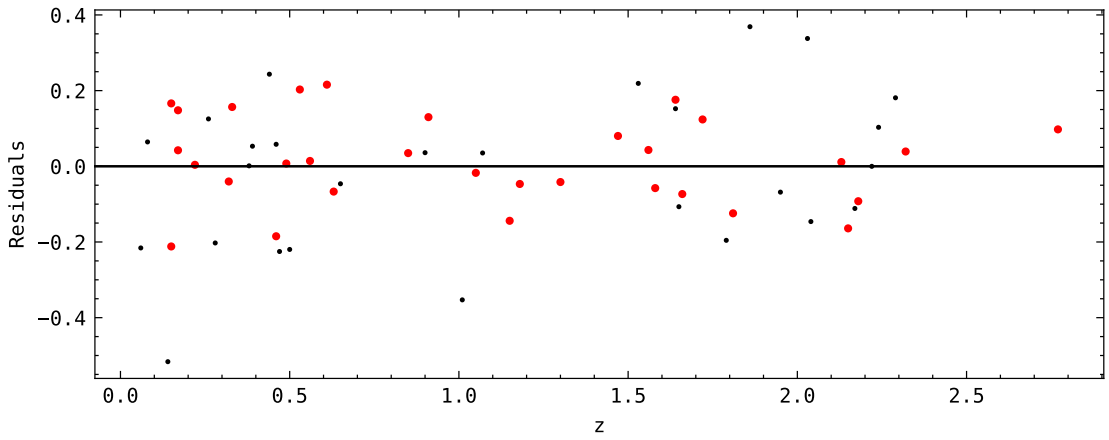

Figure 2.9: Residuals of the s_F vs. $\langle M \rangle$ show no clear dependence on redshift.

ing (2.4) where fit$\big(\langle M \rangle\big)$ refers to the right-hand side of (2.3).

$$d = \sqrt{\frac{\sum_i^N \Big(\text{fit}\big(\langle M \rangle_i\big) - \big(\log|s_F|_i - \log(1+z_i)\big)\Big)^2}{N-1}}. \tag{2.4}$$

2.0.4 Luminosity Distance

We now derive the luminosity distance from our fitted s_F vs. $\langle M \rangle$ relation, (2.3). The variational rate of the absolute light curve, s_F, can be related to that in the apparent light curve, $s_f = \frac{df}{dt_{obs}}$, through

$$\log|s_F| = \log|s_f| + \log(1+z) + 2(\log d_L - 1) + \tfrac{2}{5}K(z). \tag{2.5}$$

Using (2.1) and (2.5) in (2.3) allows one to obtain

$$\log d_L = (2+5\alpha)^{-1}[\alpha\langle m \rangle + \beta - \log|s_f|] - \tfrac{1}{5}K(z) + 1 \tag{2.6}$$

showing that in practice one can calculate the luminosity distance from the apparent light curves.

In a demonstration of the work to come we have constructed a Hubble diagram for a sample of quasars from the Sloan Digital Sky Survey (SDSS) assembled by MacLeod et. al., [120][3]. That is to say, we will now calculate $\langle m \rangle$ and s_f from a different set of quasar light curves and predict a cosmology from them. The full sample contains 9258 light curves all of which have a sampling frequency far below the minimum requirements we have discussed in previous sections. In addition, the SDSS observations were made in the u-, g-, r-, i-, and z-bands as opposed to the v-band which we have used to calibrate the s_F vs. $\langle M \rangle$ relation. But, in order to show what future work is needed, we have imposed a rough cut of >100 observations over the survey's ∼10 year observing period. This reduces the number of light curves to 304 but allows the fitting algorithms to be applied without technical issues. Figure 2.10 show the fitted apparent light curve and resulting weighted s_f population of the best sampled quasar of the SDSS dataset. Notice the poor sampling of the quasar compared to the MACHO quasars and also the difference in time scales.

Figure 2.11 shows the Hubble diagram corresponding to the i-band SDSS sample with the distance modulus, DM, defined as

$$DM = 5(\log d_L - 1) \tag{2.7}$$

and errors given as

$$d(DM) = \frac{5\sqrt{(2\langle m \rangle - \beta + \log|s_f|)^2 d\alpha^2 + (2+5\alpha)^2 (d\beta^2 + d(\log|s_f|)^2)}}{(2+5\alpha)^2}. \tag{2.8}$$

The uncertainty in $\langle m \rangle$ is neglected here. The black points correspond to the

[3]We have only made use of the southern sample which can be found here: http://faculty.washington.edu/ivezic/macleod/qso_dr7/index.html

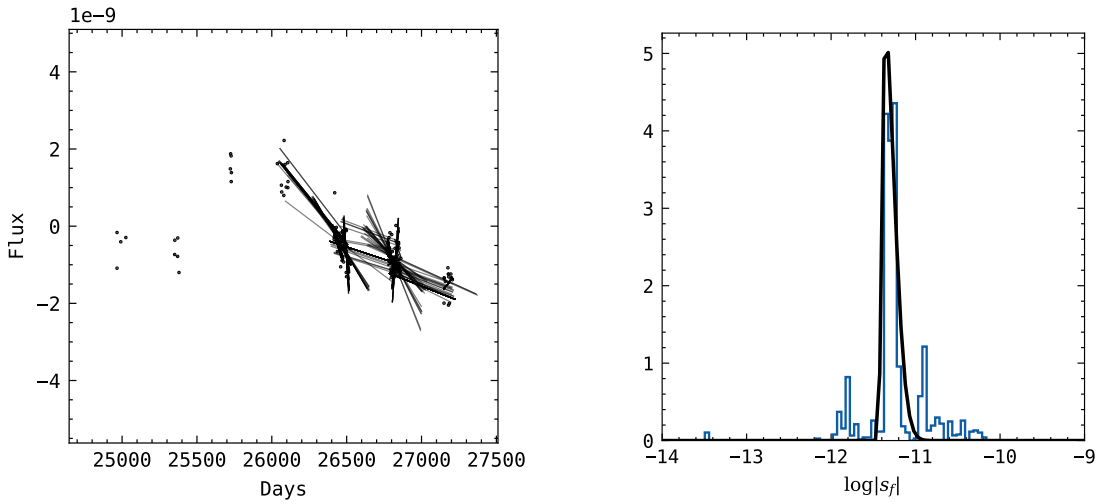

Figure 2.10: *Left*: The fitted light curve of quasar 1365809 from the SDSS dataset (the best sampled quasar in the set). *Right*: The corresponding weighted s_f population. To ensure the same dynamics are being compared for all quasars in the observer's frame, the minimum window size of the finding method is taken to be $(1+z)\times$40days.

individual quasars which have been binned by redshift shown in red. We note that these distance moduli are calculated without any assumptions on the cosmology with the exception of the model dependencies used to calibrate α and β. It should also be noted that even though the SDSS light curves are significantly under sampled, the individual light curves typically have short, densely sampled observing periods which are sufficient for our finding method. The short observing periods provide us with a rough estimate of the average slope but lack the statistics that longer observations can produce, hence the large dispersion. Sufficiently sampled light curves should give the same overall behavior with less dispersion.

We wish to highlight that even with the exceedingly poor sampling of the SDSS dataset the general behavior still follows the ΛCDM model with good accuracy. This should not be misinterpreted as a demonstration that ΛCDM holds

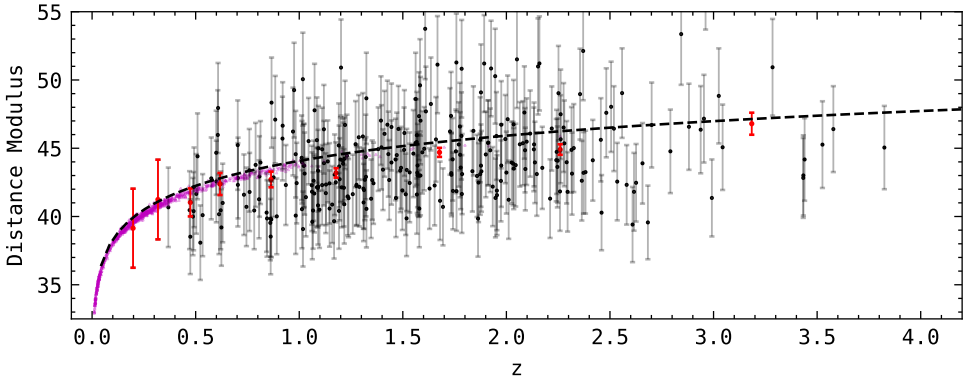

Figure 2.11: Hubble diagram of the 304 quasars from the SDSS sample (black points) and their binned values (red points, binned by redshift). SNIa from the Pantheon survey [88] (magenta points), have been added for comparison. The black dashed line corresponds to the ΛCDM distance modulus with *Planck* 2018 [11] best fit parameters. The quasars closely follow the ΛCDM model, accurately demonstrating our current model dependence.

up to $z \approx 4$ nor should it be taken as a disagreement with [109–112]. Since the fitting parameters α and β were calibrated using a ΛCDM cosmology, our agreement with ΛCDM only shows the effectiveness of our analysis. Assuming a different model for the MACHO calibration would have resulted in different fitting parameters and the SDSS Hubble diagram following the distance modulus determined by that model. Given a large enough sample of light curves, it should be possible to use the low redshift quasars in the sample to calibrate α and β with minimal model dependence while using the high redshift quasars for cosmological parameter estimations. But obtaining relative distances to well sampled quasars through their proximity to SNIa would be the ideal calibration of α and β. So far no such relative distances have been noted.

We would like to further note that the binned SDSS Hubble diagram of Fig. 8 does not match exactly with the *Planck* 2018 Pl18 best fit values (dashed line) but instead falls short at high redshift values ($z > 0.75$). This difference may likely be due to the poor sampling of the SDSS quasars, choice of binning, or,

more interestingly, differences in the redshift distributions between the MACHO sample used for calibration and the SDSS sample. The MACHO sample has an effective redshift of $z_{eff} = 1.1$ while the SDSS sample is slightly higher at $z_{eff} = 1.6$. This may be an indication of disagreement between Hubble diagrams at high-redshift and a flat ΛCDM cosmology. We will however consider this possibility in future work.

2.0.5 Damped Random Walk

We now comment on our agreements with findings made using synthetic quasar light curves. Damped random walks (DRWs), or biased random walks, have proven effective towards modeling quasar light curves in the optical band (see [121, 122]). duck DRWs perform a random walk over short time scales, $\Delta t \ll \tau$, but have a restoring term such that the walk leads back to the same place over larger time scales, $\Delta t \sim \tau$. The process, excluding the overall magnitude, takes just two parameters: τ, the relaxation time which controls the strength of the restoring term, and SF_∞, the structure function at infinite time scales (not to be confused with s_F) which controls the variability at times $\Delta t \ll \tau$. A DRW can be generated as a solution to the differential equation

$$\tau dF(t) = -F(t)dt + SF_\infty \epsilon(t)\sqrt{2\tau dt} + \langle F \rangle dt \tag{2.9}$$

where $F(t)$ is the flux in our example and $\epsilon(t)$ is a white noise function with zero mean and unit variance. We instead resort to the Python module astroML (ref. [123]) which contains a DRW generating function built in.

We have generated 100 DRW light curves spanning an observation period of three years each. Applying the same analysis discussed in section 2.0.3 we

find for the s_F vs. $\langle M \rangle$ relation in the DRW light curves an $\alpha_{DRW} \approx -\frac{2}{5}$ with negligible deviations as we vary τ and SF_∞. No constant values of τ and SF_∞ were found that would allow $\alpha_{DRW} \approx -0.3$ as one would hope in order to have agreement with the MACHO light curves.

However, in studying the r- and b-band light curves of 100 actual quasars (55 of which were from the MACHO survey) in the context of DRWs the authors of [121, 122] have found relations between the mean luminosity and separately SF_∞ and τ. Other relations were also discussed but are not of interest here. The authors of [122] have parameterized these relations as

$$\log SF_\infty = A + C(M_i + 23) \tag{2.10}$$

and

$$\log \tau = A' + C'(M_i + 23) \tag{2.11}$$

where M_i is the i-band mean magnitude and $\{A, C, A', C'\}$ are best fit parameters given in Table 1 of [122]. Logarithmic dependencies on wavelength and black hole mass have been excluded for the present work. Now generating 1000 DRW light curves, using (2.10) and (2.11) our analysis finds an s_F vs. $\langle M \rangle$ relation with $\alpha_{DRW} = -0.2813 \pm 0.0012$ and a dispersion of 0.095dex (see figure 2.12). Assuming deviations due to varying band usage to be small, it would seem as though our $\alpha = -0.2929 \pm 0.0098$ from the MACHO light curves is in agreement with the findings of [122].

Furthermore, in section 2.0.4 the luminosity distance was derived in terms of our fitting parameters from which we see that an $\alpha = -\frac{2}{5}$ value would not allow the determination of d_L from the apparent light curves. It would then seem that

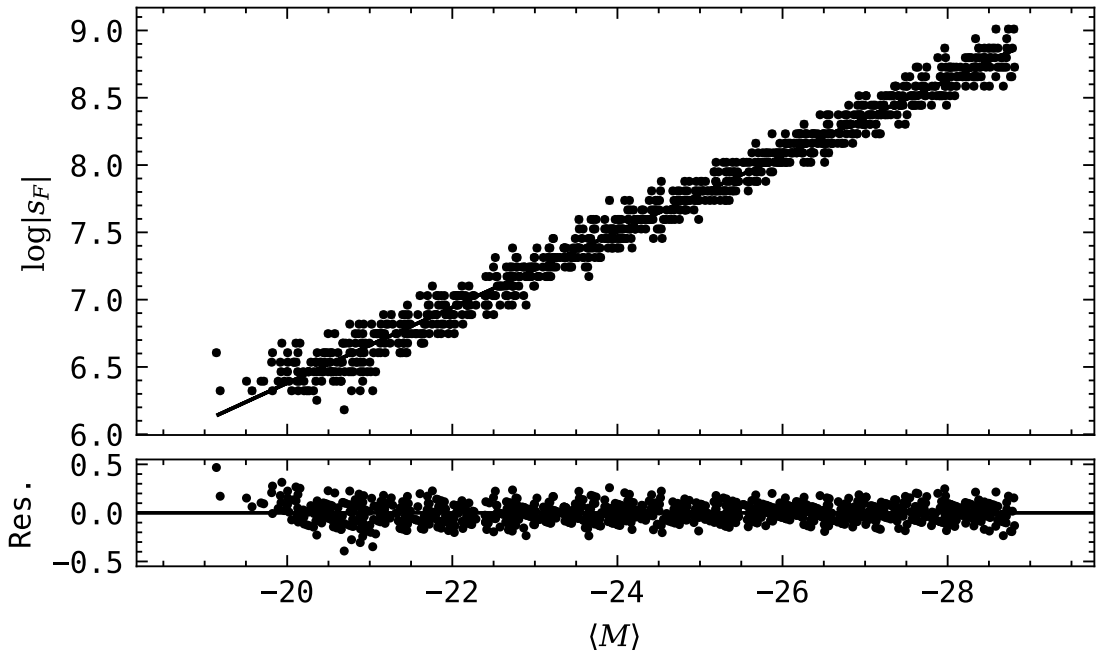

Figure 2.12: Same as figure 2.8 but over the 1000 synthetic DRW light curves. For simplicity the synthetic quasars were assumed at a redshift of $z = 0$.

the unexpected relations between (SF_∞, τ) and mean luminosity that enables us to determine the luminosity distance.

One point of interest is that the use of the $SF_\infty(M_i)$ and $\tau(M_i)$ relations causes a slightly higher dispersion for low luminosity quasars (below $M > -20$ in the simulations of figure 2.12). It is unclear if this is a feature of quasars or an artifact of the fitted $SF_\infty(M_i)$ and $\tau(M_i)$ relations as the range of luminosities it is outside of that probed by the MACHO sample.

2.0.6 Summary

We have shown that the variability in the apparent light curves of quasars can be used to determine their luminosity distance making it possible to join quasars to the cosmic distance ladder. This is through an observed dispersion of 0.15dex

in the s_F vs. $\langle M \rangle$ relation from quasars spanning a large range of luminosities. With further studies and cleaner data sets we may be able to reduce the dispersion even further. That being said, if the modeling of quasar light curves through DRWs is effective for all intents and purposes, the dispersion of 0.095dex in figure 2.12 may be a lower cutoff to the accuracy of this method.

Figure 2.8 and the resulting fit, (2.3), show that the variations are systematically more rapid for brighter quasars in agreement with [121, 122]. This would seem to disfavor the starburst model as the cause of the variations. The starburst model, in assuming the variations are due to supernovae in the environment of the quasar, would not naturally explain the increasing variational rate of brighter quasars, but perhaps the accretion instability model could still work. As discussed in [121], the short time scale variations in the optical bands are likely due to local irregularities in the accretion disk from turbulence and other effects.

The form of (2.6) is similar to equation (7) in [112]. We mention this only to clarify the advantages and limitations of our method. Since $\log d_L$ goes as $(2 + 5\alpha)^{-1}$ or $0.5(1 - \gamma)^{-1}$ in [112] then for our method to be on par with previous works we would need a dispersion below the $\frac{(2+5\alpha)}{2(1-\gamma)}$0.2dex level. That is to say, taking $\alpha \approx -0.3$ and $\gamma \approx 0.6$, we should have a dispersion of 0.13dex or lower if we wish to improve the use of quasars as standard candles. Using all 58 MACHO quasars does not quite satisfy this with a dispersion of 0.15dex. Just using the better sampled quasars (N$\geq$500) does however with a dispersion of 0.11dex The obvious drawback to our method in comparison to that in [112] is the observational effort required to produce the needed light curves. But there have been many such observations already made by the microlensing and strong lensing communities that could relieve this issue. A dedicated survey

would however be ideal in reducing the dispersion.

At this point we have shown that our method can be applied with great success. In follow up efforts we will extend the analyses to a larger number of low-z quasar light curves in order to ensure the statistical relevance of the s_F vs. $\langle M \rangle$ relation and to relieve our current model dependence.

2.0.7 Precautions for high redshift probes

The redshift range $2 \lesssim z \lesssim 1100$ is the current playground for observational constraints on cosmology. However we must be cautious as we add probes in this range due to subtle biases in the flat ΛCDM model that if left unchecked will likely cause spurious deviations from both baseline high z and low z observations.

The analytic argument is fairly straightforward. Given that the Hubble parameter in the late universe can be written as

$$H(z) \approx H_{100}\sqrt{\omega_\Lambda + \omega_m(1+z)^3}, \tag{2.12}$$

where $\omega_i \equiv \Omega_i h^2$, we can see that at very low redshifts $H(z)$ is sensitive to both ω_Λ and ω_m, but at higher redshifts the sensitivity to ω_Λ quickly drops off. Therefore, any dispersion in higher redshift probes effectively washes out any inference of dark energy at lower redshifts. And with the added flatness constraint from *Planck* 2018 [11] intertwining ω_Λ and ω_m through

$$\omega_\Lambda = h^2 - \omega_m \tag{2.13}$$

the insensitivity to ω_Λ at high redshift bleeds into the predictions of Ω_{m0} and h

through non-Gaussian tails which favor higher values of Ω_{m0} and lower values of h.

To illustrate this more clearly let us consider the $H(z)$ error forecasts, σ_{Hs}/Hs, provided by the Dark Energy Spectroscopic Instrument (DESI) [124]. In figure 2.13 we have projected the forecasts onto a flat ΛCDM background with *Planck* 2018 [11] best fit parameters. The projections are used to construct 10^5 mock samples each with dispersions set by the forecasted errors in the relevant redshift ranges. Breaking each mock sample up into redshift bins, we are able to see some particularly troublesome effects. Using a maximum likelihood fitting algorithm, the fitted ω_Λ values in each redshift bin (left of figure 2.13) have an approximately normal distribution around their central value as one would expect (the tight constraints from [11] make the spread in ω_m negligible). Likewise, we see a normal distribution around the true values for Ω_{m0} and h when the full redshift range is taken into account. But while the low redshift bins remain sensitive to the true values, non-Gaussian tails form in the higher redshift bins. By reducing the forecasted errors (i.e. the dispersion in the fitted samples) the formation of non-Gaussian tails can be pushed to higher redshift bins.

The formation of the non-Gaussian tails can be easily understood through error propagation. A converged maximum likelihood fitting method will obtain approximately normal distributions for the coefficients in the fitting function much like what is seen for ω_Λ in figure 2.14. However, the spreads in ω_Λ and ω_m, which we represent as $\mathrm{d}\omega_\Lambda$ and $\mathrm{d}\omega_m$, respectively, is translated into $\mathrm{d}\Omega_{m0}$ and $\mathrm{d}h$ through the relations

$$\mathrm{d}h = \frac{\mathrm{d}\omega_\Lambda}{2\sqrt{\omega_\Lambda + \omega_m}} \tag{2.14}$$

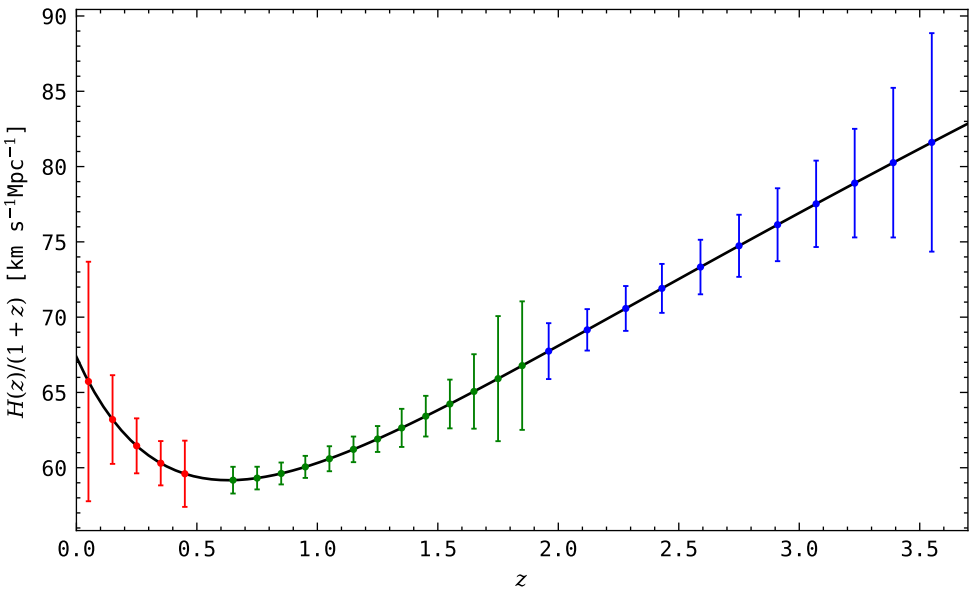

Figure 2.13: Projected uncertainties from the DESI Bright Galaxy Survey (red), DESI (green), and Ly-α forest quasar surveys (blue). The underlying model parameters assume the fiducial values $\Omega_{m0} = 0.3153$, $\Omega_\Lambda = 0.6847$, and $h = 0.6736$.

$$d\Omega_{m0} = -\frac{d\omega_\Lambda}{\omega_\Lambda + \omega_m} + \frac{\omega_\Lambda(d\omega_\Lambda + d\omega_m)}{(\omega_\Lambda + \omega_m)^2} \approx -\frac{\omega_m\, d\omega_\Lambda}{(\omega_\Lambda + \omega_m)^2} \tag{2.15}$$

where in the last line we use the fact that the spread in ω_m is negligible due to the [11] constraints. Clearly, if both ω_Λ and ω_m are Gaussian then h and Ω_{m0} are non-Gaussian with the non-Gaussianities in Ω_{m0} growing faster than in h. We demonstrate this in figure 2.15 where we have assumed Gaussian distributions for both ω_Λ and ω_m with equal spread (solid) and with ω_Λ having a four times larger spread (dashed). Therefore, an increase in $d\omega_\Lambda$, which is expected as we look at higher redshift probes with less sensitivity to the dark energy epoch, generally produces non-Gaussian distributions in (h,Ω_{m0}) in a flat ΛCDM model.

The presence of these non-Gaussian tails will pull the best fit Ω_{m0} (h) to

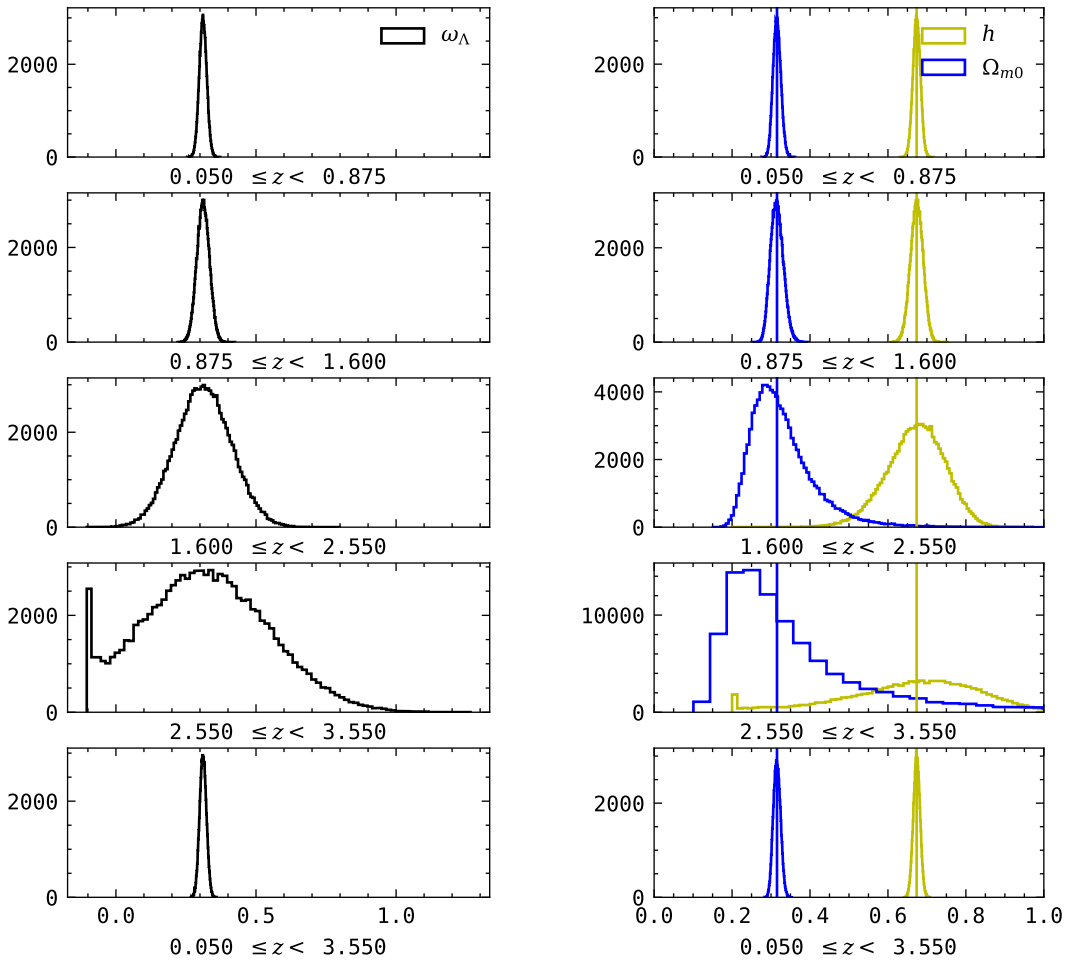

Figure 2.14: *Left*: Distribution of fitted ω_Λ values from the binned mock DESI samples. Note that the ω_Λ values are approximately normally distributed for all redshift bins. The leftward pileup in the [2.550,3.550) bin is an artifact due to the spread growing larger than the allowed parameter ranges: $h \in [0.2, 1.2]$ and $\Omega_{m0} \in [0, 5]$. *Right*: Corresponding distributions in (h,Ω_{m0}) with vertical lines designating the true values. Clearly, the full redshift range (bottom) is able to accurately capture the true values along with the low redshift bins ($z < 1.6$). However, non-Gaussian tales form in the higher redshift bins.

higher (lower) values than is the true value. These effects have recently been observed in the Pantheon+ analysis (see figure 16 in [100]) and also in cosmic chronometers and BAO [3]. Thus, in going forward with dispersive high redshift probes it is important that we take this into account when making cosmo-

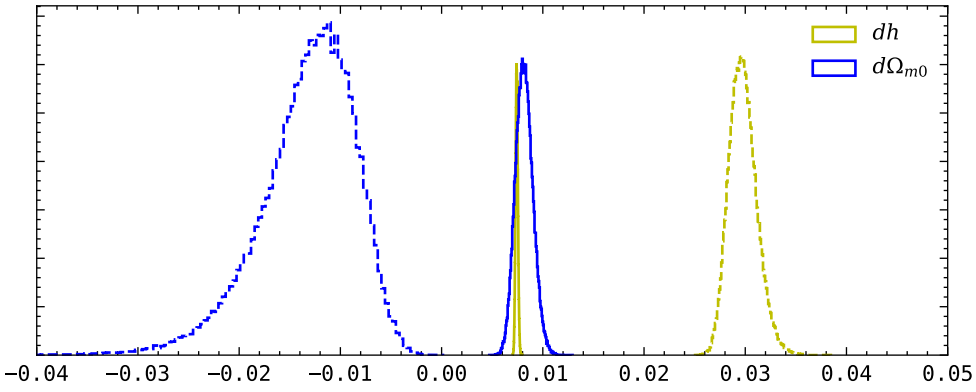

Figure 2.15: *Solid*: Spreads in h and Ω_{m0} assuming Gaussian distributions in ω_Λ and ω_m with a fiducial 0.01 variance. *Dashed*: Similarly but with ω_Λ now having 0.04 variance – a trend we would expect when moving towards higher redshift probes.

logical claims since an error like this would cause an apparent reduction in the Hubble tension. We can avoid dominating non-Gaussian tails in probes with sufficiently low dispersion (on par if not lower than the dispersion found in SNIa) or in probes that can be connected back to the dark energy epoch like what is typically done with standardizable candles and the cosmic distance ladder.

Chapter 3

Modified recombination and the Hubble tension

This chapter follows a mechanism I proposed to naturally source a modified recombination as a means of solving the Hubble tension [4].

3.1 Current state of the Hubble tension

The tension in the measured values of H_0 between early and late time observations is now at 5σ with the latest analysis by the SH0ES team [28]. A great number of attempts have been made towards solving the tension and bringing the two families of observations into agreement.

Systematic errors should of course be everyone's initial suspect for the cause of the tension. Focusing on the *Planck* 2018 [11] and the SH0ES 2021 [28] results there are some hints towards systematic errors. The strongest hint in *Planck* is the $A_L > 1$ anomaly. A_L is a phenomenological parameter used to rescale the lensing amplitude in the CMB power spectrum to match theory with observa-

tion. But with the cosmological parameters determined in a model, the lensing amplitude can be very accurately determined [125]; so one would expect if both data and the model are sufficient then no rescaling would be necessary, corresponding to $A_L = 1$. *Planck* however requires

$$A_L = 1.243 \pm 0.096 \qquad \text{(68\% CL, TT+lowE)} \tag{3.1}$$

$$A_L = 1.180 \pm 0.065 \qquad \text{(68\% CL, TT,TE,EE+lowE),} \tag{3.2}$$

over 2.5σ deviation from $A_L = 1$. In order to explain an $A_L > 1$ we would need to invoke either modified gravity [126], a closed universe [127], or a running in the spectral index [128] all of which are either in strong disagreement with other observations or would require an overhaul in the standard ΛCDM model. More room for systematic errors can be found in the cosmic distance ladder of SH0ES and related works. The most obvious area of concern is in the anchoring of the local Cepheids, which if incorrect can shift the expected H_0 value obtained by SNe by a significant amount. However, independent calibrations have been performed with TRGBs and MIRAS as SNe anchors with similar results; thus reducing the likelihood that systematics in the Cepheid calibration is to blame. Additional systematic errors may lay in our very phenomenological understanding of SNe. [129–131] have discussed differences in the light curves of low and high z SNe, but [132] has shown that taking these effects into account contributes an additional H_0 uncertainty of 0.14km s^{-1} Mpc^{-1} which does not make up a significant contribution to the tension. Many other cross calibrations have been performed (see figure 1.2) and all within reasonable agreement with the SH0ES results making systematics in the cosmic distance ladder either increasingly unlikely or increasingly subtle.

In the absence of sufficient systematic errors there have been many attempts at expanding the theoretical models to explain the tension. Some attempts are minor deviations from ΛCDM such as early dark energy (EDE) models which allow dark energy to make up a significant fraction of the energy density in the early Universe. Other attempts like modified gravity models consider more fundamental changes to cosmology. The review papers [29, 86] outline a great number of the leading attempts at solving the Hubble tension, but we focus on a particularly promising one which uses a dynamic electron mass, m_e, to modify the recombination history.

3.2 Why modify recombination?

The *Planck* 2018 team [11] has very accurately measured the angular scale of the first peak in the CMB power spectrum to be

$$100\theta_* = 1.04097 \pm 0.00046 \qquad \text{(68\% CL, TT+lowE)} \tag{3.3}$$

$$100\theta_* = 1.04109 \pm 0.00030 \qquad \text{(68\% CL, TT,TE,EE+lowE).} \tag{3.4}$$

Since this is just an angle on the sky there is no model dependence in this value. We can however calculate the expected θ_* from a model given that

$$\theta_* = \frac{r_*}{(1+z_*)D_A(z_*)} = \frac{\int_0^{z_*} c_s(1+z)^{-1}H^{-1}dz}{(1+z_*)\int_0^{z_*} H^{-1}dz} \tag{3.5}$$

where r_* is the radius of the comoving sound horizon at recombination, $D_A(z_*)$ is the angular diameter distance to recombination taken to be in flat space, and

the acoustic sound horizon at recombination is given by

$$c_s^{-1} = \sqrt{3 + \frac{9\omega_b}{4\omega_\gamma}(1+z_*)} \tag{3.6}$$

where $\omega_\gamma \equiv \Omega_\gamma h^2$ (for radiation), $\omega_b \equiv \Omega_b h^2$ (for baryonic matter), and, soon to be introduced, $\omega_m \equiv \Omega_m h^2$ (for baryonic + cold dark matter, Ω_c). If one now wishes to allow for an increase in a cosmological parameter such as $h \equiv \frac{H_0}{100km/s/Mpc}$ then the rule of the game is to mirror the increase with a change in other parameters such that r_* and $(1+z_*)D_A(z_*)$ remain unchanged, or at least their ratio remains unchanged. For our purposes, we can get a better grasp of the problem after evaluating the integrals in (3.5). Parsing out the important parts of the integral we find that we can keep the numerator and denominator of (3.5) separately unchanged if we keep the two values

$$\frac{4\omega_\gamma}{3\omega_b}(1+z_*), \qquad \frac{(1+z_*)}{\omega_m}\sqrt{\frac{\omega_m}{(1+z_*)} + \omega_\gamma} \tag{3.7}$$

unchanged. Given that $\omega_m = \omega_c + \omega_b$ we assume any changes in ω_b are shared with ω_m, i.e. $\Delta\omega_m = \Delta\omega_b$. It is clear then that both terms remain unaffected if $\Delta\omega_m = 2\omega_m\frac{\Delta h}{h} = \Delta z_*$. That is to say, the CMB estimate of H_0 can be raised if we consider also consider an increase in z_*. This procedure is what we will mean by modified recombination even though other aspects of recombination can also be modified such as its effective width.

Possibly the most straightforward way to allow for a higher z_* is to consider either a larger fine-structure constant, α_{EM}, or a larger electron mass, m_e, in the early universe enabling recombination to occur at a higher temperature and therefore a higher redshift. Both have been extensively studied (see [133–141])

with similar affects on cosmological fitting parameters. However, as discussed in [142], it is unlikely that a simple variation in α_{EM} will play a significant role in the H_0-tension while changes in m_e remain a viable solution. And even though the concept of varying fundamental constants has been around at least since the 1980s [143], to seriously consider a varying m_e as a possible solution to the H_0-tension then a convincing mechanism must be provided that would naturally enable m_e to differ between the early and late universe.

We consider the existence of the symmetron field, a scalar-tensor theory with a symmetry breaking potential and a universal coupling to the trace of the stress-energy tensor (see section 3.3 for detailed discussion on the symmetron model). We propose a Yukawa interaction between the electron and symmetron such that the screening mechanism has indirect control over the mass of the electron in addition to the strength of fifth force interactions. Just like the Higgs coupling to the electron, the symmetron coupling would naturally give a mass contribution to the electron proportional to the symmetron's vacuum expectation value (VEV)[1], ν. However, unlike the Higgs coupling, the symmetron's VEV depends on the background matter density of its environment. In regions of high density $\nu = 0$, while in low density regions it pulls off towards a finite value. With the Yukawa coupling, the electron mass would have an additional contribution which varies with the density of its environment. Therefore, an electron in a high density region (i.e. in the early universe) would have a different mass than one in a low density region (i.e. in low redshift interstellar gas clouds). This would enable a difference in m_e between recombination and the observed value today in Earth based measurements. In general a Yukawa interaction of this sort should be shared by other Standard Model particles but for

[1]Similar principles have been previously discussed in [144] and more recently in [145].

simplicity we focus only on the electron interaction.

The prospects of this mechanism are quite intriguing. It was studied in [87] that a varying electron mass by itself could reduce the tension from 4.7σ to 3σ in flat ΛCDM (using *Planck* 2018 TT,TE,EE+lowE in combination with Pantheon SNe [88] and BAO [146–148]) and in an $\Omega_k\Lambda$CDM model the tension can be reduced below 2σ. Even more intriguing though is the pairing of the work here with that in [149] which considers the effect of screened fifth forces on the cosmic distance ladder (the symmetron being one of the studied screening mechanisms). The authors show that if the local Cepheids callibrated with parallax measurements are more screened than the distant Cepheids used to anchor SNe then H_0 would be biased towards higher values[2]. In total, accounting for symmetron fifth forces may decrease the local estimates of H_0 while accounting for the electron-symmetron coupling may increase the CMB estimated value, relieving the tension two-fold.

Section 3.3 introduces the basics of the symmetron field and some of the current bounds on its parameters while section 3.5 discusses the details of the coupling necessary for shifting H_0 towards higher values. In section 3.6 we explore some possible observables of the coupling and we conclude in section 3.7.

3.3 Symmetron Field

Fifth force interactions are generally expected to accompany scalar theories. In most cosmological applications of scalar fields these fifth forces will need grav-

[2]The effect on the independent TRGB and MIRAS calibrations still need to be studied however.

itational strength interactions in order to have noticeable effects in their range of applications which, if unchecked, will cause apparent deviations from GR. But since stringent solar system tests are still in complete agreement with GR, these scalar fields must come with a mechanism of screening fifth force interactions at least at the length scale of the solar system. The Vainshtein [150] and chameleon [151] are two examples of screening mechanisms. Vainshtein screening uses non-linear scalar field fluctuations in curved space to suppress the canonically normalized kinetic term resulting in heavily damped fifth force interactions. Chameleon screening on the other hand uses an effective scalar field mass which scales with the background energy density so that in regions of high density (such as inside of a galaxy) the mass is high which drives the fifth force range below observational precision. We however consider a third screening mechanism, the symmetron, which is very similar in structure to the chameleon field but differs enough to be of interest. The symmetron field was originally introduced in [152] and discussed at length in [153]. And although it is beyond the interests of this chapter, [154] discusses possible UV completeness which will be touched upon in chapter 4.

In its original formulation the symmetron assumes a general scalar-tensor theory,

$$S = \int d^4x\sqrt{-g}\Big[\frac{1}{2}M_{Pl}^2R - \frac{1}{2}g^{\mu\nu}\partial_\mu\phi\partial_\nu\phi - V(\phi)\Big] + \int d^4x\sqrt{-\tilde{g}}\mathcal{L}_m(\psi,\tilde{g}) \quad (3.8)$$

where the matter fields, ψ, contribute in the last term and have a minimal coupling to the Jordan frame metric,

$$\tilde{g}_{\mu\nu} = A^2(\phi)g_{\mu\nu}. \quad (3.9)$$

The resulting equation of motion for the field ϕ is then

$$\Box\phi = V_{,\phi} - A^3(\phi)A_{,\phi}(\phi)\tilde{T} \tag{3.10}$$

where $\tilde{T}$ is the trace of the stress energy tensor in the Jordan frame for the matter fields. Generality is broken when we choose the forms

$$V = -\frac{1}{2}\mu^2\phi^2 + \frac{1}{4}\lambda\phi^4 \tag{3.11}$$

and

$$A = 1 + \frac{1}{2}\left(\frac{\phi}{M}\right)^2 + \mathcal{O}\left(\frac{\phi}{M}\right)^4 \tag{3.12}$$

with μ and M as two mass scales, λ as a dimensionless coupling constant, and the assumption that in all points of interest $\phi \ll M$ such that the power series expansion in (3.12) remains valid. The above two choices are the simplest functions satisfying the required $\mathbb{Z}_2$ symmetry but other choices may also have been made. For example, these forms are not suitable for a symmetron dark energy model given constraints from tests of gravity, but [153] explores more general forms of $V(\phi)$ and $A(\phi)$ that may be able to. We are not interested in dark energy here so the forms (3.11) and (3.12) will suffice. However, in the appendix we discuss a slight modification to both $V(\phi)$ and $A(\phi)$ that would have similar, but separately interesting, effects to those discussed in the main body of this text.

Noting that $A^3(\phi)\tilde{T} = A^3(\phi)(1-3w)\tilde{\rho} = (1-3w)\rho$ we do not expect coupling to the radiation sector of ψ. The only contributions will be from matter (both baryonic and dark matter, $w = 0$) and dark energy ($w = -1$), but in our interested density range we will only consider the matter contribution. A cou-

pling to radiation may also be considered given the arguments in [155] though these too will be ignored for simplicity. Using (3.11) and (3.12) in (3.10) gives

$$\Box\phi = V_{,\phi} + A_{,\phi}\rho \equiv V_{eff,\phi} \tag{3.13}$$

where we have defined an effective potential which to leading order in ϕ/M is

$$V_{eff} = \frac{1}{2}\Big(\frac{\rho}{M^2} - \mu^2\Big)\phi^2 + \frac{1}{4}\lambda\phi^4 \tag{3.14}$$

For convenience, we define the parameter Σ with dimension $[\text{mass}]^{-1}$ as

$$\Sigma^2 \equiv \frac{8\pi G}{3H_0^2}M^2 \tag{3.15}$$

which allows us to express the density in terms of the background fractional matter density of the universe, Ω,

$$V_{eff} = \frac{1}{2}\Big(\frac{\Omega}{\Sigma^2} - \mu^2\Big)\phi^2 + \frac{1}{4}\lambda\phi^4 \tag{3.16}$$

Thus, when $\Omega \geq \mu^2\Sigma^2$ the quadratic term is positive so that the VEV $\nu = 0$. However, when $\Omega < \mu^2\Sigma^2$ symmetry breaking occurs which pushes ν to a finite value. In total,

$$\nu = \begin{cases} 0 & \Omega \geq \mu^2\Sigma^2, \\ \sqrt{\frac{\mu^2\Sigma^2 - \Omega}{\lambda\Sigma^2}} & \Omega < \mu^2\Sigma^2. \end{cases} \tag{3.17}$$

The potential in these two regimes of Ω is sketched in figure 3.1 with arbitrary units. The transition rate between the solid and dashed curves is dependent on the growth/decay rate of Ω. In considering the symmetron near galaxies this transition is dominated by spatial growth of Ω as one looks from the outside

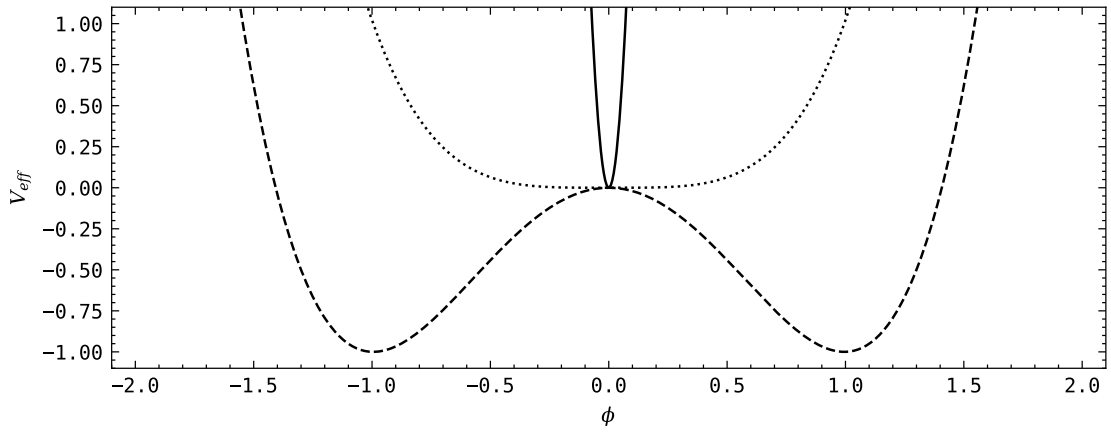

Figure 3.1: The symmetron potential in arbitrary units. The solid, dotted, and dashed curves show the potential when $\Omega \gg \mu^2\Sigma^2$, $\Omega = \mu^2\Sigma^2$, and $\Omega \ll \mu^2\Sigma^2$, respectively.

towards the inside of a galaxy. In these interests we write $\Omega = \Omega(r)$ and we consider for simplicity that the matter density of a galaxy is described by an NFW profile.[3] But when considering the symmetron through cosmic history the transition would be more sensitive to redshift which we will write as $\Omega = \Omega(z)$. This is important to note since we are comparing m_e during recombination to the value measured in our solar system which is suspended in a local over-density (i.e. the Milky Way galaxy).

3.4 Parameter Constraints

[152] has considered symmetry breaking in the symmetron field to occur in recent cosmological history such that unscreened long range interactions of gravitational strength could serve as an effective dark energy. This is not our interest here. Instead, we emphasize a difference in VEV between the densities present

[3]One can of course more accurately consider a baryonic disk structure embedded in a dark matter NFW profile. This will not affect the arguments in this paper, but it may loosen the parameter constraints marginally due to localized over-densities.

at recombination and today's local value,

$$\Omega_{rec} = \Omega_{m0}(1 + z_*)^3 \approx 4 \times 10^8 \tag{3.18}$$

$$\Omega_{MW} \approx 8 \times 10^4 \tag{3.19}$$

where an NFW fit to the Milky Way was used to calculate Ω_{MW}. This translates to $\mu^2\Sigma^2$ being greater than at least one of the above densities. Since the Milky Way on average has a lower density out of the two we impose

$$\mu^2\Sigma^2 > \Omega_{MW}. \tag{3.20}$$

Otherwise, if Ω_{rec} and Ω_{MW} were both greater than $\mu^2\Sigma^2$ then symmetry breaking would occur only in the intergalactic space of the late universe. With the discussion below in section 3.5 this corresponds to the symmetron-electron Yukawa coupling having no significant effect on the predicted value of H_0 which is of no interest here (though the regime could still be of general cosmological interest). On the other hand, if $\mu^2\Sigma^2$ is much larger than Ω_{rec} then symmetry breaking would occur much too early so that the VEV values between recombination and the Milky Way would be nearly indistinguishable and any effect on H_0 would be negligible. That is to say, for the symmetron to cause a significant enough mass difference between recombination and the measured value we must require

$$\mu^2\Sigma^2 \not\gg \Omega_{rec}. \tag{3.21}$$

Figure 3.2 shows both $\Omega(z)$ and $\Omega(r)$. The interesting range of $\mu^2\Sigma^2$ values lies in the darker green band, between recombination ($z = 1100$) and the radial position of the solar system inside the Milky Way ($r \approx 8.3kpc$). The shape of

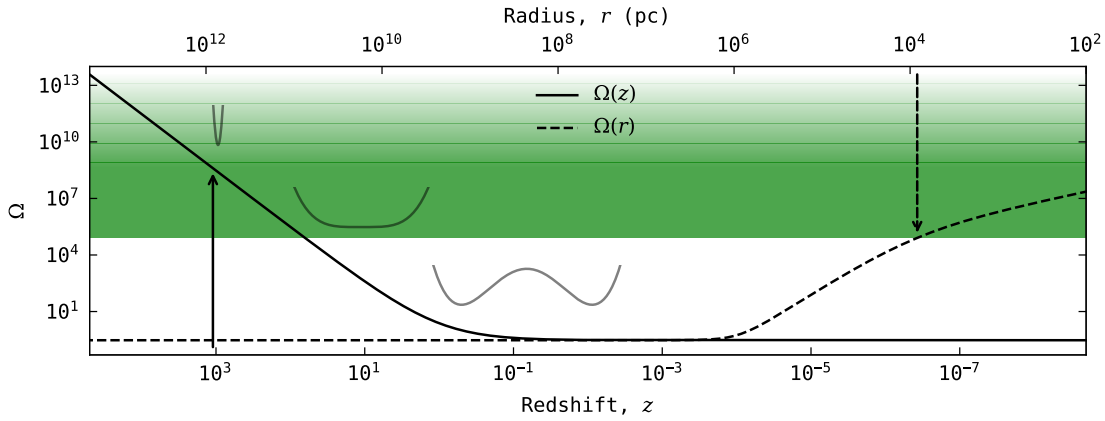

Figure 3.2: Cosmological matter density versus redshift (solid curve) and the Milky Way matter density versus radius (dashed curve) modeled using an NFW profile with fitting parameters taken from [156]. The solid arrow marks recombination while the dashed arrow marks the radial position of the solar system in the Milky Way. The green band highlights the expected values of $\mu^2\Sigma^2$ that would allow for a symmetron induced shift in the electron mass in accordance with the H_0-tension. The behavior of the potential before, at, and after symmetry breaking is shown in insets.

V_{eff} overlays the corresponding density ranges.

[152] further discusses local tests of gravity in order to constrain the parameter space and avoid apparent deviations from GR in the solar system. Since there have been no such deviations reported as of yet, the resulting constraints are still of interest here. Particularly, we will take

$$M \ll M_{Pl}. \tag{3.22}$$

Referring back to (3.20), this results in

$$\mu^2 \gg H_0^2. \tag{3.23}$$

Since the mass of small fluctuations around ν goes as $m_0 = \sqrt{2}\mu \gg H_0$ the

range of fifth force interactions would fall well inside the Hubble radius and may have a role in structure formation.

Laboratory tests have also placed bounds on the symmetron's parameter space (see [157, 158] for discussions). One could use these to constrain λ given the above constraints on μ and M; however, since we are not interested in a dark energy symmetron, the parameter space of interest here is far removed from those probed by laboratory tests. The parameter λ remains to be bounded.

3.5 Coupling to the Electron

We now consider a Yukawa interaction between the symmetron and the electron. This contributes an interaction term to the Lagrangian of the form

$$\mathcal{L}_{int} = -g_s \bar{e} e \phi \tag{3.24}$$

where g_s is the coupling strength between the electron and symmetron. If we take the mass contributions of the Higgs and symmetron fields to be η_H and η_s, respectively, then at all times the electron mass should be[4]

$$m_e = \eta_H + \eta_s. \tag{3.25}$$

[4]It should be noted that there are currently no constraints on g_H. The proposed Future Circular Collider (FCC-ee) may have the ability to probe the low luminosity $H \to e^+e^-$ process, possibly limiting additional components to the electron mass, as disscussed in [159].

The η_H term will take its constant canonical form, $\eta_H = \frac{g_H v_H}{\sqrt{2}}$, while

$$\eta_s = \frac{g_s \nu}{\sqrt{2}} = \begin{cases} 0 & \Omega \geq \mu^2 \Sigma^2, \\ g_s \sqrt{\frac{\mu^2 \Sigma^2 - \Omega}{2\lambda \Sigma^2}} & \Omega < \mu^2 \Sigma^2. \end{cases} \tag{3.26}$$

We note that since we have coupled matter to the Jordan frame metric in (3.9) the fermion mass term becomes $\mathcal{L}_{ferm.} = m_\psi A(\phi)\bar{\psi}\psi$ and (3.25) would have an additional contribution proportional to $m_e \nu^2 / M^2$. But as long as $|g_s| \gg 10^{-84}/\sqrt{\lambda}$ then we can safely take η_s as the dominant contribution and treat (3.25) as the electron mass in the symmetron coupled state. And although we do not apply the constraint here, if for instance one were to apply gravitational strength fifth force interactions as was done in [153] then we must require $|g_s| \gg 5 \times 10^{-23}$. In addition, including the interaction term (3.24), back reaction effects must be taken into account for the shape of V_{eff}. Since the interaction adds a term linear in ϕ to V_{eff} then the VEV will be shifted away from zero during the unbroken symmetry phase by an amount which varies with the electron density. There will also be a tilt in the symmetry broken phase creating a false vacuum. Overall these inclusions do not change the essence of our mechanism so we proceed by ignoring the back reactions and push their discussion to appendix B.

It was shown in [142] that the H_0-tension can be alleviated to within 2.8σ in the ΛCDM model with an electron mass at recombination given by

$$m_{e,rec} = \gamma m_{e,MW} \tag{3.27}$$

where $m_{e,MW}$ is the measured electron mass of 0.51MeV. The fitted parameter γ varied depending on the data sets involved but in all cases it fell in the range

$1 < \gamma < 1.02$. [87] considered the range, $0.95 < \gamma < 1.05$, in there fitting with an $\Omega_k\Lambda$CDM model, and have likewise found $\gamma > 1$ allows for a higher H_0. In either case, we note that γ deviates from unity by a small amount ($< 10\%$) and to alleviate the H_0-tension we impose $\gamma > 1$.

For concreteness we will consider $\Omega_{rec} \geq \mu^2\Sigma^2 > \Omega_{MW}$ which we emphasize by the darker horizontal green band in figure 3.2. With this choice, prior to and during recombination $\nu = 0$ and the electron mass is solely dependent on its Higgs field interaction, i.e. $m_{e,rec} = \eta_H$. But in lower densities like the immediate vicinity of the solar system the electron would have an additional mass term such that the measured electron mass is $m_{e,MW} = \eta_H + \eta_s$. Combining equations (3.25), (3.26), and (3.27) we find

$$\eta_s = g_s\sqrt{\frac{\mu^2\Sigma^2 - \Omega_{MW}}{\lambda\Sigma^2}} = -\tfrac{\gamma-1}{\gamma}\eta_H. \tag{3.28}$$

With $\gamma > 1$ the coupling constant would have to be negative, $g_s < 0$, meaning that the symmetron coupling reduces the electron mass.

3.6 Cosmological and Astrophysical Side Effects

An environment dependent electron mass should come with a number of observable effects. For instance, the Rydberg formula for atomic transitions in hydrogen gives the absorption/emission frequencies proportional to the electron mass,

$$f = m_e\alpha_{EM}^2(n_1^{-2} - n_2^{-2}). \tag{3.29}$$

If the symmetron coupling to the electron is actually at play then we would expect the spectrums from intergalactic hydrogen clouds to be shifted compared to hydrogen clouds near the cores of galactic halos. Given that m_e increases with density, lower density regions should be more redshifted than higher density regions. In general these shifts would be difficult to disentangle from cosmological redshifts unless precise distance measurements to the gas clouds are known independent of redshift observations. However, one could in principle see this effect as a systematic redshift in the 21cm line as one goes from the inner to the outer edges of a galaxy. The effect would be independent of the galaxy's rotation, instead following the density profile of the galaxy, and would also be independent of the cosmic distance making it distinguishable from cosmological redshift. Such a study would have a strong declaration on the validity of this mechanism.

Another interesting observable is in the progression of the electron mass through cosmological history. Particularly, as the cosmological matter density drops off as $(1+z)^3$ during the symmetry broken phase, the contribution to m_e given by 3.26 would go as $(1+z)^{1.5}$. Assuming the density of intergalactic gas clouds to be lower than the symmetry breaking value, $\mu^2\Sigma^2$, then the Lyman-α forest would have an additional redshift evolution in wavelength proportional to $(1+z)^{-1.5}$. Current Lyman-α surveys may then be used to place constraints on the fitting parameter λ.

3.7 Summary

We have discussed a simple mechanism that would enable the electron mass to vary between recombination and today's measured value. The density de-

pendent VEV of the symmetron field coupled to the electron serves as a control on the electron mass and shifts it to a lower value today assuming a coupling constant $g_s < 0$. The higher electron mass at recombination allows for recombination to occur at a higher temperature, increasing z_* and allowing H_0 to take higher values than currently estimated by *Planck*.

The parameter space of this model is still fairly open which makes confirmation, and more importantly invalidation, difficult. However, we noted that a predicted deviation proportional to $(1+z)^{-1.5}$ should be expected in the evolution of the Lyman-α forest along with a redshift profile across a galaxy following the galaxy's density profile. Both of these signals can be studied using existing data to constrain the parameter space. Given the simplicity of this solution and its application towards the prominent discussions of the H_0-tension it would serve well to explore this mechanism in greater detail.

Chapter 4

Swampland Conjectures

I now turn the last of our discussion towards the swampland and its conjectures. There are a growing many swampland conjectures in the field today. I will only focus on the two that I have published work on: the Weak Gravity Conjecture and the de Sitter Swampland Conjecture. My contributions in the latter work were secondary to Wei-Chen Lin who has used the work as a central point in his dissertation. So to avoid significant reiteration, I will speak only on the main points of the work and refer the reader to the original text, [160], for full details.

4.1 Introduction to the Swampland

Effective field theory (EFT) is an extremely useful tool in a physicist's arsenal, serving as an approximation of some underlying, more complicated physics which we do not quite understand fundamentally. As such, an EFT can only be valid within some range of length scales taken to be much higher than those of the actual physical phenomena. For example, it is very common to use an EFT approach to detail a dynamical dark energy model with the assumption

that some unknown physical interactions are governing dark energy at scales much smaller than galaxies. The symmetron discussed in chapter 3 is one such example of an EFT with a cutoff scale $M \ll M_{Pl}$. Even GR can be discussed as an EFT description of quantum gravity.

The downside of EFTs is that more than one can sufficiently describe a set of observations within respective energy scales. For instance, both the chameleon and symmetron fields can be used to describe dark energy even though they differ at more fundamental levels. There may in fact be a great number of fundamentally different EFTs that are all able to satisfy the same set of observations. So, in order to parse the more-likely-correct EFTs from the others, we can require that an EFT must be compatible with the theories that are expected to explain the smallest scales[1], otherwise called the UV limit. Any EFT found to be compatible with the UV limit is considered UV-complete. Thus, we define the swampland as the set of all low-energy EFTs found to be UV-incomplete while the landscape is defined as the complementary set. Our Universe, described by the SU(3)$\otimes$SU(2)$\otimes$U(1) Standard Model, may be just one of many possibilities in the landscape (see figure 4.1 for an illustration of our place in field space).

Checking the UV-completeness of every EFT is clearly impractical. Instead, it is far easier to construct simple conjectures which are argued for from the UV limit (i.e. expectations from quantum gravity) but can be broadly applied at the EFT level so that any EFT caught violating the conjectures is easily thrown into the swampland and conditionally forgotten.

[1]For the purpose of this discussion I will broadly consider string theory as a proper description of the smallest scales.

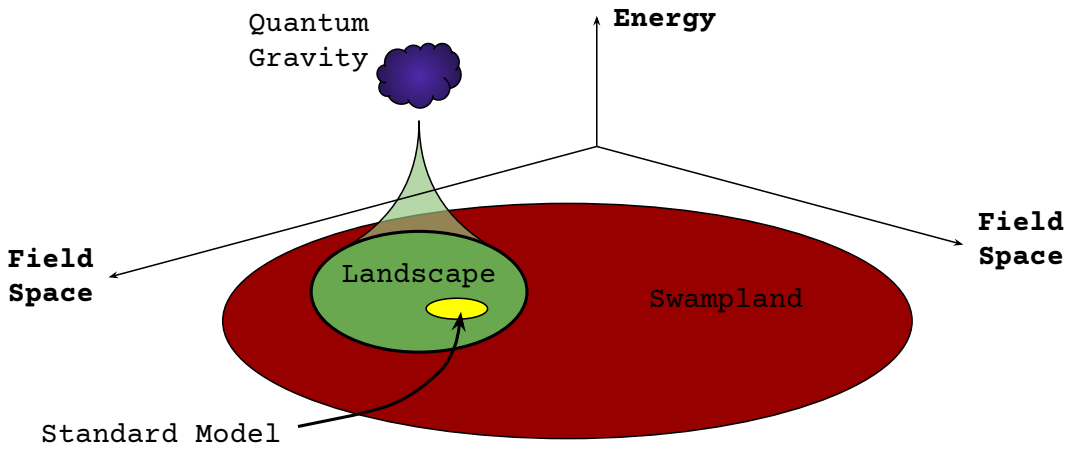

Figure 4.1: Illustration of the low-energy EFTs describing our Universe (yellow), not describing our Universe but still compatible with quantum gravity (green), and all those incompatible with quantum gravity (red).

4.2 Weak Gravity Conjecture

4.2.1 The Original Weak Gravity Conjecture

The Weak Gravity Conjecture (WGC), originally proposed in [161], poses that any possible U(1) gauge field (e.g. electromagnetism) must have at least one charged particle with charge-to-mass ratio of

$$\frac{q}{m} \geq 1 \tag{4.1}$$

in properly chosen units[2]. A small handful of simple, back-of-the-envelope arguments were originally given for its necessity, but of particular interest here is the argument based on BH evaporation and stable remnants. In short, the argument goes as follows. A BH with mass M can have any U(1) charge Q as long as $Q \leq M$ for reasons discussed earlier in chapter 1.1.2. We can imagine

[2] All Standard Model particles with U(1) charge satisfy this by many orders of magnitude.

that the BH then Hawking evaporates away its mass[3] until it reaches the extremal bound, $M = Q$. If the U(1) field has no particles with $q \geq m$ then the evaporation process cannot proceed past this state and the BH then constitutes a zero-temperature stable remnant. We are thus faced with the formation of a large number of stable remnant states with charge anywhere between 0 and Q. As a result, any thermodynamic system with U(1) gauge field interactions and sufficient energy would be infinitely biased towards the production of these zero-temperature remnants. This scenario is not favored for many reasons, not the least of which would be an overclosure of the early universe and a distortion of BBN predictions due to an early production of zero-temperature BHs with a dust equation of state, $w = 0$ [162]. Therefore, the conjecture (4.1) is required in order for the extremal BH states to be unstable against further decay processes. See figure 4.2 for a cartoon representation of the argument.

From an astrophysical point-of-view, the formation of extremal BHs are exceedingly unlikely due to the net neutral charge of large systems. However, taking the T.H. White approach of "everything which is not forbidden is compulsory," the possibility of these zero-temperature stable remnants is enough to cause great concern.

With the need for the WGC now being well argued for it still remains to be shown if the conjecture can be proven from first principle arguments. There have been attempts though with [163] being quite notable in its employment of BH thermodynamical arguments. A proof of the WGC is not the intent here. Over the next few sections I will instead extend the WGC's BH arguments with a completely general relativistic approach and show that the WGC continues to

[3]We usually imagine BHs evaporate down to the Planck mass after which it is unclear what happens since quantum gravity takes over.

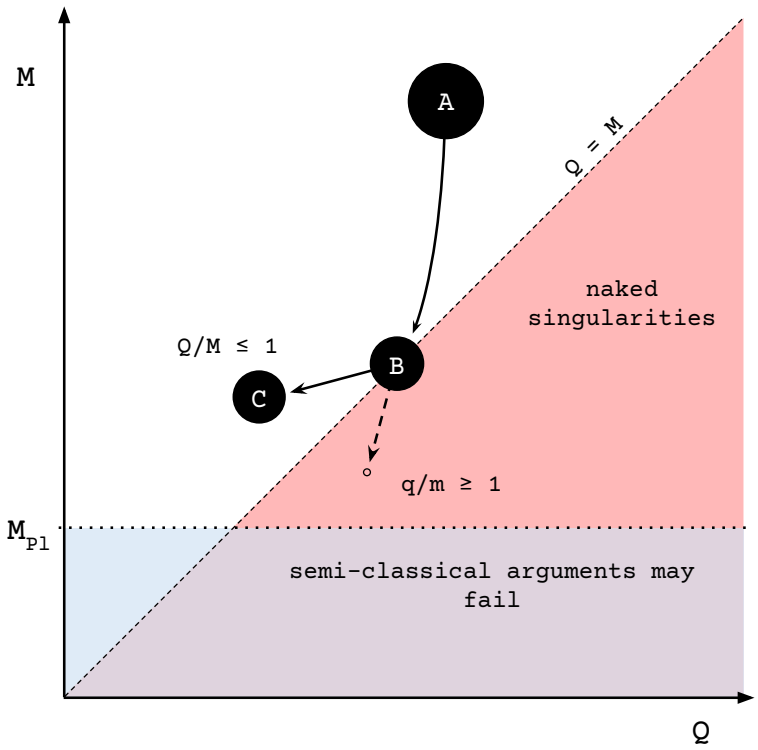

Figure 4.2: The black hole A undergoes evaporative processes until it reaches the extremal state B. The only way for B to evaporate further without forming a naked singularity is by the emission of particles (empty circle) with $q \geq m$.

hold as long as the corresponding BH mass is understood to be the ADM mass. This discussion closely follows my original work in [164].

4.2.2 Generalizing the Weak Gravity Conjecture

The Reissner-Nordström (RN) BH is a vacuum solution to a spacetime geometry containing a central mass, M, and a U(1) gauge charge, Q. The RN metric can be expressed as

$$ds^2 = -f(r)dt^2 + f^{-1}(r)dr^2 + r^2 d\Omega^2. \tag{4.2}$$

where $d\Omega^2 \equiv \sin^2\phi d\theta^2 + d\phi^2$ and

$$f(r) \equiv \left(1 - \frac{2M}{r} + \frac{Q^2}{r^2}\right) \tag{4.3}$$

which we see takes the Schwarzschild form in the limit $Q \to 0$. Finding the resulting horizon is as simple as solving $f(R) = 0$, but due to quadratic dependence of the charge term gives two real horizon radii,

$$R_\pm = M \pm \sqrt{M^2 - Q^2}. \tag{4.4}$$

Only in this chapter have we used $m_{Pl} = 1$ such that Q and M are of the same dimension. On the other hand, taking $Q > M$ results in the geometry of the RN solution no longer housing an event horizon, signaled here by the radii taking complex values. Without the event horizon the BH singularity is left bare in apparent violation of the cosmic censorship conjecture (CCC).

It is evident then, if the CCC is not to be violated, that the BH evaporation process should not be able to continue past the extremal bound. This is no issue for Hawking evaporation since the Hawking temperature for a RN BH goes as

$$T = \frac{1}{2\pi}\frac{\sqrt{1-Z^2}}{1+\sqrt{1-Z^2}} \tag{4.5}$$

where for convenience I have defined $Z \equiv Q/M$ and similarly I define for later use $z \equiv q/m$. Clearly, as the BH approaches the extremal bound, $Z \to 1$, the temperature approaches absolute zero, $T \to 0$. Other decay channels such as the Schwinger effect would in principle continue to enable further decay for sufficiently large electric fields, but this too will slow to a halt for extremal BHs on the order of the Planck mass.

In [165] a similar BH is considered and is allowed to completely decay away into a final state of $n = Q/q$ particles. From energy conservation we then require $M \geq nm$, or more succinctly

$$z \geq Z \tag{4.6}$$

which reduces to the WGC in the extremal limit. [165] further argues that it is not sufficient for just one particle in the spectrum to satisfy (4.6) but that some weighted average of the available species must[4]. We take a similar stance in section 4.2.2.1. But while [165] concerns the charge-to-mass ratio of the entire final state, we break up the final state into thin charged shells and show that each shell, when emitted, must satisfy the bound as well.

It is worth noting that, including higher order derivative terms in the RN solution, the extremal bound could become a mass dependent function, pulling away from $Q = M$ at small masses [166]. Depending on the signs of the corrections, which remain to be proven, the lower mass extremal bound will either be pushed into the $Q < M$ or $Q > M$ space. Some physical arguments have been made ([167–171]) calling for the extremal bound to be pushed towards the $Q > M$ space which would conveniently allow for small, over-charged BHs themselves to satisfy the WGC. For convenience we will ignore these corrections.

[4]One could consider this as the "weaker" gravity conjecture (WerGC) in analogy to the equivalence principles. The "weakest" gravity conjecture (WestGC) would then be the proposal that all particles in the U(1) spectrum would have to satisfy $z \geq 1$. In this case the Standard Model would be in violation of the newly minted WestGC due to the photon.

4.2.2.1 Shell Emission

Consider again a BH of mass and charge (M, Q) satisfying $Z \leq 1$ decaying to a state (M', Q') satisfying $Z' \leq 1$. We take this to be done by the emission of a charged, thin, mass shell of rest mass m and charge q. We could imagine the mass shell to be the dominant s-wave of a scalar field (see [172]), or as a locus of U(1) charged particles – since the WGC is a general result it should bound these decay modes as well. In the case of the locus of particles, assuming the shell to be a uniform distribution of identical particles, the charge-to-mass ratio of the shell will be the same as the individual particles making up the shell.

In order to satisfy charge conservation the charge of the BH before and after decay should be related by

$$Q = Q' + q. \tag{4.7}$$

For the derivation of the mass relation, we refer to Fig. 4.3 notation purposes. In the moments after the decay process, the BH is enveloped by a then mass shell which divides the space into two: inside the shell (region I) and outside (region II). The presence of the mass shell causes a discontinuity in the extrinsic curvature tensor, K_{ij}, between regions I and II. The discontinuity at the shell, denoted by the square brackets, can be expressed as (see [6] or [173] for derivation)

$$[K^j{}_i] = 8\pi\sigma\left(u^j u_i + \frac{1}{2}\delta^j{}_i\right) \tag{4.8}$$

where σ is the mass density of the shell such that $4\pi R^2\sigma = m$, the ADM rest mass of the shell, and $\mathbf{u}$ is the 4-velocity of the shell. Considering the shell to

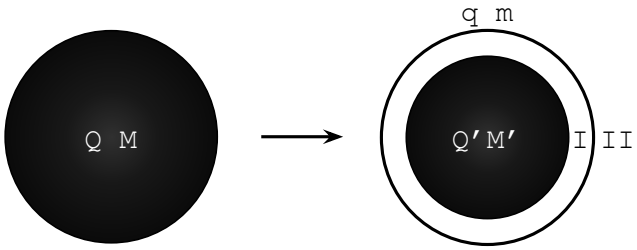

Figure 4.3: A BH decays through the emission of an outward moving thin, charged mass shell. The shell divides the space into two regions, interior (I) and exterior (II).

only have radial motion (i.e. $g_{\theta\theta}u^{\theta}u_{\theta} = 0$), we find that

$$[K_{\theta\theta}] = 4\pi g_{\theta\theta}\sigma = 4\pi R^2\sigma = m. \tag{4.9}$$

We have implicitly assumed a dust equation of state for the shell in (4.8) so we cannot naively take the limit $m \to 0$. Furthermore, we note that q contributes to the discontinuity (4.9) only through its energy content which is already taken into account in m (see [174]).

The discontinuity in the extrinsic curvature can also be directly obtained by taking the difference between the extrinsic curvature tensor inside and outside the shell,

$$[K^j_{\ i}] = K^{j\ (II)}_{\ i} - K^{j\ (I)}_{\ i}. \tag{4.10}$$

We express the RN metrics inside and outside the shell[5] as

$$ds_I^2 = -f_I(r)dt_I^2 + f_I^{-1}(r)dr^2 + r^2d\Omega^2, \tag{4.11}$$

$$ds_{II}^2 = -f_{II}(r)dt_{II}^2 + f_{II}^{-1}(r)dr^2 + r^2d\Omega^2 \tag{4.12}$$

[5]Notice, [175] has shown that the time coordinates in the two regions must differ in order for the two regions to match at the boundary.

where

$$f_I(r) \equiv \left(1 - \frac{2M'}{r} + \frac{Q'^2}{r^2}\right), \tag{4.13}$$

$$f_{II}(r) \equiv \left(1 - \frac{2M}{r} + \frac{Q^2}{r^2}\right). \tag{4.14}$$

Calculating the extrinsic curvature tensor in both regions we obtain

$$[K_{\theta\theta}] = -R\left(\sqrt{f_{II}(R) + v^2} - \sqrt{f_I(R) + v^2}\right) = m. \tag{4.15}$$

where $u^r = v$ is the radial speed in the rest frame of the shell and R is the radial size of the mass shell centered on M'. Solving (4.15) for M' we can get

$$M' = M + \frac{q^2 - m^2 - 2qQ}{2R} - m\sqrt{f_{II}(R) + v^2}. \tag{4.16}$$

Notice that M, M', and m are the constant ADM masses. So if we let $R \to \infty$ then we find

$$M' = M - m\sqrt{1 + v_\infty^2}, \tag{4.17}$$

which one might have guessed allowing for the possibility that m still has some kinetic energy far removed from the BH. In order for the BH to eventually decay away we must impose $Z \geq Z'$, which combined with (4.7) and (4.17) and taking $v_\infty = 0$ we find

$$z \geq Z \tag{4.18}$$

in agreement with (4.6). This reduces to the original WGC in the extremal limit but generalizes the argument to non-extremal BHs. In addition, the condition for complete evaporation of non-extremal BHs is relaxed in comparison

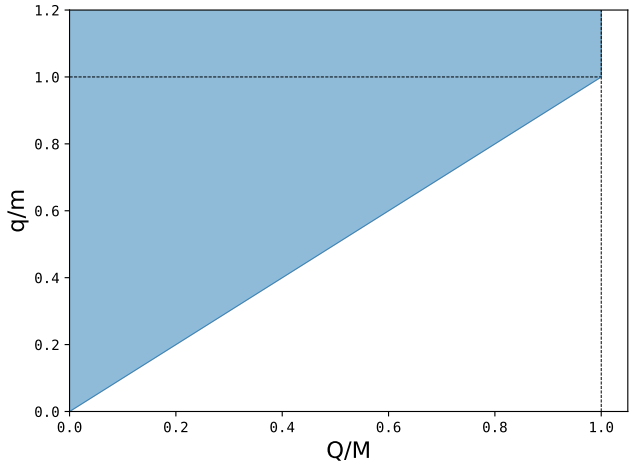

Figure 4.4: The shaded region marks those charge-to-mass ratios of a shell that would allow for a BH of (M, Q) to evaporate away from extremality. Dashed lines mark the $q = m$ and $Q = M$ bounds.

to WGC. That is to say, states with $q/m \leq 1$ can also reduce the Q/M ratio of a BH.

As an important consequence, the condition in Eq. (4.18) also allows us to directly relate the particle content of the theory with the spectrum of BH states. We show this in Fig. 4.4.

Admittedly, going from (4.16) to (4.17) we assumed the shell to be able to escape from the BH which is not generally guaranteed. To be more precise we can require

$$M + \frac{q^2 - m^2 - 2qQ}{2R} - m\sqrt{f_{II}(R) + v^2} \leq M - m$$

which is equivalent to $M' \leq M - m$. If we consider the most extreme case where the shell originates from the horizon of the original BH, $R = M + \sqrt{M^2 - Q^2}$,

then solving for v gives

$$v \geq 1 + (z^2 - 1)\frac{m}{2R} - z\frac{Q}{R} \tag{4.19}$$

where z is defined in the same way as in (4.6). Thus, for the shell to escape to infinity we would require

$$2zQ \geq (z^2 - 1)m \tag{4.20}$$

or equivalently

$$2qQ + m^2 \geq q^2 \tag{4.21}$$

which is trivially satisfied since $q \leq Q$. That is to say, charged shells are generally able to escape the near-horizon region of a BH, and as long as the shell's charge-to-mass ratio is at least that of the original BH's then it will allow the BH to recede from extremality.

4.2.2.2 Summary

In principle, if we require that BHs are allowed to evaporate completely without crossing the extremal bound we can connect the charge-to-mass ratio of the RN BH and the particle content in a theory. Formerly, the WGC and its extensions have shown that at least one far removed particle – or a combination of far removed particles – available in a U(1) spectrum must satisfy $q/m \geq 1$. Here we have used the outflow of a charged thin shell to show that the WGC continues to hold as the shell escapes the near horizon geometry and thereby we have tied the WGC explicitly to BHs. This agreement has come at the requirement that the shell have at least the necessary escape velocity from the BH which in the extremal limit is found to be zero for a shell with $q/m \geq 1$ (see equation (4.19)).

We also wish to note that our main result,

$$\frac{q}{m} \geq \frac{Q}{M}, \tag{4.22}$$

directly connects a general charged BH and particle spectra for a particular U(1). One could perhaps conjectured or guessed this very relationship, however here we obtained it by solving an exact general relativistic problem. As an interesting consequence of (4.22)), particles with $q/m \leq 1$ can also reduce Q/M ratio of a BH with $Q < M$.

In addition, in some cases, the relation can apply to the creation of BHs in addition to their evaporation. For example, we can consider a U(1) with only one particle species. If the species had $q/m < 1$ it would apparently violate the original WGC, but not our relation Eq. (4.22)). In such a theory, BHs would stay safely away from the extremal bound since collapse and/or accretion of particles with $q/m < 1$ could produce only BHs with strictly $Q < M$. As a richer particle spectrum is considered a wider variety of BHs can be produced.

Furthermore, while we are in agreement with previous results, knowing that a shell of particles emitted from an extremal BH must also satisfy $q/m \geq 1$ could allow us to use the production rates of particles to further constrain the necessary charge-to-mass ratio needed in a theory. For instance, if two charged species ($i = 1, 2$) exist in a U(1) then the shell will consist of some percentage of $i = 1$ particles and $i = 2$ particles with their contribution depending on their production rate. So if species 1 has $q_1/m_1 \ll 1$ but a very high production rate at the extremal bound compared to species 2, that is to say $\langle N_1 \rangle \gg \langle N_2 \rangle$, then species 2 would not only need $q_2/m_2 \geq 1$ but instead $q_2/m_2 \gg 1$. This could in turn further narrow down the allowed particle content in the theory. This

idea follows the work done in [176] for the electron-positron pair production through the Schwinger effect.

4.3 A $P(X, \varphi)$ Inflationary Theory in Light of the de Sitter Swampland Conjectures

In chapter 1.4 I discussed both the standard inflationary model with a potential $V(\phi)$ and k-inflation or a $P(X, \varphi)$ model. I also discussed how both models can sufficiently source the expansion necessary to solve the horizon problem along with the flatness and magnetic monopole problems as long as the slow roll conditions, (1.35) and (1.37), were satisfied. However, as I will introduce in the next section, the de Sitter Swampland Conjecture (dSSC) is in severe tension with the slow roll paradigm of standard single field inflationary models due to the dSSC's bounds on the gradient of the potential. The dSSC thus provides strong constraints in the formulation of other potential driven inflationary models. But it is not clear how the dSSC is applied to $P(X, \varphi)$ models which does not require a defined potential. There are attempts at generalizing the dSSC (see [177, 178]) in order to include $P(X, \varphi)$ theories, but we instead take a new approach considered in [178–180] which embeds the $P(X, \varphi)$ theory into a curved two-field space metric.

4.3.1 The de Sitter Swampland Conjecture

Observations from both low and high redshifts (e.g. accelerated expansion and $\Omega_\Lambda \approx 0.7$, respectively) provide significant evidence that our Universe has a de Sitter (dS) vacuum ($\Lambda > 0$). If the Universe continues to agree with the

ΛCDM model then it will eventually evolve into a dS one in the distant future. Moreover, the inflationary period of the very early Universe must have also been very similar to a dS universe. We would then expect that a dS vacuum can be constructed from string theory, but so far none have been shown rigorously without objection [181–183]. Given the difficulty of constructing dS vacua from string theory, the possibility that string theory is not compatible with dS vacua has begun to be considered in the form of the dSSC.

Now, a dS vacuum can be produced in two ways: (i) it could be that we have a scalar field potential, V, with the scalar field resting in a local minimum, (ii) or a scalar field slowly rolling down a sufficiently flat potential (like that discussed in section 1.4). In order to keep from forming a dS vacuum we can argue that

$$\epsilon_V \equiv M_{Pl}^2 \frac{V_{,\phi}^2}{V^2} \geq c \sim \mathcal{O}(1) \tag{4.23}$$

thus making it so that neither a potential minimum nor a sufficiently flat potential can form a positive cosmological constant. The original proposal of the dSSC [184] argues for a bound of $c < \sqrt{2}$ in order to still have an accelerated Universe while [185] finds $c \lesssim 0.6$ is required for quintessence models. The bound is in clear tension with a slowly rolling single-field inflationary field which satisfies (1.36), but potentially more complicated realizations of inflation may still be consistent with the dSSC. Multi-field inflation, which is detailed in the next section, provides a clean way around violating the dSSC but it is unclear how $P(X, \varphi)$ models are affected. It is possible however to embed a $P(X, \varphi)$ model into a multi-field model as its low energy effective description. From this point of view, we have shown that the dSSC can place useful constraints on $P(X, \varphi)$ models.

4.3.2 Multi-field Inflation

Standard inflation uses the simplest single-field scenario and has been successful at explaining observations in doing so. But there are no reasons why we should expect there to be only one scalar field; it may be the case that there are many scalar fields forming a complex field space through which the trajectory of the inflaton can still satisfy the slow roll conditions and produce the necessary exponential-like expansion in the very early Universe.

Let us consider the two fields $\phi = \{\varphi, \chi\}$ described by the non-linear sigma model

$$S = \int \mathrm{d}x^4 \sqrt{-g}\Big[\frac{M_{Pl}}{2}R - \frac{1}{2}G_{IJ}(\phi)\partial^\mu\phi^I\partial_\mu\phi^J - V(\phi)\Big] \tag{4.24}$$

where G^{IJ} is the field metric with $\{I, J\}$ indexing the fields. Per the usual, the first Friedman equation becomes

$$H^2 = \frac{1}{3M_{Pl}^2}\Big(\frac{1}{2}\dot{\Phi}^2 + V\Big) \tag{4.25}$$

where we have defined $\dot{\Phi} = \sqrt{G_{IJ}\dot{\phi}^I\dot{\phi}^J}$. By introducing the notation $V_I \equiv \partial V/\partial\phi^I$ along with the covariant time derivative, $D_t A^I \equiv \dot{A}^I + \Gamma^I_{JK}\dot{\phi}^J A^K$, we can express the EoM for the fields as

$$D_t\dot{\phi}^I + 3H\dot{\phi}^I + G^{IJ}V_J = 0. \tag{4.26}$$

Thus, the first slow roll parameter for the multifield case can be expressed as

$$\epsilon = \frac{\dot{\Phi}^2}{2H^2M_{Pl}^2} \tag{4.27}$$

with the form of the second slow roll parameter following suit.

The field space metric may in general be non-trivial so it is easier to discuss the trajectory of the inflaton through the use of the tangent field vector,

$$T^I = \frac{\dot{\phi}^I}{\dot{\Phi}} \tag{4.28}$$

which describes the field components tangent to the field's trajectory and, conversely, the normal field vector,

$$N^I = -\frac{D_t T^I}{|D_t T|} \equiv -\frac{D_t T^I}{\Omega} \tag{4.29}$$

where we introduce the turning rate, $\Omega \equiv |D_t T|$, characterizing how windy the trajectory is through field space. We can project the EoM into the tangent and normal fields, respectively, so that

$$\ddot{\Phi} + 3H\dot{\Phi} + V_T = 0, \tag{4.30}$$

$$\Omega = \frac{V_N}{\dot{\Phi}} \tag{4.31}$$

where $V_T \equiv T^I V_I$ and $V_N \equiv N^I V_I$ describe the change in potential along the trajectory's tangent and normal directions. Thus, the trajectory through field space is then controlled by both the shape of the potential and the field space metric allowing for a sufficiently slowly rolling trajectory through a steep potential. This is easiest to see quantitatively with the first potential slow roll parameter,

$$\epsilon_V \equiv \frac{M_{Pl}^2}{2}\frac{V^I V_I}{V^2} = \frac{\epsilon}{(3-\epsilon)^2}\Big[\Big(3 - \epsilon + \frac{\eta}{2}\Big)^2 + \frac{\Omega^2}{H^2}\Big]. \tag{4.32}$$

Assuming $\eta \ll \epsilon \ll 1$, to leading order in slow roll parameters this can be

reduced to

$$\epsilon_V \approx \epsilon\left(1+\frac{\Omega^2}{9H^2}\right). \tag{4.33}$$

Thus, if the turning rate is large in a Hubble time then we can have an $\epsilon_V \gtrsim 1$ satisfying the dSSC while $\epsilon \lesssim 1$ satisfying slow-roll inflation.

Before proceeding with the embedding of a $P(X,\varphi)$ model into a multi-field space it is worth noting again that single-field inflation is quite successful. So if there are instead many fields sourcing inflation then the field space metric must conspire to give a trajectory that is effectively described by a single field. In the two-field case, the effective mass of the isocurvature perturbations can be written as

$$M_{eff}^2 = V_{;NN} + \epsilon H^2 M_{Pl}^2 R_{fs} - \Omega^2 \tag{4.34}$$

where $V_{;NN} \equiv N^I N^J V_{;IJ}$ is the normal projection of the covariant Hessian of the potential while R_{fs} is the Ricci scalar for the field space. If the effective mass of the isocurvature modes is very large compared to the Hubble parameter, $M_{eff} \gg H$, then the isocurvature modes can be integrated out to give an effective single-field model with a reduced speed of sound

$$c_s^2 = \left(1+\frac{4\Omega^2}{M_{eff}^2}\right)^{-1}. \tag{4.35}$$

This argument only holds at the perturbation level, but in the case of the gelaton model [186] and other related models [187] taking $M_{eff} \to \infty$ allows the isocurvature modes to be integrated out at the full action level making the effective single-field behaviour a general feature of the model.

4.3.3 Embedding a $P(X, \varphi)$ Theory into a Multi-Field Model

The embedding process begins by considering a two-field space containing the inflaton field, φ, satisfying a $P(X, \varphi)$ theory and an auxiliary field, χ,

$$S = \int \mathrm{d}x^4 \sqrt{-g}\Big[\frac{M_{Pl}^2}{2}R + P(X, \varphi) - \frac{1}{2\Lambda^6}(\partial\chi)^2 + (X - \chi)P_\chi\Big]. \tag{4.36}$$

This action can be viewed as a non-linear sigma model with a field space metric

$$G_{IJ} = \mathrm{diag}(\Lambda^{-6}, P_\chi) \tag{4.37}$$

and a potential

$$V(\phi) = -P + \chi P_\chi. \tag{4.38}$$

As such, the EoM for the auxiliary field can be found to be

$$\Lambda^{-6}\Box\chi + P_{\chi\chi}(X - \chi) = 0 \tag{4.39}$$

where in the case that $\Lambda \to \infty$ the auxiliary field approaches $\chi = X$ (provided that $P_{\chi\chi} \neq 0$) leaving the low energy theory as an effective $P(X, \varphi)$ model. Using the previously defined functions, in the large Λ limit, the turning rate to leading order can be written as

$$\Omega^2 \approx \Lambda^6 \frac{\dot{\varphi}^2 P_{\chi\chi}^2}{4P_\chi}. \tag{4.40}$$

Likewise the tangent and normal vector directions take the form (we have chosen the field index ordering $\{\chi, \varphi\}$)

$$T^I \approx \frac{1}{\sqrt{P_\chi}}\Big(\frac{\dot{\chi}}{\dot{\varphi}}, 1\Big), \tag{4.41}$$

$$N^I \approx \Lambda^3(-1, \Lambda^{-6}\frac{\dot{\chi}}{P_\chi \dot{\varphi}}), \tag{4.42}$$

respectively. The effective mass of the isocurvature modes can then be express as

$$M_{eff}^2 \approx \Lambda^6 \frac{P_{\chi\chi}}{4}\left(4 + \frac{(2\chi - \dot{\varphi}^2)P_{\chi\chi}}{P_\chi}\right) \tag{4.43}$$

showing that taking the $\Lambda \to \infty$ limit would enable the isocurvature modes to be integrated out and the two-field model to behave as a single-field model. In actuality, for the isocurvature modes to be integrated out we just need $M_{eff} \gg H$. At the same time, M_{eff} should have an upper cutoff as well, let us say $M_{eff} < E$. It has been argued in [188] that to avoid strong couplings in the $P(X, \varphi)$ theory an upper energy scale cutoff should be considered near

$$E^4 \approx 16\pi^2 M_{Pl}^2 |\dot{H}| \frac{c_s^5}{1 - c_s^2}. \tag{4.44}$$

From the lower and upper bounds, we see that our embedding scheme remains valid only in the mass range

$$\frac{XP_X}{M_{Pl}^2 \epsilon} \ll M_{eff}^2 < 4\pi\sqrt{XP_X \frac{c_s^5}{1 - c_s^2}} \tag{4.45}$$

or in terms of Λ,

$$\frac{2X^2}{M_{Pl}^2 \epsilon}\frac{c_s^2}{1 - c_s^2} \ll \Lambda^6 < \frac{4\sqrt{2}\pi X}{\sqrt{P_{XX}}}\frac{c_s^{7/2}}{1 - c_s^2}. \tag{4.46}$$

In total, the lower limit ensures our ability to integrate out the auxiliary field while the upper limit avoids strong couplings in the $P(X, \varphi)$ theory. A simple result can be seen from these bounds. By comparing the much larger upper

bound to the smaller lower bound, consistency dictates that

$$H \ll \frac{4\pi c_s^{5/2}}{\sqrt{1-c_s^2}}\sqrt{\epsilon}M_{Pl}. \tag{4.47}$$

Alternatively, using (1.50) the lower bound can also be written in terms of the slow roll parameters,

$$\Lambda^6 \gg \frac{4X^2}{\epsilon M_{Pl}^2}(\eta - 2\epsilon - \tilde{\kappa})^2 \tag{4.48}$$

With the caveat of the mass range argued for we can now move on to the potential slow roll parameter for a $P(X,\varphi)$ model. In the embedding scheme we can use the multi-field definition of ϵ_V given by 4.32 which to leading order in Λ and with $\epsilon, \eta \ll 1$ gives

$$\epsilon_V < \sqrt{(1-c_s^2)c_s}\epsilon^{3/2}\frac{\pi M_{Pl}}{9H}. \tag{4.49}$$

From this relation, the dSSC can be satisfied in a $P(X,\varphi)$ theory as long as the Hubble paramter satisfies

$$H < \sqrt{(1-c_s^2)c_s}\epsilon^{3/2}\frac{\pi M_{Pl}}{9}. \tag{4.50}$$

Therefore, in order for the embedding to work the $P(X,\varphi)$ theory must satisfy (4.47) while also satisfying (4.50) for the purpose of the dSSC.

4.3.4 Conclusion

We have examined a general embedding of a single-field $P(X,\varphi)$ inflationairy theory into a two-field theory with a non-trivial field space metric. The embedding treats the single-field theory as the low energy limit (i.e. $\Lambda \to \infty$) of

the two-field theory where the heavy field responsible for production of isocurvature modes can be integrated out at the full action level. This is done by considering the action

$$S = \int \mathrm{d}x^4 \sqrt{-g}\Big[\frac{M_{Pl}^2}{2}R + P(X,\varphi) - \frac{1}{2\Lambda^6}(\partial\chi)^2 + (X-\chi)P_\chi\Big] \tag{4.51}$$

where φ is the inflaton field, X is its canonical kinetic term, and χ is the auxiliary field. It is easy to see that in the limit $\Lambda \to \infty$ the auxiliary field tends towards $\chi = X$ and the single-field $P(X,\varphi)$ theory is retained. This limit does not hold exactly due to strong couplings in the $P(X,\varphi)$ model at very high Λ so the embedding is not perfect. The true range of Λ is instead given by (4.46). Calculations at next to leading order in Λ are given in the original text [160].

Using the upper bound on Λ we find that ϵ_V cannot be arbitrarily large in this model and must satisfy

$$\epsilon_V < \sqrt{(1-c_s^2)c_s}\epsilon^{3/2}\frac{\pi M_{Pl}}{9H} \tag{4.52}$$

or, if we take $\epsilon_V \sim \mathcal{O}(1)$ then the dSSC applies an upper bound on the inflationary energy for this type of model given by

$$H < \sqrt{(1-c_s^2)c_s}\epsilon^{3/2}\frac{\pi M_{Pl}}{9} \tag{4.53}$$

which can be compared a similar bound imposed in k-inflation models from the trans-Planckian censorship conjecture [189].

Appendix A

The symmetron in rewind

In chapter 3 we discuss an electron mass difference between recombination and today sourced by a Yukawa coupling with the symmetron field. Choosing the forms (3.11) and (3.12) would make the electron mass at recombination approximately the bare mass (i.e. contributions only from the Higgs field) while the value measured today is in combination with the effect from a non-zero symmetron VEV. However, we could also consider minimal changes to (3.11) and (3.12):

$$V(\phi) = \Big(-\frac{1}{2}\mu^2\phi^2 + \frac{1}{4}\lambda\phi^4 \Big) \to \Big(+\frac{1}{2}\mu^2\phi^2 + \frac{1}{4}\lambda\phi^4 \Big), \tag{A.1}$$

$$A(\phi) = \Big(1 + \frac{\phi^2}{2M^2}\Big) \to \Big(1 - \frac{\phi^2}{2M^2}\Big) \tag{A.2}$$

which together give a slightly modified V_{eff},

$$V_{eff} = \frac{1}{2}\Big(\mu^2 - \frac{\omega}{\Sigma^2}\Big)\phi^2 + \frac{1}{4}\lambda\phi^4. \tag{A.3}$$

Now, with the changes, the symmetron is in a broken symmetry phase in the early with a non-zero VEV and then when $\Omega = \mu^2\Sigma^2$ the field undergoes a

symmetry *restoration*. Therefore, the contribution to the electron mass is now in the early universe and nearly absent today. Taking $\Omega_{MW} < \mu^2\Sigma^2 \leq \Omega_{rec}$ and $g_s > 0$ one can reproduce a larger electron mass at recombination than is measured today just like what was argued in chapter 3.

There is no obvious advantage to this approach over what was discussed in chapter 3 besides one's possible preference. However, besides possibly the effect on theoretical quark stars, this alternative approach would not display any of the astrophysical effects discussed in section 3.6 due to the VEV being zero in most of the considered systems.

Appendix B

Back reactions from symmetron-electron coupling

The discussion in chapter 3 ignores the effect of the additional Yukawa coupling on V_{eff}. This was done for the sake of simplicity, but now we explore these effects by adding the Yukawa term, (3.24), to the effective potential,

$$V_{eff} = \frac{1}{2}\left(\frac{\Omega}{\Sigma^2} - \mu^2\right)\phi^2 + \frac{1}{4}\lambda\phi^4 + g_s\frac{M^2\Omega_e}{m_e\Sigma^2}\phi \tag{B.1}$$

where Ω_e is the fractional electron density which we take to be roughly $\Omega_e \approx 10^{-3}\Omega$. The VEV can then be calculated from

$$\nu^3 + \frac{(\Omega - \mu^2\Sigma^2)}{\lambda\Sigma^2}\left(\frac{g_s M^2}{10^3 m_e} + \nu\right) = 0. \tag{B.2}$$

In the early universe where $\Omega \gg \mu^2\Sigma^2$ (and therefore $\Omega \gg \lambda\Sigma^2$) the VEV rests at

$$\nu \approx -\frac{g_s M^2}{10^3 m_e} \tag{B.3}$$

and only deviates drastically from this near the transition point, $\Omega \approx \mu^2\Sigma^2$. On the other hand, when $\Omega \ll \mu^2\Sigma^2$ the VEV is displaced to some finite value (the details of which are not important here) but now with $sign(v) = sign(g_s)$. Therefore, the actual mechanism is messier than what was discussed in chapter 3 but remains the same in principle since there remains a difference in the VEV during recombination and today.

With the exception of its affect on parameter estimations, the only physical effects of interest that the back reaction term causes would be in the decreased formation of domain walls. Without the back reaction term, the field has equal probability of rolling towards $\pm v$ assuming the field is initially at rest at $\phi = 0$ (see 3.1). This would cause a high frequency of domain walls forming between states of $+v$ and $-v$. But with the back reaction term, the field at symmetry breaking is already pulled towards one of the VEVs (the true vacuum) while the secondary VEV (false vacuum) is formed at a higher energy (see B.1). Domain walls in this case only form when the field ϕ tunnels through the potential barrier and are therefore less likely to occur.

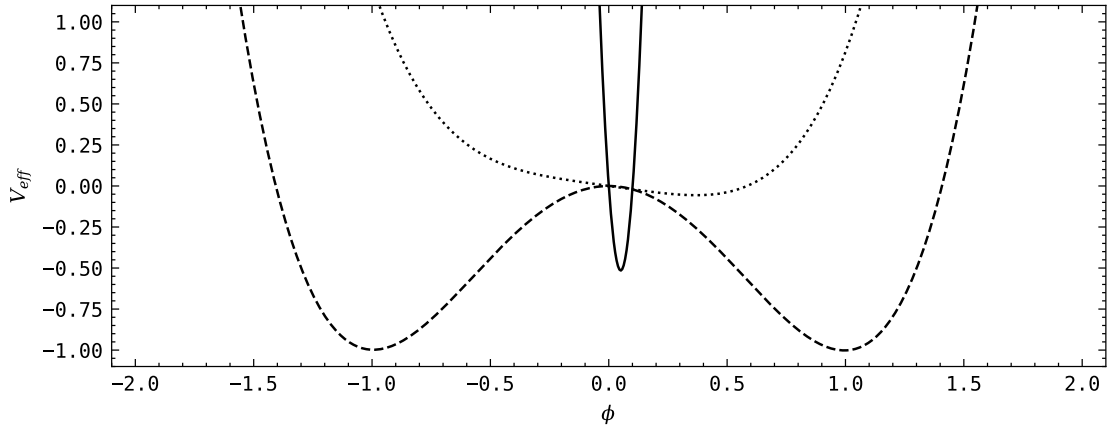

Figure B.1: The symmetron potential in arbitrary units including back reaction from the Yukawa coupling (assuming $g_s < 0$). Identical to figure 3.1, the solid, dotted, and dashed curves show the potential when $\Omega \gg \mu^2\Sigma^2$, $\Omega = \mu^2\Sigma^2$, and $\Omega \ll \mu^2\Sigma^2$, respectively. For clarity, if tracking V_{eff} through cosmic time one would see a gradual transition from the solid curve, to the dotted, and ending with the dashed.

Bibliography

[1] R. Solomon and D. Stojkovic, "Variability in quasar light curves: using quasars as standard candles," JCAP **04**, no.04, 060 (2022) doi:10.1088/1475-7516/2022/04/060 [arXiv:2110.03671 [astro-ph.CO]].

[2] E. Ó. Colgáin, M. M. Sheikh-Jabbari, R. Solomon, G. Bargiacchi, S. Capozziello, M. G. Dainotti and D. Stojkovic, "Revealing Intrinsic Flat ΛCDM Biases with Standardizable Candles," [arXiv:2203.10558 [astro-ph.CO]].

[3] E. Ó. Colgáin, M. M. Sheikh-Jabbari, R. Solomon, M. G. Dainotti and D. Stojkovic, "Putting Flat ΛCDM In The (Redshift) Bin," [arXiv:2206.11447 [astro-ph.CO]].

[4] R. Solomon, G. Agarwal and D. Stojkovic, "Environment dependent electron mass and the Hubble constant tension," Phys. Rev. D **105**, no.10, 10 (2022) doi:10.1103/PhysRevD.105.103536 [arXiv:2201.03127 [hep-ph]].

[5] R. M. Wald, "General Relativity," Chicago Univ. Pr., 1984, doi:10.7208/chicago/9780226870373.001.0001

[6] A. P. Lightman, W. H. Press, R. H. Price and S. A. Teukolsky, "Problem book in relativity and gravitation," Princeton University Press (1975)

[7] C. W. Misner, K. S. Thorne and J. A. Wheeler, "Gravitation," W. H. Freeman, 1973, ISBN 978-0-7167-0344-0, 978-0-691-17779-3

[8] J. Sola, "Cosmological constant and vacuum energy: old and new ideas," J. Phys. Conf. Ser. **453**, 012015 (2013) doi:10.1088/1742-6596/453/1/012015 [arXiv:1306.1527 [gr-qc]].

[9] N. Aghanim *et al.* [Planck], "Planck 2018 results. I. Overview and the cosmological legacy of Planck," Astron. Astrophys. **641**, A1 (2020) doi:10.1051/0004-6361/201833880 [arXiv:1807.06205 [astro-ph.CO]].

[10] J. Yoo, J. Chaname and A. Gould, "The end of the MACHO era: limits on halo dark matter from stellar halo wide binaries," Astrophys. J. **601**, 311-318 (2004) doi:10.1086/380562 [arXiv:astro-ph/0307437 [astro-ph]].

[11] N. Aghanim *et al.* [Planck], "Planck 2018 results. VI. Cosmological parameters," Astron. Astrophys. **641**, A6 (2020) [erratum: Astron. Astrophys. **652**, C4 (2021)] doi:10.1051/0004-6361/201833910 [arXiv:1807.06209 [astro-ph.CO]].

[12] A. Kashlinsky, F. Atrio-Barandela, H. Ebeling, A. Edge and D. Kocevski, "A new measurement of the bulk flow of X-ray luminous clusters of galaxies," Astrophys. J. Lett. **712**, L81-L85 (2010) doi:10.1088/2041-8205/712/1/L81 [arXiv:0910.4958 [astro-ph.CO]].

[13] A. Kashlinsky, F. Atrio-Barandela and H. Ebeling, "Measuring the dark flow with public X-ray cluster data," Astrophys. J. **732**, 1 (2011) doi:10.1088/0004-637X/732/1/1 [arXiv:1012.3214 [astro-ph.CO]].

[14] P. K. Aluri, P. Cea, P. Chingangbam, M. C. Chu, R. G. Clowes, D. Hutsemékers, J. P. Kochappan, A. Krasiński, A. M. Lopez and L. Liu, *et al.* "Is the Observable Universe Consistent with the Cosmological Principle?," [arXiv:2207.05765 [astro-ph.CO]].

[15] T. Clifton, P. G. Ferreira, A. Padilla and C. Skordis, "Modified Gravity and Cosmology," Phys. Rept. **513**, 1-189 (2012) doi:10.1016/j.physrep.2012.01.001 [arXiv:1106.2476 [astro-ph.CO]].

[16] M. Milgrom, "A modification of the Newtonian dynamics - Implications for galaxies," ApJ. **270** pp. 371-383 (1983,7)

[17] R. H. Sanders and S. S. McGaugh, "Modified Newtonian dynamics as an alternative to dark matter," Ann. Rev. Astron. Astrophys. **40**, 263-317 (2002) doi:10.1146/annurev.astro.40.060401.093923 [arXiv:astro-ph/0204521 [astro-ph]].

[18] D. C. Dai and D. Stojkovic, "Maximal temperature in a simple thermodynamical system," JCAP **06**, 040 (2016) doi:10.1088/1475-7516/2016/06/040 [arXiv:1601.07563 [gr-qc]].

[19] R. Hill, K. W. Masui and D. Scott, "The Spectrum of the Universe," Appl. Spectrosc. **72**, no.5, 663-688 (2018) doi:10.1177/0003702818767133 [arXiv:1802.03694 [astro-ph.CO]].

[20] D. J. Eisenstein *et al.* [SDSS], "Detection of the Baryon Acoustic Peak in the Large-Scale Correlation Function of SDSS Luminous Red Galaxies," Astrophys. J. **633**, 560-574 (2005) doi:10.1086/466512 [arXiv:astro-ph/0501171 [astro-ph]].

[21] J. Kovac, E. M. Leitch, C. Pryke, J. E. Carlstrom, N. W. Halverson and W. L. Holzapfel, "Detection of polarization in the cosmic microwave background using DASI," Nature **420**, 772-787 (2002) doi:10.1038/nature01269 [arXiv:astro-ph/0209478 [astro-ph]].

[22] A. G. Riess *et al.* [Supernova Search Team], "Observational evidence from supernovae for an accelerating universe and a cosmological constant," Astron. J. **116**, 1009-1038 (1998) doi:10.1086/300499 [arXiv:astro-ph/9805201 [astro-ph]].

[23] F. Bernardeau, S. Colombi, E. Gaztanaga and R. Scoccimarro, "Large scale structure of the universe and cosmological perturbation theory," Phys. Rept. **367**, 1-248 (2002) doi:10.1016/S0370-1573(02)00135-7 [arXiv:astro-ph/0112551 [astro-ph]].

[24] R. H. Cyburt, B. D. Fields, K. A. Olive and T. H. Yeh, "Big Bang Nucleosynthesis: 2015," Rev. Mod. Phys. **88**, 015004 (2016) doi:10.1103/RevModPhys.88.015004 [arXiv:1505.01076 [astro-ph.CO]].

[25] E. Di Valentino, L. A. Anchordoqui, Ö. Akarsu, Y. Ali-Haimoud, L. Amendola, N. Arendse, M. Asgari, M. Ballardini, S. Basilakos and E. Battistelli, *et al.* "Cosmology intertwined III: $f\sigma_8$ and S_8," Astropart. Phys. **131**, 102604 (2021) doi:10.1016/j.astropartphys.2021.102604 [arXiv:2008.11285 [astro-ph.CO]].

[26] L. Perivolaropoulos and F. Skara, "Challenges for ΛCDM: An update," [arXiv:2105.05208 [astro-ph.CO]].

[27] E. Abdalla, G. Franco Abellán, A. Aboubrahim, A. Agnello, O. Akarsu, Y. Akrami, G. Alestas, D. Aloni, L. Amendola and L. A. Anchordoqui, *et al.* "Cosmology intertwined: A review of the particle physics, astrophysics, and cosmology associated with the cosmological tensions and anomalies," JHEAp **34**, 49-211 (2022) doi:10.1016/j.jheap.2022.04.002 [arXiv:2203.06142 [astro-ph.CO]].

[28] A. G. Riess, W. Yuan, L. M. Macri, D. Scolnic, D. Brout, S. Casertano, D. O. Jones, Y. Murakami, L. Breuval and T. G. Brink, *et al.* "A Comprehensive Measurement of the Local Value of the Hubble Constant with 1 km/s/Mpc Uncertainty from the Hubble Space Telescope and the SH0ES Team," [arXiv:2112.04510 [astro-ph.CO]].

[29] E. Di Valentino, O. Mena, S. Pan, L. Visinelli, W. Yang, A. Melchiorri, D. F. Mota, A. G. Riess and J. Silk, "In the realm of the Hubble tension—a review of solutions," Class. Quant. Grav. **38**, no.15, 153001 (2021) doi:10.1088/1361-6382/ac086d [arXiv:2103.01183 [astro-ph.CO]].

[30] L. Balkenhol *et al.* [SPT-3G], "Constraints on ΛCDM extensions from the SPT-3G 2018 EE and TE power spectra," Phys. Rev. D **104**, no.8, 083509 (2021) doi:10.1103/PhysRevD.104.083509 [arXiv:2103.13618 [astro-ph.CO]].

[31] L. Pogosian, G. B. Zhao and K. Jedamzik, "Recombination-independent determination of the sound horizon and the Hubble constant from BAO," Astrophys. J. Lett. **904**, no.2, L17 (2020) doi:10.3847/2041-8213/abc6a8 [arXiv:2009.08455 [astro-ph.CO]].

[32] P. A. R. Ade *et al.* [Planck], "Planck 2015 results. XIII. Cosmological parameters," Astron. Astrophys. **594**, A13 (2016) doi:10.1051/0004-6361/201525830 [arXiv:1502.01589 [astro-ph.CO]].

[33] D. Dutcher *et al.* [SPT-3G], "Measurements of the E-mode polarization and temperature-E-mode correlation of the CMB from SPT-3G 2018 data," Phys. Rev. D **104**, no.2, 022003 (2021) doi:10.1103/PhysRevD.104.022003 [arXiv:2101.01684 [astro-ph.CO]].

[34] S. Aiola *et al.* [ACT], "The Atacama Cosmology Telescope: DR4 Maps and Cosmological Parameters," JCAP **12**, 047 (2020) doi:10.1088/1475-7516/2020/12/047 [arXiv:2007.07288 [astro-ph.CO]].

[35] X. Zhang and Q. G. Huang, "Constraints on H_0 from WMAP and BAO Measurements," Commun. Theor. Phys. **71**, no.7, 826-830 (2019) doi:10.1088/0253-6102/71/7/826 [arXiv:1812.01877 [astro-ph.CO]].

[36] J. W. Henning *et al.* [SPT], "Measurements of the Temperature and E-Mode Polarization of the CMB from 500 Square Degrees of SPTpol Data," Astrophys. J. **852**, no.2, 97 (2018) doi:10.3847/1538-4357/aa9ff4 [arXiv:1707.09353 [astro-ph.CO]].

[37] G. Hinshaw *et al.* [WMAP], "Nine-Year Wilkinson Microwave Anisotropy Probe (WMAP) Observations: Cosmological Parameter Results," Astrophys. J. Suppl. **208**, 19 (2013) doi:10.1088/0067-0049/208/2/19 [arXiv:1212.5226 [astro-ph.CO]].

[38] S. Alam *et al.* [eBOSS], "Completed SDSS-IV extended Baryon Oscillation Spectroscopic Survey: Cosmological implications from two decades of spectroscopic surveys at the Apache Point Observatory," Phys. Rev. D **103**, no.8, 083533 (2021) doi:10.1103/PhysRevD.103.083533 [arXiv:2007.08991 [astro-ph.CO]].

[39] O. H. E. Philcox, M. M. Ivanov, M. Simonović and M. Zaldarriaga, "Combining Full-Shape and BAO Analyses of Galaxy Power Spectra:

A 1.6\% CMB-independent constraint on H_0," JCAP **05**, 032 (2020) doi:10.1088/1475-7516/2020/05/032 [arXiv:2002.04035 [astro-ph.CO]].

[40] G. D'Amico, J. Gleyzes, N. Kokron, K. Markovic, L. Senatore, P. Zhang, F. Beutler and H. Gil-Marín, "The Cosmological Analysis of the SDSS/BOSS data from the Effective Field Theory of Large-Scale Structure," JCAP **05**, 005 (2020) doi:10.1088/1475-7516/2020/05/005 [arXiv:1909.05271 [astro-ph.CO]].

[41] M. M. Ivanov, M. Simonović and M. Zaldarriaga, "Cosmological Parameters from the BOSS Galaxy Power Spectrum," JCAP **05**, 042 (2020) doi:10.1088/1475-7516/2020/05/042 [arXiv:1909.05277 [astro-ph.CO]].

[42] T. Colas, G. D'amico, L. Senatore, P. Zhang and F. Beutler, "Efficient Cosmological Analysis of the SDSS/BOSS data from the Effective Field Theory of Large-Scale Structure," JCAP **06**, 001 (2020) doi:10.1088/1475-7516/2020/06/001 [arXiv:1909.07951 [astro-ph.CO]].

[43] O. H. E. Philcox, B. D. Sherwin, G. S. Farren and E. J. Baxter, "Determining the Hubble Constant without the Sound Horizon: Measurements from Galaxy Surveys," Phys. Rev. D **103**, no.2, 023538 (2021) doi:10.1103/PhysRevD.103.023538 [arXiv:2008.08084 [astro-ph.CO]].

[44] A. G. Riess, S. Casertano, W. Yuan, J. B. Bowers, L. Macri, J. C. Zinn and D. Scolnic, "Cosmic Distances Calibrated to 1% Precision with Gaia EDR3 Parallaxes and Hubble Space Telescope Photometry of 75 Milky Way Cepheids Confirm Tension with ΛCDM," Astrophys. J. Lett. **908**, no.1, L6 (2021) doi:10.3847/2041-8213/abdbaf [arXiv:2012.08534 [astro-ph.CO]].

[45] L. Breuval, P. Kervella, R. I. Anderson, A. G. Riess, F. Arenou, B. Trahin, A. Mérand, A. Gallenne, W. Gieren and J. Storm, *et al.* "The Milky Way Cepheid Leavitt law based on Gaia DR2 parallaxes of companion stars and host open cluster populations," Astron. Astrophys. **643**, A115 (2020) doi:10.1051/0004-6361/202038633 [arXiv:2006.08763 [astro-ph.SR]].

[46] A. G. Riess, S. Casertano, W. Yuan, L. M. Macri and D. Scolnic, "Large Magellanic Cloud Cepheid Standards Provide a 1% Foundation for the Determination of the Hubble Constant and Stronger Evidence for Physics beyond ΛCDM," Astrophys. J. **876**, no.1, 85 (2019) doi:10.3847/1538-4357/ab1422 [arXiv:1903.07603 [astro-ph.CO]].

[47] D. Camarena and V. Marra, "Local determination of the Hubble constant and the deceleration parameter," Phys. Rev. Res. **2**, no.1, 013028 (2020) doi:10.1103/PhysRevResearch.2.013028 [arXiv:1906.11814 [astro-ph.CO]].

[48] C. R. Burns *et al.* [CSP], "The Carnegie Supernova Project: Absolute Calibration and the Hubble Constant," Astrophys. J. **869**, no.1, 56 (2018) doi:10.3847/1538-4357/aae51c [arXiv:1809.06381 [astro-ph.CO]].

[49] S. Dhawan, S. W. Jha and B. Leibundgut, "Measuring the Hubble constant with Type Ia supernovae as near-infrared standard candles," Astron. Astrophys. **609**, A72 (2018) doi:10.1051/0004-6361/201731501 [arXiv:1707.00715 [astro-ph.CO]].

[50] B. Follin and L. Knox, "Insensitivity of the distance ladder Hubble constant determination to Cepheid calibration modelling choices," Mon. Not. Roy. Astron. Soc. **477**, no.4, 4534-4542 (2018) doi:10.1093/mnras/sty720 [arXiv:1707.01175 [astro-ph.CO]].

[51] S. M. Feeney, D. J. Mortlock and N. Dalmasso, "Clarifying the Hubble constant tension with a Bayesian hierarchical model of the local distance ladder," Mon. Not. Roy. Astron. Soc. **476**, no.3, 3861-3882 (2018) doi:10.1093/mnras/sty418 [arXiv:1707.00007 [astro-ph.CO]].

[52] A. G. Riess, L. M. Macri, S. L. Hoffmann, D. Scolnic, S. Casertano, A. V. Filippenko, B. E. Tucker, M. J. Reid, D. O. Jones and J. M. Silverman, *et al.* "A 2.4% Determination of the Local Value of the Hubble Constant," Astrophys. J. **826**, no.1, 56 (2016) doi:10.3847/0004-637X/826/1/56 [arXiv:1604.01424 [astro-ph.CO]].

[53] W. Cardona, M. Kunz and V. Pettorino, "Determining H_0 with Bayesian hyper-parameters," JCAP **03**, 056 (2017) doi:10.1088/1475-7516/2017/03/056 [arXiv:1611.06088 [astro-ph.CO]].

[54] W. L. Freedman, B. F. Madore, V. Scowcroft, C. Burns, A. Monson, S. E. Persson, M. Seibert and J. Rigby, "Carnegie Hubble Program: A Mid-Infrared Calibration of the Hubble Constant," Astrophys. J. **758**, 24 (2012) doi:10.1088/0004-637X/758/1/24 [arXiv:1208.3281 [astro-ph.CO]].

[55] J. Soltis, S. Casertano and A. G. Riess, "The Parallax of ω Centauri Measured from Gaia EDR3 and a Direct, Geometric Calibration of the Tip of the Red Giant Branch and the Hubble Constant," Astrophys. J. Lett. **908**, no.1, L5 (2021) doi:10.3847/2041-8213/abdbad [arXiv:2012.09196 [astro-ph.GA]].

[56] W. L. Freedman, B. F. Madore, T. Hoyt, I. S. Jang, R. Beaton, M. G. Lee, A. Monson, J. Neeley and J. Rich, "Calibration of the Tip of the Red Giant Branch (TRGB)," doi:10.3847/1538-4357/ab7339 [arXiv:2002.01550 [astro-ph.GA]].

[57] M. J. Reid, D. W. Pesce and A. G. Riess, "An Improved Distance to NGC 4258 and its Implications for the Hubble Constant," Astrophys. J. Lett. **886**, no.2, L27 (2019) doi:10.3847/2041-8213/ab552d [arXiv:1908.05625 [astro-ph.GA]].

[58] W. L. Freedman, B. F. Madore, D. Hatt, T. J. Hoyt, I. S. Jang, R. L. Beaton, C. R. Burns, M. G. Lee, A. J. Monson and J. R. Neeley, *et al.* "The Carnegie-Chicago Hubble Program. VIII. An Independent Determination of the Hubble Constant Based on the Tip of the Red Giant Branch," doi:10.3847/1538-4357/ab2f73 [arXiv:1907.05922 [astro-ph.CO]].

[59] W. Yuan, A. G. Riess, L. M. Macri, S. Casertano and D. Scolnic, "Consistent Calibration of the Tip of the Red Giant Branch in the Large Magellanic Cloud on the Hubble Space Telescope Photometric System and a Re-determination of the Hubble Constant," Astrophys. J. **886**, 61 (2019) doi:10.3847/1538-4357/ab4bc9 [arXiv:1908.00993 [astro-ph.GA]].

[60] I. S. Jang and M. G. Lee, "The Tip of the Red Giant Branch Distances to Typa Ia Supernova Host Galaxies. V. NGC 3021, NGC 3370, and NGC 1309 and the Value of the Hubble Constant," Astrophys. J. **836**, no.1, 74 (2017) doi:10.3847/1538-4357/836/1/74 [arXiv:1702.01118 [astro-ph.CO]].

[61] C. D. Huang, A. G. Riess, W. Yuan, L. M. Macri, N. L. Zakamska, S. Casertano, P. A. Whitelock, S. L. Hoffmann, A. V. Filippenko and D. Scolnic, "Hubble Space Telescope Observations of Mira Variables in the Type Ia Supernova Host NGC 1559: An Alternative Candle to Measure the Hubble Constant," doi:10.3847/1538-4357/ab5dbd [arXiv:1908.10883 [astro-ph.CO]].

[62] D. W. Pesce, J. A. Braatz, M. J. Reid, A. G. Riess, D. Scolnic, J. J. Condon, F. Gao, C. Henkel, C. M. V. Impellizzeri and C. Y. Kuo, *et al.* "The Megamaser Cosmology Project. XIII. Combined Hubble constant constraints," Astrophys. J. Lett. **891**, no.1, L1 (2020) doi:10.3847/2041-8213/ab75f0 [arXiv:2001.09213 [astro-ph.CO]].

[63] E. Kourkchi, R. B. Tully, G. S. Anand, H. M. Courtois, A. Dupuy, J. D. Neill, L. Rizzi and M. Seibert, "Cosmicflows-4: The Calibration of Optical and Infrared Tully–Fisher Relations," Astrophys. J. **896**, no.1, 3 (2020) doi:10.3847/1538-4357/ab901c [arXiv:2004.14499 [astro-ph.GA]].

[64] J. Schombert, S. McGaugh and F. Lelli, "Using the Baryonic Tully–Fisher Relation to Measure H o," Astron. J. **160**, no.2, 71 (2020) doi:10.3847/1538-3881/ab9d88 [arXiv:2006.08615 [astro-ph.CO]].

[65] J. P. Blakeslee, J. B. Jensen, C. P. Ma, P. A. Milne and J. E. Greene, "The Hubble Constant from Infrared Surface Brightness Fluctuation Distances," Astrophys. J. **911**, no.1, 65 (2021) doi:10.3847/1538-4357/abe86a [arXiv:2101.02221 [astro-ph.CO]].

[66] N. Khetan, L. Izzo, M. Branchesi, R. Wojtak, M. Cantiello, C. Murugeshan, A. Agnello, M. Della Valle, C. Gall and J. Hjorth, *et al.* "A new measurement of the Hubble constant using Type Ia supernovae calibrated with surface brightness fluctuations," Astron. Astrophys. **647**, A72 (2021) doi:10.1051/0004-6361/202039196 [arXiv:2008.07754 [astro-ph.CO]].

[67] T. de Jaeger, B. E. Stahl, W. Zheng, A. V. Filippenko, A. G. Riess and L. Galbany, "A measurement of the Hubble constant from Type II supernovae," Mon. Not. Roy. Astron. Soc. **496**, no.3, 3402-3411 (2020) doi:10.1093/mnras/staa1801 [arXiv:2006.03412 [astro-ph.CO]].

[68] D. Fernández Arenas, E. Terlevich, R. Terlevich, J. Melnick, R. Chávez, F. Bresolin, E. Telles, M. Plionis and S. Basilakos, "An independent determination of the local Hubble constant," Mon. Not. Roy. Astron. Soc. **474**, no.1, 1250-1276 (2018) doi:10.1093/mnras/stx2710 [arXiv:1710.05951 [astro-ph.CO]].

[69] J. Z. Qi, J. W. Zhao, S. Cao, M. Biesiada and Y. Liu, "Measurements of the Hubble constant and cosmic curvature with quasars: ultracompact radio structure and strong gravitational lensing," Mon. Not. Roy. Astron. Soc. **503**, no.2, 2179-2186 (2021) doi:10.1093/mnras/stab638 [arXiv:2011.00713 [astro-ph.CO]].

[70] P. Denzel, J. P. Coles, P. Saha and L. L. R. Williams, "The Hubble constant from eight time-delay galaxy lenses," Mon. Not. Roy. Astron. Soc. **501**, no.1, 784-801 (2021) doi:10.1093/mnras/staa3603 [arXiv:2007.14398 [astro-ph.CO]].

[71] S. Birrer, A. J. Shajib, A. Galan, M. Millon, T. Treu, A. Agnello, M. Auger, G. C. F. Chen, L. Christensen and T. Collett, *et al.* "TDCOSMO - IV. Hierarchical time-delay cosmography – joint inference of the Hubble constant and galaxy density profiles," Astron. Astrophys. **643**, A165 (2020) doi:10.1051/0004-6361/202038861 [arXiv:2007.02941 [astro-ph.CO]].

[72] E. J. Baxter and B. D. Sherwin, "Determining the Hubble Constant without the Sound Horizon Scale: Measurements from CMB Lensing," Mon. Not. Roy. Astron. Soc. **501**, no.2, 1823-1835 (2021) doi:10.1093/mnras/staa3706 [arXiv:2007.04007 [astro-ph.CO]].

[73] T. Yang, S. Birrer and B. Hu, "The first simultaneous measurement of Hubble constant and post-Newtonian parameter from Time-Delay Strong Lensing," Mon. Not. Roy. Astron. Soc. **497**, no.1, L56-L61 (2020) doi:10.1093/mnrasl/slaa107 [arXiv:2003.03277 [astro-ph.CO]].

[74] K. Liao, A. Shafieloo, R. E. Keeley and E. V. Linder, "Determining Model-independent H 0 and Consistency Tests," Astrophys. J. Lett. **895**, no.2, L29 (2020) doi:10.3847/2041-8213/ab8dbb [arXiv:2002.10605 [astro-ph.CO]].

[75] M. Millon, A. Galan, F. Courbin, T. Treu, S. H. Suyu, X. Ding, S. Birrer, G. C. F. Chen, A. J. Shajib and D. Sluse, *et al.* "TDCOSMO. I. An exploration of systematic uncertainties in the inference of H_0 from time-delay cosmography," Astron. Astrophys. **639**, A101 (2020) doi:10.1051/0004-6361/201937351 [arXiv:1912.08027 [astro-ph.CO]].

[76] A. J. Shajib *et al.* [DES], "STRIDES: a 3.9 per cent measurement of the Hubble constant from the strong lens system DES J0408−5354," Mon. Not. Roy. Astron. Soc. **494**, no.4, 6072-6102 (2020) doi:10.1093/mnras/staa828 [arXiv:1910.06306 [astro-ph.CO]].

[77] S. Birrer, T. Treu, C. E. Rusu, V. Bonvin, C. D. Fassnacht, J. H. H. Chan, A. Agnello, A. J. Shajib, G. C. F. Chen and M. Auger, *et al.* "H0LiCOW - IX. Cosmographic analysis of the doubly imaged quasar SDSS 1206+4332 and a new measurement of the Hubble constant," Mon. Not. Roy. Astron. Soc. **484**, 4726 (2019) doi:10.1093/mnras/stz200 [arXiv:1809.01274 [astro-ph.CO]].

[78] K. Liao, A. Shafieloo, R. E. Keeley and E. V. Linder, "A model-independent determination of the Hubble constant from lensed quasars and supernovae using Gaussian process regression," Astrophys. J. Lett. **886**, no.1, L23 (2019) doi:10.3847/2041-8213/ab5308 [arXiv:1908.04967 [astro-ph.CO]].

[79] K. C. Wong, S. H. Suyu, G. C. F. Chen, C. E. Rusu, M. Millon, D. Sluse, V. Bonvin, C. D. Fassnacht, S. Taubenberger and M. W. Auger, *et al.* "H0LiCOW – XIII. A 2.4 per cent measurement of H0 from lensed quasars: 5.3σ tension between early- and late-Universe probes," Mon. Not. Roy. Astron. Soc. **498**, no.1, 1420-1439 (2020) doi:10.1093/mnras/stz3094 [arXiv:1907.04869 [astro-ph.CO]].

[80] V. Bonvin, F. Courbin, S. H. Suyu, P. J. Marshall, C. E. Rusu, D. Sluse, M. Tewes, K. C. Wong, T. Collett and C. D. Fassnacht, *et al.* "H0LiCOW – V. New COSMOGRAIL time delays of HE 0435−1223: H_0 to 3.8 per cent precision from strong lensing in a flat ΛCDM model," Mon. Not. Roy. Astron. Soc. **465**, no.4, 4914-4930 (2017) doi:10.1093/mnras/stw3006 [arXiv:1607.01790 [astro-ph.CO]].

[81] E. Di Valentino, "A combined analysis of the H_0 late time direct measurements and the impact on the Dark Energy sector," Mon. Not. Roy. Astron. Soc. **502**, no.2, 2065-2073 (2021) doi:10.1093/mnras/stab187 [arXiv:2011.00246 [astro-ph.CO]].

[82] V. Gayathri, J. Healy, J. Lange, B. O'Brien, M. Szczepanczyk, I. Bartos, M. Campanelli, S. Klimenko, C. O. Lousto and R. O'Shaughnessy, "Measuring the Hubble Constant with GW190521 as an Eccentric black hole Merger and Its Potential Electromagnetic Counterpart," Astrophys. J. Lett. **908**, no.2, L34 (2021) doi:10.3847/2041-8213/abe388 [arXiv:2009.14247 [astro-ph.HE]].

[83] S. Mukherjee, A. Ghosh, M. J. Graham, C. Karathanasis, M. M. Kasliwal, I. Magaña Hernandez, S. M. Nissanke, A. Silvestri and B. D. Wandelt, "First measurement of the Hubble parameter from bright binary black hole GW190521," [arXiv:2009.14199 [astro-ph.CO]].

[84] S. Mukherjee, G. Lavaux, F. R. Bouchet, J. Jasche, B. D. Wandelt, S. M. Nissanke, F. Leclercq and K. Hotokezaka, "Velocity correction for Hubble constant measurements from standard sirens," Astron. Astrophys. **646**, A65 (2021) doi:10.1051/0004-6361/201936724 [arXiv:1909.08627 [astro-ph.CO]].

[85] B. P. Abbott *et al.* [LIGO Scientific, Virgo, 1M2H, Dark Energy Camera GW-E, DES, DLT40, Las Cumbres Observatory, VINROUGE and MASTER], "A gravitational-wave standard siren measurement of the Hubble constant," Nature **551**, no.7678, 85-88 (2017) doi:10.1038/nature24471 [arXiv:1710.05835 [astro-ph.CO]].

[86] N. Schöneberg, G. Franco Abellán, A. Pérez Sánchez, S. J. Witte, V. Poulin and J. Lesgourgues, "The H_0 Olympics: A fair ranking of proposed models," [arXiv:2107.10291 [astro-ph.CO]].

[87] T. Sekiguchi and T. Takahashi, "Early recombination as a solution to the H_0 tension," Phys. Rev. D **103**, no.8, 083507 (2021) doi:10.1103/PhysRevD.103.083507 [arXiv:2007.03381 [astro-ph.CO]].

[88] D. M. Scolnic *et al.* [Pan-STARRS1], "The Complete Light-curve Sample of Spectroscopically Confirmed SNe Ia from Pan-STARRS1 and Cosmological Constraints from the Combined Pantheon Sample," Astrophys. J. **859**, no.2, 101 (2018) doi:10.3847/1538-4357/aab9bb [arXiv:1710.00845 [astro-ph.CO]].

[89] E. Hubble, "A relation between distance and radial velocity among extra-galactic nebulae," Proc. Nat. Acad. Sci. **15**, 168-173 (1929) doi:10.1073/pnas.15.3.168

[90] L. Lindegren, J. Hernandez, A. Bombrun, S. Klioner, U. Bastian, M. Ramos-Lerate, A. de Torres, H. Steidelmuller, C. Stephenson and D. Hobbs, *et al.* "Gaia Data Release 2: The astrometric solution," Astron. Astrophys. **616**, A2 (2018) doi:10.1051/0004-6361/201832727 [arXiv:1804.09366 [astro-ph.IM]].

[91] B. Nicolet "Catalogue of homogeneous data in the UBV photoelectric photometric system," ApJ. **34** pp. 1-49 (1978,10)

[92] D. Lambert, J. Brown, K. Hinkle, and H. Johnson "Carbon, nitrogen and oxygem abundances in Betelgeuse," ApJ. **284** pp. 223-237 (1984,9)

[93] P. Pietrukowicz, W. Dziembowski, P. Mróz, I. Soszyński, A. Udalski, R. Poleski, M. Szymański, M. Kubiak, G. Pietrzyński and L. Wyrzykowski, *et al.* "Large Variety of New Pulsating Stars in the OGLE-III Galactic Disk Fields," Acta Astronautica **63**, 379-404 (2013,12

[94] M. W. Feast and R. M. Catchpole, "The Cepheid period-luminosity zero-point from HIPPARCOS trigonometrical parallaxes," Mon. Not. Roy. Astron. Soc. **286**, L1-L5 (1997) doi:10.1093/mnras/286.1.L1

[95] J. Frogel, J. Cohen and S. Persson, "Globular cluster giant branches and the metallicity scale," Astrophys. J **275** pp. 773-789 (1983,12)

[96] T. J. Hoyt, "On Zero Point Calibration of the Red Giant Branch Tip in the Magellanic Clouds," [arXiv:2106.13337 [astro-ph.GA]].

[97] J. Bloom, D. Kasen, K. Shen, P. Nugent, N. Butler, M. Graham, D. Howell, U. Kolb, S. Holmes, C. Haswell, V. Burwitz, J. Rodriguez and M. Sullivan, "A Compact Degenerate Primary-star Progenitor of SN 2011fe," Astrophys. J. **744**, eL17 (2012,1)

[98] S. Colgate and C. McKee, "Early Supernova Luminosity," Astophys. J. **157** pp. 623 (1969,8)

[99] M. Phillips "The Absolute Magnitudes of Type IA Supernovae," ApJ. **413** pp. L105 (1993,8)

[100] D. Brout, D. Scolnic, B. Popovic, A. G. Riess, J. Zuntz, R. Kessler, A. Carr, T. M. Davis, S. Hinton and D. Jones, *et al.* "The Pantheon+ Analysis: Cosmological Constraints," [arXiv:2202.04077 [astro-ph.CO]].

[101] E. W. Kolb and M. S. Turner, "The Early Universe," Front. Phys. **69**, 1-547 (1990) doi:10.1201/9780429492860

[102] C. Armendariz-Picon, T. Damour and V. F. Mukhanov, "k - inflation," Phys. Lett. B **458**, 209-218 (1999) doi:10.1016/S0370-2693(99)00603-6 [arXiv:hep-th/9904075 [hep-th]].

[103] M. Schmidt "The Distances to the Quasars," Quarterly Journal of the Roy. Astron. Soc. **13** pp. 297 (1972,6)

[104] R. J. A. Lambourne, "Relativity, gravitation and cosmology,"

[105] M. Hawkins and P. Veron "The space density of quasars at z¿4," Mon. Not. Roy. Astron. Soc. **281**, 348-356 (1996,7)

[106] S. Collier, K. Horne, I. Wanders and B. M. Peterson, "A new direct method for measuring the hubble constant from reverberating accretion discs in active galaxies," Mon. Not. Roy. Astron. Soc. **302**, 24 (1999) doi:10.1046/j.1365-8711.1999.02250.x [arXiv:astro-ph/9811278 [astro-ph]].

[107] M. Elvis and M. Karovska, "Quasar parallax: A Method for determining direct geometrical distances to quasars," Astrophys. J. Lett. **581**, L67-L70 (2002) doi:10.1086/346015 [arXiv:astro-ph/0211385 [astro-ph]].

[108] S. Bisogni, G. Risaliti and E. Lusso, "A Hubble diagram for quasars," [arXiv:1712.07515 [astro-ph.GA]].

[109] G. Risaliti and E. Lusso, "Cosmology with AGN: can we use quasars as standard candles?," Astron. Nachr. **338**, no.2/3, 329-333 (2017) doi:10.1002/asna.201713351 [arXiv:1612.02838 [astro-ph.CO]].

[110] E. Lusso and G. Risaliti, "Quasars as standard candles I: The physical relation between disc and coronal emission," Astron. Astrophys. **602**, A79 (2017) doi:10.1051/0004-6361/201630079 [arXiv:1703.05299 [astro-ph.HE]].

[111] F. Salvestrini, G. Risaliti, S. Bisogni, E. Lusso and C. Vignali, "Quasars as standard candles II: The non linear relation between UV and X-ray emission at high redshifts," Astron. Astrophys. **631**, A120 (2019) doi:10.1051/0004-6361/201935491 [arXiv:1909.12309 [astro-ph.GA]].

[112] E. Lusso, G. Risaliti, E. Nardini, G. Bargiacchi, M. Benetti, S. Bisogni, S. Capozziello, F. Civano, L. Eggleston and M. Elvis, *et al.* "Quasars as standard candles III. Validation of a new sample for cosmological studies," Astron. Astrophys. **642**, A150 (2020) doi:10.1051/0004-6361/202038899 [arXiv:2008.08586 [astro-ph.GA]].

[113] D. Dultzin, P. Marziani, J. A. de Diego, C. A. Negrete, A. Del Olmo, M. L. Martínez-Aldama, M. D'Onofrio, E. Bon, N. Bon and G. M. Stirpe, "Extreme quasars as distance indicators in cosmology," Front. Astron.

Space Sci. **6**, 80 (2020) doi:10.3389/fspas.2019.00080 [arXiv:2001.10368 [astro-ph.CO]].

[114] K. Korista, J. Baldwin and G. Ferland, "Quasars as cosmological probes: the ionizing continuum, gas metallicity and the ew-l relation," Astrophys. J. **507**, 24 (1998) doi:10.1086/306321 [arXiv:astro-ph/9805338 [astro-ph]].

[115] F. La Franca, S. Bianchi, G. Ponti, E. Branchini and G. Matt, "A New Cosmological Distance Measure Using Active Galactic Nucleus X-Ray Variability," Astrophys. J. Lett. **787**, L12 (2014) doi:10.1088/2041-8205/787/1/L12 [arXiv:1404.2607 [astro-ph.CO]].

[116] M. Geha *et al.* [MACHO], "Variability - selected quasars in MACHO project Magellanic Cloud fields," Astron. J. **125**, 1 (2003) doi:10.1086/344947 [arXiv:astro-ph/0209513 [astro-ph]].

[117] S. Kozłowski *et al.* [OGLE], "The Magellanic Quasars Survey. III. Spectroscopic Confirmation of 758 Active Galactic Nuclei behind the Magellanic Clouds," Astrophys. J. **775**, 92 (2013) doi:10.1088/0004-637X/775/2/92 [arXiv:1305.6927 [astro-ph.CO]].

[118] L. Wisotzki "Quasar spectra and the K correction," Astronomy and Astrophysics **353**, 861-866 (2000)

[119] D. C. Dai, G. D. Starkman, B. Stojkovic, D. Stojkovic and A. Weltman, "Using quasars as standard clocks for measuring cosmological redshift," Phys. Rev. Lett. **108**, 231302 (2012) doi:10.1103/PhysRevLett.108.231302 [arXiv:1204.5191 [astro-ph.CO]].

[120] C. L. MacLeod, Ž. Ivezić, B. Sesar, W. de Vries, C. S. Kochanek, B. C. Kelly, A. C. Becker, R. H. Lupton, P. B. Hall and G. T. Richards, *et al.*, "A Description of Quasar Variability Measured Using Repeated SDSS and POSS Imaging," ApJ **753**, 106 (2012) doi:10.1088/0004-637X/753/2/106 [arXiv:1112.0679 [astro-ph.CO]].

[121] B. C. Kelly, J. Bechtold and A. Siemiginowska, "Are the Variations in Quasar Optical Flux Driven by Thermal Fluctuations?," ApJ **698**, no.1, 895-910, (2009) doi:10.1088/0004-637X/698/1/895, [arXiv:0903.5315 [astro-ph.CO]]. https://ui.adsabs.harvard.edu/abs/2009ApJ...698..895K

[122] C. L. Macleod, Ž. Ivezić, C. S. Kochanek, S. Kozłowski, B. Kelly, E. Bullock, A. Kimball, B. Sesar, D. Westman and K. Brooks, *et al.*, "Modeling the time variability of SDSS stripe 82 quasars as a damped random walk," Astrophys. J. **721**, no.2, 1014 (2010) doi:10.1088/0004-637X/721/2/1014 [arXiv:1004.0276 [astro-ph.CO]].

[123] J. VanderPlas, A. J. Connolly, Z. Ivezic and A. Gray, "Introduction to astroML: Machine learning for astrophysics," Proceedings of Conference on Intelligent Data Understanding (CIDU), 47-54 (2012) doi10.1109/CIDU.2012.6382200 [arXiv:1411.5039 [astro-ph.IM]].

[124] A. Aghamousa *et al.* [DESI], "The DESI Experiment Part I: Science,Targeting, and Survey Design," [arXiv:1611.00036 [astro-ph.IM]].

[125] A. Lewis and A. Challinor, "Weak gravitational lensing of the CMB," Phys. Rept. **429**, 1-65 (2006) doi:10.1016/j.physrep.2006.03.002 [arXiv:astro-ph/0601594 [astro-ph]].

[126] E. Di Valentino, A. Melchiorri and J. Silk, "Cosmological hints of modified gravity?," Phys. Rev. D **93**, no.2, 023513 (2016) doi:10.1103/PhysRevD.93.023513 [arXiv:1509.07501 [astro-ph.CO]].

[127] J. Ooba, B. Ratra and N. Sugiyama, "Planck 2015 Constraints on the Non-flat ΛCDM Inflation Model," Astrophys. J. **864**, no.1, 80 (2018) doi:10.3847/1538-4357/aad633 [arXiv:1707.03452 [astro-ph.CO]].

[128] G. Cabass, E. Di Valentino, A. Melchiorri, E. Pajer and J. Silk, "Constraints on the running of the running of the scalar tilt from CMB anisotropies and spectral distortions," Phys. Rev. D **94**, no.2, 023523 (2016) doi:10.1103/PhysRevD.94.023523 [arXiv:1605.00209 [astro-ph.CO]].

[129] M. Rigault, G. Aldering, M. Kowalski, Y. Copin, P. Antilogus, C. Aragon, S. Bailey, C. Baltay, D. Baugh and S. Bongard, *et al.* "Confirmation of a Star Formation Bias in Type Ia Supernova Distances and its Effect on Measurement of the Hubble Constant," Astrophys. J. **802**, no.1, 20 (2015) doi:10.1088/0004-637X/802/1/20 [arXiv:1412.6501 [astro-ph.CO]].

[130] M. Rigault *et al.* [Nearby Supernova Factory], "Strong Dependence of Type Ia Supernova Standardization on the Local Specific Star Formation Rate," Astron. Astrophys. **644**, A176 (2020) doi:10.1051/0004-6361/201730404 [arXiv:1806.03849 [astro-ph.CO]].

[131] N. Nicolas, M. Rigault, Y. Copin, R. Graziani, G. Aldering, M. Briday, Y. L. Kim, J. Nordin, S. Perlmutter and M. Smith, "Redshift evolution of the underlying type Ia supernova stretch distribution," Astron. Astrophys. **649**, A74 (2021) doi:10.1051/0004-6361/202038447 [arXiv:2005.09441 [astro-ph.CO]].

[132] D. O. Jones, A. G. Riess, D. M. Scolnic, Y. C. Pan, E. Johnson, D. A. Coulter, K. G. Dettman, M. M. Foley, R. J. Foley and M. E. Huber, *et al.*

"Should Type Ia Supernova Distances be Corrected for their Local Environments?," Astrophys. J. **867**, no.2, 108 (2018) doi:10.3847/1538-4357/aae2b9 [arXiv:1805.05911 [astro-ph.CO]].

[133] L. Hart and J. Chluba, "New constraints on time-dependent variations of fundamental constants using Planck data," Mon. Not. Roy. Astron. Soc. **474**, no.2, 1850-1861 (2018) doi:10.1093/mnras/stx2783 [arXiv:1705.03925 [astro-ph.CO]].

[134] M. Kaplinghat, R. J. Scherrer and M. S. Turner, "Constraining variations in the fine structure constant with the cosmic microwave background," Phys. Rev. D **60**, 023516 (1999) doi:10.1103/PhysRevD.60.023516 [arXiv:astro-ph/9810133 [astro-ph]].

[135] P. P. Avelino, C. J. A. P. Martins, G. Rocha and P. T. P. Viana, "Looking for a varying alpha in the cosmic microwave background," Phys. Rev. D **62**, 123508 (2000) doi:10.1103/PhysRevD.62.123508 [arXiv:astro-ph/0008446 [astro-ph]].

[136] R. A. Battye, R. Crittenden and J. Weller, "Cosmic concordance and the fine structure constant," Phys. Rev. D **63**, 043505 (2001) doi:10.1103/PhysRevD.63.043505 [arXiv:astro-ph/0008265 [astro-ph]].

[137] P. P. Avelino, S. Esposito, G. Mangano, C. J. A. P. Martins, A. Melchiorri, G. Miele, O. Pisanti, G. Rocha and P. T. P. Viana, "Early universe constraints on a time varying fine structure constant," Phys. Rev. D **64**, 103505 (2001) doi:10.1103/PhysRevD.64.103505 [arXiv:astro-ph/0102144 [astro-ph]].

[138] G. Rocha, R. Trotta, C. J. A. P. Martins, A. Melchiorri, P. P. Avelino, R. Bean and P. T. P. Viana, "Measuring alpha in the early universe: cmb polarization, reionization and the fisher matrix analysis," Mon. Not. Roy. Astron. Soc. **352**, 20 (2004) doi:10.1111/j.1365-2966.2004.07832.x [arXiv:astro-ph/0309211 [astro-ph]].

[139] C. J. A. P. Martins, A. Melchiorri, G. Rocha, R. Trotta, P. P. Avelino and P. T. P. Viana, "Wmap constraints on varying alpha and the promise of reionization," Phys. Lett. B **585**, 29-34 (2004) doi:10.1016/j.physletb.2003.11.080 [arXiv:astro-ph/0302295 [astro-ph]].

[140] C. G. Scoccola, S. J. Landau and H. Vucetich, "WMAP 5-year constraints on α and m_e," Mem. Soc. Ast. It. **80**, no.4, 814-819 (2009) doi:10.1017/S1743921310009476 [arXiv:0910.1083 [astro-ph.CO]].

[141] E. Menegoni, M. Archidiacono, E. Calabrese, S. Galli, C. J. A. P. Martins and A. Melchiorri, "The Fine Structure Constant and the CMB Damping

Scale," Phys. Rev. D **85**, 107301 (2012) doi:10.1103/PhysRevD.85.107301 [arXiv:1202.1476 [astro-ph.CO]].

[142] L. Hart and J. Chluba, "Updated fundamental constant constraints from Planck 2018 data and possible relations to the Hubble tension," Mon. Not. Roy. Astron. Soc. **493**, no.3, 3255-3263 (2020) doi:10.1093/mnras/staa412 [arXiv:1912.03986 [astro-ph.CO]].

[143] H. Terazawa, "Cosmological Origin of Mass Scales," Phys. Lett. B **101**, 43-47 (1981) doi:10.1016/0370-2693(81)90485-8

[144] K. A. Olive and M. Pospelov, "Environmental dependence of masses and coupling constants," Phys. Rev. D **77**, 043524 (2008) doi:10.1103/PhysRevD.77.043524 [arXiv:0709.3825 [hep-ph]].

[145] L. W. Fung, L. Li, T. Liu, H. N. Luu, Y. C. Qiu and S. H. H. Tye, "The Hubble Constant in the Axi-Higgs Universe," [arXiv:2105.01631 [astro-ph.CO]].

[146] S. Alam *et al.* [BOSS], "The clustering of galaxies in the completed SDSS-III Baryon Oscillation Spectroscopic Survey: cosmological analysis of the DR12 galaxy sample," Mon. Not. Roy. Astron. Soc. **470**, no.3, 2617-2652 (2017) doi:10.1093/mnras/stx721 [arXiv:1607.03155 [astro-ph.CO]].

[147] P. Zarrouk, E. Burtin, H. Gil-Marin, A. J. Ross, R. Tojeiro, I. Pâris, K. S. Dawson, A. D. Myers, W. J. Percival and C. H. Chuang, *et al.* "The clustering of the SDSS-IV extended Baryon Oscillation Spectroscopic Survey DR14 quasar sample: measurement of the growth rate of structure from the anisotropic correlation function between redshift 0.8 and 2.2," Mon. Not. Roy. Astron. Soc. **477**, no.2, 1639-1663 (2018) doi:10.1093/mnras/sty506 [arXiv:1801.03062 [astro-ph.CO]].

[148] J. E. Bautista, N. G. Busca, J. Guy, J. Rich, M. Blomqvist, H. d. Bourboux, M. M. Pieri, A. Font-Ribera, S. Bailey and T. Delubac, *et al.* "Measurement of baryon acoustic oscillation correlations at $z = 2.3$ with SDSS DR12 Lyα-Forests," Astron. Astrophys. **603**, A12 (2017) doi:10.1051/0004-6361/201730533 [arXiv:1702.00176 [astro-ph.CO]].

[149] H. Desmond, B. Jain and J. Sakstein, "Local resolution of the Hubble tension: The impact of screened fifth forces on the cosmic distance ladder," Phys. Rev. D **100**, no.4, 043537 (2019) [erratum: Phys. Rev. D **101**, no.6, 069904 (2020); erratum: Phys. Rev. D **101**, no.12, 129901 (2020)] doi:10.1103/PhysRevD.100.043537 [arXiv:1907.03778 [astro-ph.CO]].

[150] A. I. Vainshtein, "To the problem of nonvanishing gravitation mass," Phys. Lett. B **39**, 393-394 (1972) doi:10.1016/0370-2693(72)90147-5

[151] J. Khoury and A. Weltman, "Chameleon cosmology," Phys. Rev. D **69**, 044026 (2004) doi:10.1103/PhysRevD.69.044026 [arXiv:astro-ph/0309411 [astro-ph]].

[152] K. Hinterbichler and J. Khoury, "Symmetron Fields: Screening Long-Range Forces Through Local Symmetry Restoration," Phys. Rev. Lett. **104**, 231301 (2010) doi:10.1103/PhysRevLett.104.231301 [arXiv:1001.4525 [hep-th]].

[153] K. Hinterbichler, J. Khoury, A. Levy and A. Matas, "Symmetron Cosmology," Phys. Rev. D **84**, 103521 (2011) doi:10.1103/PhysRevD.84.103521 [arXiv:1107.2112 [astro-ph.CO]].

[154] K. Hinterbichler, J. Khoury and H. Nastase, "Towards a UV Completion for Chameleon Scalar Theories," JHEP **03**, 061 (2011) [erratum: JHEP **06**, 072 (2011)] doi:10.1007/JHEP06(2011)072 [arXiv:1012.4462 [hep-th]].

[155] R. Dong, W. H. Kinney and D. Stojkovic, "Symmetron Inflation," JCAP **01**, 021 (2014) doi:10.1088/1475-7516/2014/01/021 [arXiv:1307.4451 [astro-ph.CO]].

[156] H. Lin, and X. Li, "The dark matter profiles in the Milky Way," Mon. Not. Roy. Astron. Soc. **487**, no.4, 5679-5684 (2019) doi:10.1093/mnras/stz1698 [arXiv:1906.08419 [astro-ph.GA]].

[157] C. Burrage and J. Sakstein, "Tests of Chameleon Gravity," Living Rev. Rel. **21**, no.1, 1 (2018) doi:10.1007/s41114-018-0011-x [arXiv:1709.09071 [astro-ph.CO]].

[158] P. Brax, S. Casas, H. Desmond and B. Elder, "Testing Screened Modified Gravity," Universe **8**, no.1, 11 (2021) doi:10.3390/universe8010011 [arXiv:2201.10817 [gr-qc]].

[159] D. d'Enterria, A. Poldaru and G. Wojcik, "Measuring the electron Yukawa coupling via resonant s-channel Higgs production at FCC-ee," [arXiv:2107.02686 [hep-ex]].

[160] W. C. Lin and R. M. Solomon, "Generalizing the swampland: Embedding $P(X, \varphi)$ inflationary theories in a curved multifield space," Phys. Rev. D **103**, no.6, 063533 (2021) doi:10.1103/PhysRevD.103.063533 [arXiv:2101.00497 [hep-th]].

[161] N. Arkani-Hamed, L. Motl, A. Nicolis and C. Vafa, "The String landscape, black holes and gravity as the weakest force," JHEP **06**, 060 (2007) doi:10.1088/1126-6708/2007/06/060 [arXiv:hep-th/0601001 [hep-th]].

[162] D. C. Dai, K. Freese and D. Stojkovic, "Constraints on dark matter particles charged under a hidden gauge group from primordial black holes," JCAP **0906**, 023 (2009) doi:10.1088/1475-7516/2009/06/023 [arXiv:0904.3331 [hep-ph]].

[163] S. Hod, "A proof of the weak gravity conjecture," Int. J. Mod. Phys. D **26**, no.12, 1742004 (2017) doi:10.1142/S0218271817420044 [arXiv:1705.06287 [gr-qc]].

[164] R. Solomon and D. Stojkovic, "Generalizing weak gravity conjecture," Phys. Rev. D **102**, no.4, 4 (2020) doi:10.1103/PhysRevD.102.046016 [arXiv:2008.03749 [gr-qc]].

[165] C. Cheung and G. N. Remmen, "Naturalness and the Weak Gravity Conjecture," Phys. Rev. Lett. **113**, 051601 (2014) doi:10.1103/PhysRevLett.113.051601 [arXiv:1402.2287 [hep-ph]].

[166] Y. Kats, L. Motl and M. Padi, "Higher-order corrections to mass-charge relation of extremal black holes," JHEP **0712**, 068 (2007) doi:10.1088/1126-6708/2007/12/068 [hep-th/0606100].

[167] Y. Hamada, T. Noumi and G. Shiu, "Weak Gravity Conjecture from Unitarity and Causality," Phys. Rev. Lett. **123**, no.5, 051601 (2019) doi:10.1103/PhysRevLett.123.051601 [arXiv:1810.03637 [hep-th]].

[168] G. Goon and R. Penco, "Universal Relation between Corrections to Entropy and Extremality," Phys. Rev. Lett. **124**, no.10, 101103 (2020) doi:10.1103/PhysRevLett.124.101103 [arXiv:1909.05254 [hep-th]].

[169] C. Cheung, J. Liu and G. N. Remmen, "Entropy Bounds on Effective Field Theory from Rotating Dyonic Black Holes," Phys. Rev. D **100**, no.4, 046003 (2019) doi:10.1103/PhysRevD.100.046003 [arXiv:1903.09156 [hep-th]].

[170] B. Bellazzini, M. Lewandowski and J. Serra, "Positivity of Amplitudes, Weak Gravity Conjecture, and Modified Gravity," Phys. Rev. Lett. **123**, no.25, 251103 (2019) doi:10.1103/PhysRevLett.123.251103 [arXiv:1902.03250 [hep-th]].

[171] M. Mirbabayi, "A Weak Gravity Theorem," [arXiv:1905.02736 [hep-th]].

[172] D. N. Page, "Particle Emission Rates from a Black Hole: Massless Particles from an Uncharged, Nonrotating Hole," Phys. Rev. D **13**, 198-206 (1976) doi:10.1103/PhysRevD.13.198

[173] E. Poisson, "A Relativist's Toolkit: The Mathematics of Black-Hole Mechanics," doi:10.1017/CBO9780511606601

[174] M. Heusler, C. Kiefer and N. Straumann, "The self energy of a thin charged shell in general relativity," Phys. Rev. D **42**, 4254 (1990) doi:10.1103/PhysRevD.42.4254

[175] D. C. Dai and D. Stojkovic, "Pre-Hawking radiation may allow for reconstruction of the mass distribution of the collapsing object," Phys. Lett. B **758**, 429 (2016) doi:10.1016/j.physletb.2016.05.037 [arXiv:1601.07921 [gr-qc]].

[176] W. A. Hiscock and L. D. Weems, "Evolution of Charged Evaporating Black Holes," Phys. Rev. D **41**, 1142 (1990) doi:10.1103/PhysRevD.41.1142

[177] M. S. Seo, "de Sitter swampland bound in the Dirac-Born-Infeld inflation model," Phys. Rev. D **99**, no.10, 106004 (2019) doi:10.1103/PhysRevD.99.106004 [arXiv:1812.07670 [hep-th]].

[178] S. Mizuno, S. Mukohyama, S. Pi and Y. L. Zhang, "Hyperbolic field space and swampland conjecture for DBI scalar," JCAP **09**, 072 (2019) doi:10.1088/1475-7516/2019/09/072 [arXiv:1905.10950 [hep-th]].

[179] K. Dasgupta, M. Emelin, E. McDonough and R. Tatar, "Quantum Corrections and the de Sitter Swampland Conjecture," JHEP **01**, 145 (2019) doi:10.1007/JHEP01(2019)145 [arXiv:1808.07498 [hep-th]].

[180] A. R. Solomon and M. Trodden, "Non-canonical kinetic structures in the swampland," JCAP **09**, 049 (2020) doi:10.1088/1475-7516/2020/09/049 [arXiv:2004.09526 [hep-th]].

[181] T. Wrase and M. Zagermann, "On Classical de Sitter Vacua in String Theory," Fortsch. Phys. **58**, 906-910 (2010) doi:10.1002/prop.201000053 [arXiv:1003.0029 [hep-th]].

[182] G. Shiu and Y. Sumitomo, "Stability Constraints on Classical de Sitter Vacua," JHEP **09**, 052 (2011) doi:10.1007/JHEP09(2011)052 [arXiv:1107.2925 [hep-th]].

[183] S. R. Green, E. J. Martinec, C. Quigley and S. Sethi, "Constraints on String Cosmology," Class. Quant. Grav. **29**, 075006 (2012) doi:10.1088/0264-9381/29/7/075006 [arXiv:1110.0545 [hep-th]].

[184] G. Obied, H. Ooguri, L. Spodyneiko and C. Vafa, "De Sitter Space and the Swampland," [arXiv:1806.08362 [hep-th]].

[185] P. Agrawal, G. Obied, P. J. Steinhardt and C. Vafa, "On the Cosmological Implications of the String Swampland," Phys. Lett. B **784**, 271-276 (2018) doi:10.1016/j.physletb.2018.07.040 [arXiv:1806.09718 [hep-th]].

[186] A. J. Tolley and M. Wyman, "The Gelaton Scenario: Equilateral non-Gaussianity from multi-field dynamics," Phys. Rev. D **81**, 043502 (2010) doi:10.1103/PhysRevD.81.043502 [arXiv:0910.1853 [hep-th]].

[187] S. Garcia-Saenz, L. Pinol and S. Renaux-Petel, "Revisiting non-Gaussianity in multifield inflation with curved field space," JHEP **01**, 073 (2020) doi:10.1007/JHEP01(2020)073 [arXiv:1907.10403 [hep-th]].

[188] C. Cheung, P. Creminelli, A. L. Fitzpatrick, J. Kaplan and L. Senatore, "The Effective Field Theory of Inflation," JHEP **03**, 014 (2008) doi:10.1088/1126-6708/2008/03/014 [arXiv:0709.0293 [hep-th]].

[189] W. C. Lin and W. H. Kinney, "Trans-Planckian Censorship and *k*-inflation," Phys. Rev. D **101**, no.12, 123534 (2020) doi:10.1103/PhysRevD.101.123534 [arXiv:1911.03736 [gr-qc]].